MICROSTRUCTURE-BASED COMPUTATIONAL MODELING OF TRIP STEELS WITH DISPERSED PARTICLES

A Thesis

by

SARA CRISTINA DIAZ

Submitted to the Office of Graduate Studies of
Texas A&M University
in partial fulfillment of the requirements for the degree of

MASTER OF SCIENCE

August 2012

Major Subject: Civil Engineering

Microstructure-Based Computational Modeling of TRIP Steels with Dispersed Particles

MICROSTRUCTURE-BASED COMPUTATIONAL MODELING OF TRIP STEEL WITH DISPERSED PARTICLES

A Thesis

by

SARA CRISTINA DIAZ

Submitted to the Office of Graduate Studies of
Texas A&M University
in partial fulfillment of the requirements for the degree of

MASTER OF SCIENCE

Approved by:

Chair of Committee,	Rashid Abu Al-Rub
Committee Members,	Hanifah Muliana
	Luciana Barroso
	Ibrahim Karaman
Head of Department,	John Niedzwecki

August 2012

Major Subject: Civil Engineering

ABSTRACT

Microstructure-Based Computational Modeling of TRIP Steels with Dispersed Particles.

(August 2012)

Sara Cristina Diaz, B.S, Texas A&M University

Chair of Advisory Committee: Dr. Rashid K. Abu Al-Rub

Industries, such as the automotive industry, aim to increase the reliability of their products to match the demands and assure the safety of their clients. The proposition of a third generation advanced high strength steel is introduced in this study. The ideas surrounding the behavior of transformation induced plasticity (TRIP) steels and particle reinforced composites are combined and investigated. A finite element model (FEM) is created to investigate the effects of dispersed ceramic particles with varying parameters throughout a TRIP steel microstructure and identify key mechanisms responsible for achieving simultaneous enhancements in strength and ductility. The ceramic material utilized and volume fraction of the ceramic particles dispersed throughout the representative volume element (RVE) are the two varying parameters investigated in this study.

Through observing the equivalent plastic strain (PEEQ) distribution at different strain levels up to 100%, evidence of failure controlled by strain localization throughout the ferrite matrix is more prevalent through the softer, austenitic microstructures with 5% or less ceramic particle inclusions. On the other hand, the presence of the hard

martensite constituents, or 10% volume fraction of ceramics in an austenitic structure, proposed that failure would engender due to void nucleation at the harder constituent/ferrite interfaces. These voids will then grow and coalesce throughout the microstructure, resulting in a crack.

The increased addition of ceramic inclusions also illustrates a simultaneous enhancement in the ultimate tensile strength and ultimate strain in all microstructures. Tensile strength increases by a total of 18% with 10% volume ceramic particles in a TRIP steel microstructure. Between utilizing silicon carbide, cementite, zirconia and aluminum oxide ceramic particles, the microstructure that illustrated the most optimal enhanced performance in strength and ductility was the 10% volume fraction aluminum oxide particle reinforced TRIP steel composite.

ACKNOWLEDGEMENTS

I would like to thank my committee chair, Dr. Rashid Abu Al-Rub, and my committee members, Dr. Luciana Barroso, Dr. Anastasia Muliana, and Dr. Ibrahim Karaman, for their guidance and support throughout the course of this research. I would also like to express my infinite gratitude to Ardeshir Tehrani and Mahmood Ettehad for all the help and guidance in this research.

I also want to thank the National Science Foundation, Department of Energy, and the Army Research Office for their support. Finally, thanks to my lovely family and close friends for their encouragement to keep going, even through the hard times. I couldn't have done it without your support.

TABLE OF CONTENTS

Page

Page

LIST OF FIGURES

Page

Page

Page

Page

LIST OF TABLES

Page

Page

1. INTRODUCTION

1.1 Inspiration

Technological advances proliferate through industry at an exponential rate, causing the demand for innovative materials and products to increase. Light weight metals illustrate one of the most attractive and desired aspects stemming from this technological evolution. Reduced weight proposes less energy consumption for performance which results in a variety of environmental benefits such as smaller power plants, energy storage systems and fewer emissions. Yet, with weight reduction and increased durability, the material must maintain or increase its strength and resistance to fracture. The alteration of the microstructure of metals provides the basis for a broad variety of technological innovations with a profound impact on society. Advanced strength steels, for example, are a growing innovation to the engineering world. The simultaneous enhancement of toughness as well as strength in steels has been studied rigorously. So far, transformation induced plasticity (TRIP) steels prove to illustrate the highest ductility to strength ratio among advanced high strength steels as illustrated in Figure 1 (Wagoner and Smith, 2006) and Figure 2 (1999-2011).

This thesis follows the style of International Journal of Plasticity.

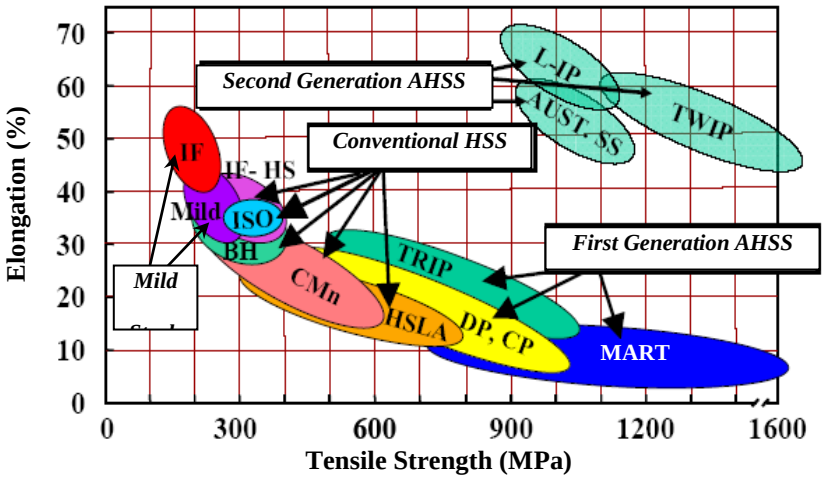

Figure 1 Ductility-strength relationship of different grades of steels (Wagoner and Smith, 2006)

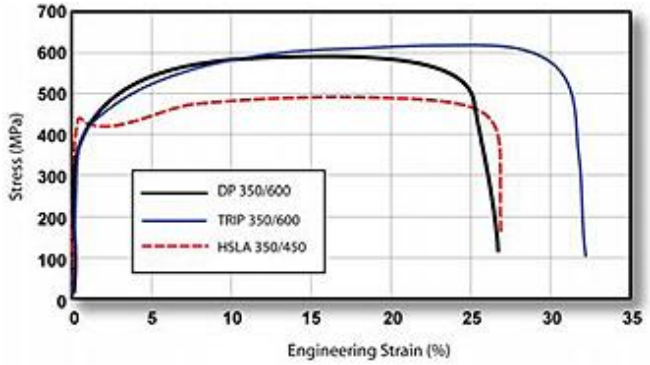

Figure 2 Engineering stress and strain comparison of some advanced high strength steels (1999-2011)

1.2 TRIP Steel Microstructure

TRIP steels contain a microstructure composed of retained austenite and bainite embedded in a ferrite matrix as illustrated in Figure 3 (1999-2011). In an isothermal

environment the metastable retained austenite transforms into martensite upon straining. As a result of plastic deformation, the transformation from retained austenite to martensite results in a change in the composite's overall mechanical properties. This is a consequence of the formation of martensite since it is the hardest and strongest microstructure. It is unfortunately also the most brittle. Although it is not as strong as martensite, bainite is introduced as an aid to the soft ferrite matrix. It's finer microstructure exhibit a desirable combination of strength and ductility, which make it a tougher phase than martensite.

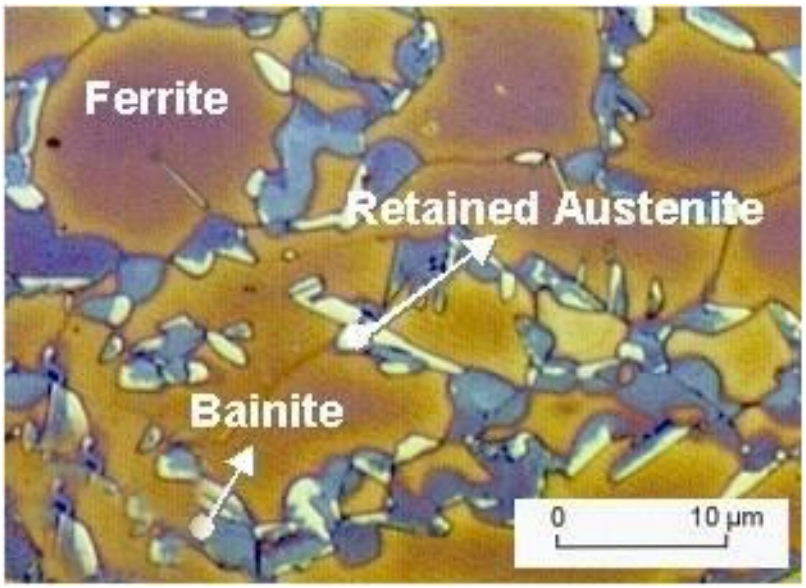

Figure 3 TRIP steel microstructure example (1999-2011)

1.3 TRIP Steel Phase Transformation

Understanding the microscopic and macroscopic level of TRIP steels as well as its behavior in different conditions has been a large focus of study. Considering the phase transformation behavior in TRIP steels has been a challenging factor that has been investigated through various analytical, experimental and numerical methods (Iwamoto and Tomita, 1995, 2001; Iwamoto and Tsuta, 2000, 2002, 2004; Iwamoto et al., 1998; Kim, 1988; Olson and Cohen, 1975; Papatriantafillou et al., 2006; Stringfellow et al., 1991). Olsen and Cohen (Olson and Cohen, 1975), were the first to propose a transformation kinetics model for strain induced martensitic transformation. It was claimed that the main parameters responsible for the phase transformation were temperature and plastic strain. This model has since then been expanded by numerous studies. For example, Olsen and Cohen's model was expanded by Stringfellow et al. (Stringfellow et al., 1991), by recasting the martensitic volume fraction evolution in a generalized rate form that included the influence of the stress state on the phase transformation. Austenite grain size was another consideration proposed by Iwamoto and Tsuta (Iwamoto and Tsuta, 2000; Iwamoto et al., 1998). Iowamoto and Tsuta (Iwamoto and Tomita, 1995, 2001; Iwamoto and Tsuta, 2000, 2002, 2004; Iwamoto et al., 1998) enhanced these works into a phenomenological constitutive model for austenitic steel. This model included the rate of shear band formation's dependence on the strain rate (Iwamoto and Tomita, 1995)and stress state (Iwamoto et al., 1998).

Aside from modeling the behavior, computational as well as experimental efforts have been pursued to explore parameters that highly influence the enhanced properties

resulting from phase transformation. TRIP steels can illustrate different behaviors by simply altering the properties, grain sizes, volume fractions, size, and spatial distributions of the constituent phases, especially the retained austenite (Choi et al., 2009; Muransky et al., 2006; Uthaisangsuk et al., 2008; Zrnik et al., 2006). The increased strength and formability of TRIP steel is not only a result of solid solution hardening, grain refinement and precipitation hardening. The coexistence of the different constituent phases and their varying properties and grain sizes play a large role in this enhancement (Uthaisangsuk et al., 2008). Kim Chongmin (Kim, 1988) developed an analytical model which described the tensile deformation behavior of dual phase steel, which idealizes the same martensitic transformation as TRIP steel. This model illustrated that the most influential parameter to increasing ductility and strength resulted in a large work hardening coefficient of martensite. Choi, Soulami, Lui, Sun and Khaleel (Choi et al., 2010), found that higher austenite stability delays martensitic transformation. This is due to the fact that the transformation has a higher volume of retained austenite to transform, which naturally takes more time. By extending the transformation time, the ductility and formability of TRIP steels is enhanced. Stronger constituent phases increase the ultimate tensile strength as well. This explains the purpose of introducing bainite into the ferrite matrix. Unfortunately, it was also concluded that by increasing the austenite volume fraction and/or the ferrite strength alone was not sufficient to improve the overall performance of TRIP steels. The inhomogenity in the microstructure among the different phases serves as an imperfection condition that triggers plastic instability (Choi et al., 2009). In other words, this conflict in phase boundaries serves as a potential

area for engendered damage, and ultimately failure. Yet, another interesting observation was made by Wenzel and Aneziris (Wenzel and Aneziris, 2010), whom investigated ceramic matrix composites based on magnesia partially stabilized zirconia with TRIP-steel particles. This paper proposed that the volumetric expansion (about 1%) of austenite into martensite during transformation served as a mechanism that hindered crack growth, thus increasing the materials strength. This volumetric expansion hinders damage development in the microstructure by delaying void nucleation between the different phases (Jacques et al., 2001). Unfortunately, as found before, this investigation also found that failure initiated due to bonding between the different constituents, which will be revisited later. More recently, Ke Zhang et al. (Zhang et al., 2011) utilized X-ray diffraction line profile analysis (XPLA) to examine a high strength treated martensitic steel under tensile tests at different strain stages. Their results propose a new effect of austenite on the ductility enhancement in which the austenite phase has the ability to continuously absorb dislocations from nearby martensite bands. This behavior is known as the dislocation absorption by retained austenite (DARA) effect. This increases deformability of the martensite phase during straining. Thus, the DARA effect is a vital factor driving enhanced toughness. The retained austenite serves as a crutch to the martensite by absorbing more of the plasticity occurring and allowing the martensite elongate further.

When investigating TRIP steel, two main failure modes are discussed- cleavage and dimpling fracture. Various damage models illustrate that these fracture modes depend highly on the stress state, the internal cleanness or previous existence of damage,

the volume fraction of the retained austenite, the morphology of the martensitic islands, and the conditions of neighboring constituent grain sizes(Gurson, 1977; Papaefthymiou et al., 2006; Uthaisangsuk et al., 2008, 2011). Since TRIP steels generally undergo ductile fracture, it is stated that this failure depends highly on the microstructure, voids, inclusions, and micro cracks in the soft ferrite matrix that lead to a dimple fracture (Choi et al., 2010; Gurson, 1977; Papaefthymiou et al., 2006; Uthaisangsuk et al., 2008, 2011). These factors are known as damage in the microstructure. Damage could naturally exist in the structure before analysis, and can also be initiated or increased during straining or loading. The leading mechanism for ductile failure or dimpling fracture is void initiation and coalescence within the ferrite matrix. This mainly occurs along the grain boundaries of the ferrite or the constituents. Ductile fracture entails large plastic deformations. On the other hand, major failure bands have also shown to cut through the hard bainite and martensite grains, which are known as cleavage fracture. This fracturing entails material separation due to an achieved critical condition, initiating a crack and causing propagation through the material due to local stress triaxility during deformation (Papaefthymiou, 2005; Uthaisangsuk et al., 2011; Xu and Needleman, 1994). In TRIP steel, cracks are observed to engender at the hard phases in the material, such as the retained austenite and martensite. Crack initiation and propagation is the primary mechanism for cleavage fracture. Cracks can initiate in the banded bainite package structure, retained austenite with insufficient transformation stability, and martensite in the initial microstructure. These cracks mainly occur when a martensite or austenite

grain forms and fails inside a bainite island (Papaefthymiou et al., 2006; Uthaisangsuk et al., 2008, 2011).

1.4 Particle Reinforced Metals

Aside from TRIP steel, particle reinforced metals have also been another branch of study that has proven to be extremely successful. Besides illustrating great performances in increasing modulus and strength and illustrating large improvement in the plastic work-hardening behavior, they also prove to be affordable, show high resistance to damage, and are not difficult to manufacture (Abu Al-Rub, 2009; Lloyd, 1994). A variety of investigations have been done to prove the addition of hard inclusions into a soft matrix has the potential to increase the overall mechanical properties of the composite.

Large focuses have been on reinforced metal matrix composites with ceramic inclusions, such as silicon (Abu Al-Rub, 2009; Bao, 1992; Christman et al., 1989; Corbin and Wilkinson, 1994; Evans et al., 1991; Hu, 1991; Jain et al., 1994; Kiser et al., 1996; Llorca and Poza, 1994; Lloyd, 1990; Lloyd, 1991; Lloyd, 1994; Mazen and Emara, 2004; McDaniels, 1985; Mummery et al., 1993; Nan and Clarke, 1995; Shen et al., 1994; Taggart and Bassani, 1991; Vasudevan et al., 1989; Yang et al., 1990; Zahl and McMeeking, 1991; Zhu et al., 1994). Besides the properties of the materials, the parameters of the inclusions play a large role in the composite's overall behavior. Particle shape for example is a large factor. Angular shaped inclusions provide sharp areas for increases in local stress and consequently reduce ductility (Lloyd, 1994). Thus

particles with smooth edges are the most ideal. In regards to size, smaller particles perform best. Larger particles provide a larger area to handle stress and increase the risk of particle or cleavage fracture. At equal volume fractions, decreasing particle sizes usually illustrates a substantial increase in yield strength and flow stress of the composite (Abu Al-Rub, 2009; Kiser et al., 1996; Lloyd, 1994; Nan and Clarke, 1995; Zhu et al., 1994). When examined by Kiser et all, larger particles proved to be the weakest and were the first to fail in PMMC's (Kiser et al., 1996). It is much more ideal to have the stress distributed throughout a larger amount of smaller particles than a few coarser particles. Lloyd (Lloyd, 1994) proposes that coarser ceramic particles will have a higher probability of containing fracture initiating defects or initial damage. These particles should be less than 10 micrometers to be considered fine. The size distribution of these particles should also be uniform to avoid stress concentrations on slightly larger particles. The distribution of these small particles is also extremely important. Closely spaced elastic particles cause large local stress levels that greatly exceed those of the matrix flow stress , resulting in void nucleation and coalescence and ultimately failure. Therefore, it is more effective to distribute particles uniformly throughout the matrix. This explained, it is also important to realize that one cannot have too large of a particle volume fraction. Although yield strength of the metal matrix increases as more reinforcement particles are added, the tensile strength illustrates better results at lower particle volume fractions and remains constant or decreases when more particles are added and a certain volume fraction of particles is reached (Mazen and Emara, 2004). For example, Mazen and Emara's (Mazen and Emara, 2004) investigation of Al-SiC

particle metal matrix composites, the unreinforced aluminum matrix illustrated an original tensile strength of 108.2MPa. This property increased to 119.7MPa at as 2.5% of SiC particle reinforcement was added. It then increased slightly at 5% SiC particle to 120MPa, yet started decreasing at 10% SiC particle to 108.3MPa.

Compatibility between the materials in the composite is another large factor that must be considered. The bonding interface between the particle and the matrix has a large influence on the behavior of the composite (Abu Al-Rub, 2009; Bao, 1992; Christman et al., 1989; Corbin and Wilkinson, 1994; Hu, 1991; Jain et al., 1994; Kiser et al., 1996; Llorca and Poza, 1994; Lloyd, 1990, 1994; Mummery et al., 1993; Shen et al., 1994; Taggart and Bassani, 1991; Vasudevan et al., 1989; Wenzel and Aneziris, 2010; Yang et al., 1990; Zahl and McMeeking, 1991). If weak, this interface could serve as the initiation of failure by separation, or voiding, and engendering damage and ultimately failure in the composite. The properties of the materials may be very strong and durable, yet if bonding between them is weak, the composite will fail before allowing any of the materials to undergo any type of deformation. The transfer of stress throughout the metal will be stopped at these interfaces, thus hindering the load to transfer throughout the composite effectively. Wensel and Aneziris (Wenzel and Aneziris, 2010) noticed this in their experiment when no cracks were observed between the zirconia ceramic matrix and no plastic deformation had occurred in the TRIP steel inclusions. Thus, damage initiated between the zirconia-steel interfaces as the two materials debonded. Mismatched materials with incompatible properties may also lead to early inhomogeneous plastic yielding during loading in which stresses are lower than the

required in the pure matrix (Corbin and Wilkinson, 1994; Jain et al., 1994; Kiser et al., 1996; Taggart and Bassani, 1991; Zahl and McMeeking, 1991). At high strains, this incompatibility developed large stresses within the particles that exceed that of the matrix alone (Bao, 1992; Christman et al., 1989; Evans et al., 1991; Hom and McMeeking, 1991). The overall behavior of the composite depends highly on the how the matrix and particles function together. For example, in Kaiser et all's PMMC model, they describe that under tensile loading, the particles crack at a rate that proves to be dependent on the intrinsic strength characteristics of the particles as well as the flow characteristics of the matrix. The cracking of the particles reduces the work hardening rate, which consequently decreases the strength and ductility and will eventually lead to failure (Abu Al-Rub, 2009; Kiser et al., 1996). The reactivity between two different phases may even cause chemical changes within the matrix and must also be considered. For example, most carbides such as boron carbide and titanium carbide are thermodynamically unstable in molten aluminum and react in a complex manner(Lloyd, 1994). Another factor that is most overlooked is the processing of the composite. Lloyd (Lloyd, 1994) discovered that with powder metallurgy processing, the composition of the matrix and the type of reinforcement are independent of one another. On the other hand in molten metal processing they are intimately linked in terms of different reactivities which occur between the reinforcement and the matrix in the molten state. Features such as this are highly overlooked in composite simulations and are worth noting.

Evidence from numerous theoretical , numerical and experimental approaches have concluded that the particle reinforced composites illustrate an enhanced performance as opposed to its pure matrix state (Abu Al-Rub, 2009; Kiser et al., 1996; Lloyd, 1990, 1994; Mazen and Emara, 2004). This is due to the enhancement of properties of the composite. One mechanical property that shows repetitious supporting data of increasing due to particle reinforcement is Young's modulus, consequently increasing the composite's overall strength. McDanels (McDaniels, 1985), for example, investigated SiC whisker and particle reinforcement in several alloy matrices and reported up to a 60% increase in yield and ultimate tensile strengths. As previously discussed, the addition of TRIP inclusions in Wenzel and Aneziris (Wenzel and Aneziris, 2010) experiments increased the fracture strength of the composite by 43%.

The most prominent short coming of particle reinforced composites is limited ductility. The addition of harder particles into the soft matrix decreases the overall ductility of the metal structure in most cases(Lloyd, 1994). In some special cases, this issue was overcome. One particular case where a ceramic matrix composite was reinforced with TRIP steel particles, toughness was enhanced almost three times as much as the pure ceramic material (Wenzel and Aneziris, 2010).

1.5 Other TRIP Steel and Particle Reinforced Composite Behavioral Mechanisms

With the unique microstructure presented in TRIP steel, other factors that do not correlate specifically with phase transformation have been identified that are responsible for altering strength and ductility behavior. Manufacturing and processing TRIP steel is

paramount to the mechanical behavior since it entails heat-treating the material, determination of steel composition, and molding the microstructure. The processing of low alloy multiphase and TRIP steels is still a matter of current research (Muransky et al., 2006). According to Sittner, process should be done to yield a TRIP steel microstructure that contains 50 to 60% ferrite, 25 to 40% bainite, and 5 to 15% metastable retained austenite uniformly distributed throughout the specimen. The temperature and cooling rate during this process will also be a very important factor for the strength and ductility of the microstructure (Muransky et al., 2006). Besides temperature, according to Lloyd (Lloyd, 1994), in powder processed material, the reinforcement distribution will depend on the blending and consolidation procedures, as well as the relative size of the matrix and reinforced particles. For example, if the matrix powder is much larger than the reinforcement, the reinforcement is more likely to collect in the gaps between the matrix particles. Consequently, uniform distribution of the particles throughout the matrix would not exist. If this occurs, secondary processing could be utilized to try and redistribute the particles throughout the matrix. Unfortunately with TRIP steels this will cause further change in the overall performance of the composite due to the phase change vulnerability to temperature.

Alternatively, in composites processed by molten metal mixing methods, the process is more complex because the reinforcement distribution is influenced by the distribution in the liquid due to mixing, after mixing but before solidification, and redistribution as a result of solidification. Controlling these parameters during the production process is of paramount importance since they define the microstructure's

behavior and mechanical properties (Zrnik et al., 2006). As previously mentioned, the strain hardening behavior and the temperature sensitivity is what distinguishes TRIP steels from conventional cold formable steels. Bleck describes that there is strong temperature dependence of the strain hardening for all TRIP aided steels (Bleck et al., 1999). The strain driven phase transformation caused the mechanical properties of TRIP steels to respond sensitively and change in a wide range if the test temperatures. Zirnik also claims that an optimized structure of TRIP steels for different forming operations or sorting parameters will need a more thorough and quantitative understanding of the temperature and stress state dependencies and microstructural features responsible for these (Zrnik et al., 2006). Thus, due to its large sensitivity to temperature, the manufacturing of TRIP steel still needs further review.

Another large factor that is still under investigative study is the consequences of size effect of particles or constituents involved in a metal matrix composite. Nan and Clark (Nan and Clarke, 1995) investigated the influence of particle size and particle fracture on the elastic/plastic deformation of metal matrix composites, more specifically, silicon carbide reinforced aluminum. They studied an analytical method for calculating the deformation behavior of metal matrix composites over a full range of particle sizes. It is a key combination of the key features of dislocation plasticity with a continuum mechanics approach based on effective medium approximations. Four main mechanisms were identified that contributed to the flow stress of the composite. The first contribution entailed the Orowan stress, or the stress necessary to pass a dislocation through an array of impeding particles of average spacing. This stress is highly dependent on the size of

the particles and their volume fraction. The second and third factors entail the strain gradient effects resulting from the geometrically necessary distributions of dislocations. These dislocations are essential for accommodating the plastic strain discrepancy between the hard particles and the surrounding soft matrix. The fourth contributions entail the density of initial dislocations presented in the microstructure due to processing and variant thermal expansions.

With these mechanisms of flow stress considered, and assuming a perfectly bonded composite, Nan and Clark found that overall, smaller sized particles yielded larger stresses. As previously explained, larger particles tend to crack much easier than smaller sized particles in tension. As the strain was increased, so did the proportion of particle fractures throughout the composite. It was also shown that at 15% volume fraction of silicon carbide particles in an aluminum matrix, with uniform particle sizes throughout the microstructure, smaller sized particles illustrated a higher stress, yet yielded a smaller strain. Thus, even at the same volume fraction, smaller particles illustrate a higher strength, yet reduce ductility or the strain necessary to cause fracture. According to the study, when particle sizes are large, or the diameter of the particles exceeds 10 μm, particle size is not a prevalent contributor and thus continuum plasticity dominates. On the other hand, when the size of the particles is small, or less than 0.5μm, the strengthening caused by dislocations dominates. Consequently, the overall mechanical behavior of the composite relies heavily on the size of the particles, even at an equivalent volume fraction.

The dependents of particle size also increased as the volume fraction of particles increased throughout the microstructure. This is relevant since even at the same volume fraction, particle size was essential. It was noticed that a higher volume fraction of particles in the composite yielded a lower applied strain at which fracture occurred in particles of a given size. Varying particle sizes were also investigated by Nan and Clark. The standard deviation increase of particle size distribution reflected an increase in the quantity of larger particles. Consequently, these larger/coarser particles cracked before the smaller particles at a given strain increase resulting in a decreased calculated flow stress. Thus, uniformly sized particles or constituents illustrated a superior enhancement on the overall behavior of the composite in comparison to deviating particle sizes.

1.6 Objective

The alteration of the microstructure of metals provides the basis for a broad variety of technological innovations with a profound impact on society. TRIP steel already offers a high strength and ductility ratio that proves to be a very attractive feature for steel structures. Yet, by combining this advanced high strength material, with the ideals and results surrounding particle reinforced composites, it is highly possible to enhance the performance and behavior of TRIP steel even further. The objective of this paper is to investigate the deformation behavior of ceramic particle reinforced TRIP steel. This will include varying parameters throughout the composite's constituents to identify key mechanisms responsible for achieving simultaneous enhancements in strength and ductility.

2. THEORY

Since the rate of transformation is the main factor that affects the strength and toughness of TRIP steels, it is worth investigating methods of hindering or slowing this process down. Overall, it is predicted that the presence of these brittle inclusions in a TRIP microstructure will further delay the transformation of retained austenite into martensite, thus allowing these hardening properties to behave for a longer period of time. Also, it is also predicted that the hard ceramic particles will also take most of the stress imposed on the composite, and allow enhanced performance in material strength of the overall composite. Ceramic inclusions will provide the added increase in strength in the same form as other particle reinforced metals described earlier. Likewise, as described previously, in actual experimentation, the DARA effect should also relieve some stress from the martensite, allowing it to withstand more stress. Extending the period of transformation during straining plays a large role in allowing the material to elongate even further. By increasing the ductility in the material, it allows the composite to become tougher and more resilient to impact forces. It should be noted that the addition of ceramic inclusions will also introduce another hardened phase into the metal, thus providing a higher risk of potential cleavage fracture. Another phase boundary is also introduced into the material. For this investigation, all phases will be assumed to be perfectly bonded. Also, although it is a key factor that must be investigated further, the phase transformation of the austenite to the martensite will not be simulated but is taken into account by modeling the beginning and final stages only. This will be described in

more detail in the simulation descriptions. The metal composite's behavior will be monitored by investigating its stress vs. equivalent strain response under uniaxial tensile loading. It is predicted that the reinforced TRIP steel will have a ductile fracture in which extensive plastic deformation will occur before ultimate failure. This fracture occurs after the reinforced metal composite has experienced hardening and undergoes softening. This softening can be due to three factors which include localization, damage due to voids and cracking, and temperature. It is important to note, due to its complexity and uncertainty, the consequences of size effect, damage, temperature effects, and gradient theory are neglected in this investigation, yet worth noting for future opportunities.

2.1 Elasticity and Plasticity Theory

During elastic deformation, and assuming the material to be isotropic, elastic behavior is described by Hooke's law

$$\sigma_{ij} = E_{ijkl}\varepsilon^{e}_{kl}. \tag{2.1.1}$$

The modulus of elasticity, E, is simply the following equation:

$$E_{ijkl} = GI^{d}_{ijkl} + K\delta_{ij}\delta_{kl} \tag{2.1.2}$$

where the shear modulus and the bulk modulus are

$$G = \frac{E}{2(1+\nu)} \tag{2.1.3}$$

$$K = \frac{E}{3(1-2\nu)} \tag{2.1.4}$$

and I^d_{ijkl} is the deviatoric component of the 4rth order identity tensor:

$$I^d_{ijkl} = I_{ijkl} - \frac{1}{3}\delta_{ij}\delta_{kl} \tag{2.1.5}$$

$$I_{ijkl} = \frac{1}{2}(\delta_{ik}\delta_{jl} + \delta_{il}\delta_{jk}) \tag{2.1.6}$$

.

Elastic behavior occurs until the initial von Mises yield condition is exceeded.

This study recognizes that the metal composite's plastic deformation could be explained through the flow plasticity theory which incorporates the hardening phenomenon into the model. Hardening causes the yield surface to expand and alter while undergoing plastic deformation during loading. Due to this, the alteration of the yield surface depends on the plastic strain at each increment of loading. Thus, calculating the plastic strain at different stages of loading can be done through investigating the plastic flow rule (Kelly, 2008).

To begin this plastic flow investigation, it is important to recall that an increment in strain $\dot{\varepsilon}$ can be decomposed into two parts, elastic and plastic,

$$\dot{\varepsilon}_{ij} = \dot{\varepsilon}^e_{ij} + \dot{\varepsilon}^p_{ij} \,. \tag{2.1.7}$$

Since the TRIP steel composite model is proposed to be isotropic, the principal plastic strain increments $\dot{\varepsilon}^p_{ii}$ are proportional to the principal deviatoric stresses s_{ii} as follows:

$$\frac{\dot{\varepsilon}^p_{ii}}{s_{ii}} = \dot{\lambda} \geq 0 \quad (no\ sum\ on\ i) \tag{2.1.8}$$

.

This relationship illustrates the ratios of the plastic strain increments to the deviatoric stresses where $\dot{\lambda}$ is the proportional positive scalar constant or the plastic multiplier.

This constant depicts the magnitude of plastic strain that occurs and depends on the yield criterion that is utilized. The plastic multiplier also depends on the hardening behavior since it depicts how the yield surface evolves which will be explained shortly. In terms of stresses, Equation (2.1.8) can be expressed as

$$\dot{\varepsilon}_{ij}^{p} = \dot{\lambda} s_{ij} \tag{2.1.9}$$

which is denoted as the Levy-Mises flow rule. Equation (2.1.9) is more generally seen as

$$\dot{\varepsilon}_{ij}^{p} = \dot{\lambda} \frac{\partial g}{\partial \sigma_{ij}} \tag{2.1.10}$$

where g is a scalar function called the plastic potential that gives the plastic strain when differentiated with respect to stress. Equation (2.1.10) is known as the non-associated flow rule. For this research, we want to associate Equation (2.1.10) with a particular yield criterion, more specifically, the von Mises criterion:

$$f(s_{ij}) = J_2 - k^2 = 0 \tag{2.1.11}$$

where k is the yield stress of the material in pure shear and J_2 is the second invariant of the deviatoric stress defined respectively as

$$k_i = \frac{\sigma_Y^i}{\sqrt{3}} \tag{2.1.12}$$

$$J_2 = \frac{1}{6}[(\sigma_x - \sigma_y)^2 + (\sigma_y - \sigma_z)^2 + (\sigma_z - \sigma_x)^2] + \tau_{xy}^2 + \tau_{yz}^2 + \tau_{zx}^2 . \tag{2.1.13}$$

Therefore, by setting $g = f$ or making the plastic potential the yield condition, we will be utilizing the associated flow rule

$$\dot{\varepsilon}_{ij}^{p} = \dot{\lambda} \frac{\partial f}{\partial \sigma_{ij}} \tag{2.1.14}$$

where $$\frac{\partial f}{\partial \sigma_{ij}} = s_{ij} \tag{2.1.15}$$

to match Equation (2.1.9). Also, to make notation simpler, the associated flow rule in Equation (2.1.14) can be expressed in terms of principal axis.

$$\dot{\varepsilon}_{ij}^{p} = \dot{\lambda} \frac{\partial f}{\partial \sigma_{ij}} \tag{2.1.16}$$

Although the associative flow rule is not a law, it has been observed in a variety of experiments with plastically deforming metals. Now by differentiating the yield condition with respect to the stress one has

$$\frac{\partial f}{\partial \sigma_{ij}} = \frac{\partial J_2}{\partial \sigma_{ij}} \tag{2.1.17}$$

where

$$\frac{\partial J_2}{\partial \sigma_i} = \frac{\partial}{\partial \sigma_i}\left(\frac{1}{6}[(\sigma_1 - \sigma_2)^2 + (\sigma_2 - \sigma_3)^2 + (\sigma_3 - \sigma_1)^2]\right) = \frac{2}{3}\left[\sigma_1 - \frac{1}{2}(\sigma_2 + \sigma_3)\right] \tag{2.1.18}$$

where σ_i are the principal stresses ($i = 1, 2, 3$).

Thus by substituting Equation (2.1.18) into Equation (2.1.16), the incremental plastic strain may be calculated. Also, it is important to note that for Von Mises plasticity, the plastic multiplier is the effective plastic strain, $\dot{p}$, and is calculated as

$$\dot{\lambda} = \dot{p} = \sqrt{\frac{2}{3}\dot{\varepsilon}_{ij}^{p}\dot{\varepsilon}_{ij}^{p}}\ . \tag{2.1.19}$$

From this point and for this study, the plastic multiplier will be denoted as the incremental effective plastic strain, or $\dot{p}$. The total plastic strain, p, is calculated by simply integrating with respect to time

$$p = \int_0^t \dot{p} dt \tag{2.1.20}$$

Isotropic hardening is another factor that must be considered with the effective plastic strain since it causes the yield surface to expand with increasing stress. The stress due to isotropic hardening, R, is calculated by

$$R_i = K_i p^{\eta_i} \tag{2.1.21}$$

where K is the hardening coefficient and η is the hardening coefficient exponent for material i. The notation for material i will become more useful when the model for this project is described shortly. Since this phenomena occurs after the material reaches its initial yield stress, the total stress due to isotropic hardening is the sum of the yield stress and the additional stress due to isotropic hardening. Utilizing the yield boundary in Equation (2.1.11), it can be modified to incorporate isotropic hardening. First, for a uniaxial case, the effective stress of a Von Mises material, $\bar{\sigma}$, is

$$\bar{\sigma} = \sqrt{3J_2} = \sqrt{\frac{3}{2} s_{ij} s_{ij}} \tag{2.1.22}$$

Therefore our modified yield boundary can be described as

$$f = \sqrt{\frac{3}{2} s_{ij} s_{ij}} - [\sigma_Y + R] \leq 0 \tag{2.1.23}$$

2.2 Temperature Effects and Conditions

Equation (2.1.23) illustrates an isothermal case. In adiabatic conditions, temperature would have to be considered since it will affect material behavior during deformation. Thus Equation (2.1.23) is altered as:

$$f = \sqrt{\frac{3}{2} s_{ij} s_{ij}} - [\sigma_Y + R][1 - \left(\frac{T}{T_m} \right)^n] \leq 0 \tag{2.2.1}$$

where T is the reference temperature, T_m is the melting temperature, and n is the temperature softening exponent (Voyiadjis et al., 2006). In the case of adiabatic conditions, the plastic strain depends highly on the change in temperature at each increment. The thermomechanical heat balance equation for adiabatic conditions is

$$\rho c_p \dot{T} = \gamma \sigma_{ij} \varepsilon_{ij}^p \tag{2.2.2}$$

where ρ is the density, c_p is the specific heat, $\dot{T}$ is the incremental temperature, and γ is the inelastic heat fraction or the amount of dissipated energy that is converted to heat. The total temperature is found by integrating the time increment with respect to time:

$$T = \int \dot{T} dt \tag{2.2.3}$$

2.3 Theory in ABAQUS

For this study, we will investigate the previously explained theories in ABAQUS for TRIP steel and the TRIP steel composite models. As mentioned previously, once the yield stress for each material is exceeded, it undergoes plastic

deformation. Each phase is assumed to follow the associative plastic flow rule. The plastic flow stresses for ferrite, bainite, austenite, and martensite are assumed to satisfy the isotropic hardening law , thus the plastic stresses will be calculated as follows (Choi et al., 2009; Choi et al., 2010; Voyiadjis et al., 2006):

$$\sigma_0^i = \sigma_Y^i + K_i p^{n_i} \tag{2.3.1}$$

where i is either F, B, A, or M to indicate if the material is ferrite, bainite, austenite or martensite, respectively. As illustrated, the plastic parameters in this investigation only depend on the hardening coefficients and exponents. It is important to note that martensite is assumed to have a linear behavior in contrast to the other phases. This will become clear when parameters for each phase are introduced in the next chapter.

The yield function is calculated utilizing trial stresses and testing if integration points exceed the initial yield boundary. Once this yield boundary is breached, plastic deformation engenders and elastic behavior is no longer considered. Analyzing plastic deformation requires an iteration process to compute the plastic multiplier, or incremental plastic strain. Since this equation is non-linear, the Newton Raphson (N-R) method is utilized to solve for the incremental plastic strain when the yield condition = 0. This follows the standard Kuhn-Tucker loading/unloading conditions:

$$f \le 0,\ \dot{\lambda} \ge 0,\ \dot{\lambda} f = 0,\ \dot{f} = 0 \tag{2.3.2}$$

This then allows the calculation of the plastic and elastic strain increments which can help interpret the stress of the material at the next increment. The calculation of the plastic and elastic strain increments are updated for each iteration to observe the effective stress at each increment. It is paramount to stress that although the material is

assumed to be isotropic, large strains and deformations are considered in the ABAQUS analysis.

2.4 Large Deformation Plasticity Theory

For small deformation assumptions, there is large focus on the Cauchy stress, σ, which is relative to the deformed shape. When examining large deformation scenarios, the desired constitutive equations are to be objective, or frame indifferent. For the purpose of this section only, large deformation theory will be expressed in tensor notation since it is much easier to express than indicial notation. Thus in order to do this, we introduce the following equation (Voyiadjis et al., 2006):

$$\boldsymbol{\sigma}_r = \mathbf{Q}\cdot\boldsymbol{\sigma}\cdot\mathbf{Q}^T \tag{2.4.1}$$

where Q describes the rate of rotation and follows

$$\mathbf{Q}\cdot\mathbf{Q}^T = 1. \tag{2.4.2}$$

As stated, the Cauchy stress proves to be objective, but the incremental stress necessary to run this analysis is not unless Q is constant since

$$\dot{\boldsymbol{\sigma}}_r = \dot{\mathbf{Q}}\cdot\boldsymbol{\sigma}\cdot\mathbf{Q}^T + \mathbf{Q}\cdot\dot{\boldsymbol{\sigma}}\cdot\mathbf{Q}^T + \mathbf{Q}\cdot\boldsymbol{\sigma}\cdot\mathbf{Q}^T \tag{2.4.3}$$

where

$$\dot{\boldsymbol{\sigma}}_r \neq \mathbf{Q}\cdot\dot{\boldsymbol{\sigma}}\cdot\mathbf{Q}^T. \tag{2.4.4}$$

In order to make this stress rate objective, three main objective stress rates will be described briefly. These are the Truesdell rate, Green-Naghdi rate, and the Jaumann rate. Each rate is a slight variation of the other and may be utilized.

To begin, since this analysis is of large or finite deformations, the Piola-Kirchoff stress tensors are utilized to identify the stress relative to the undeformed, original shape versus the Cauchy stress which signifies the stress relative to the deformed structure. The main focus is the 2nd Piola-Kirchhoff stress tensor, $\mathbf{S}$, which relates the forces presented in the original or reference frame, to areas in the reference frame as shown in Equation (2.4.5).

$$\mathbf{S} = J\mathbf{F}^{-1} \cdot \boldsymbol{\sigma} \cdot \mathbf{F}^{-T} \tag{2.4.5}$$

where $\mathbf{F}$ is the deformation gradient, formerly described more generally as $\mathbf{Q}$, and J is the Jacobian determinant defined as follows:

$$\mathbf{F} = \frac{\partial \mathbf{x}}{\partial \mathbf{X}} = \mathbf{R} \cdot \mathbf{U} \tag{2.4.6}$$

where $(\cdot)$ means $\mathbf{A} \cdot \mathbf{B} = A_{ik} B_{kj}$

and where $\mathbf{x}$ describes the deformed configuration, $\mathbf{X}$ is the undeformed configuration, $\mathbf{R}$ is the orthogonal rotation tensor, and $\mathbf{U}$ describes the deformation or "stretch" and

$$J = \det \mathbf{F} \tag{2.4.7}$$

where $J \geq 0$ since material cannot be lost.

The Truesdell stress rate of the Cauchy stress, $\dot{\boldsymbol{\sigma}}_t$, utilizes this fundamental relationship to build a relationship between the Cauchy stress and the 2nd Piola-Kirchoff stress known as the Piola transformation. By reorganizing Equation (2.4.5), we obtain

$$\boldsymbol{\sigma} = J^{-1}\mathbf{F} \cdot \mathbf{S} \cdot \mathbf{F}^{T}. \tag{2.4.8}$$

Now the stress rate is found to be

$$\dot{\boldsymbol{\sigma}} = J^{-1}\mathbf{F}\cdot\dot{\mathbf{S}}\cdot\mathbf{F}^{T} = J^{-1}\mathbf{F}\cdot[\frac{d}{dt}(J\mathbf{F}^{-1}\cdot\boldsymbol{\sigma}\cdot\mathbf{F}^{-T})]\cdot\mathbf{F}^{T}. \tag{2.4.9}$$

Now, we will define the Kirchhoff stress, $\boldsymbol{\tau}$, where

$$\boldsymbol{\tau} = J\boldsymbol{\sigma} \tag{2.4.10}$$

and the Lie derivative of the Kirchhoff stress,

$$\mathcal{L}_{\varphi}[\boldsymbol{\tau}] = \mathbf{F}\cdot[\frac{d}{dt}(\mathbf{F}^{-1}\cdot\boldsymbol{\tau}\cdot\mathbf{F}^{-T})]\cdot\mathbf{F}^{T}. \tag{2.4.11}$$

By substituting Equation (2.4.11) and Equation (2.4.10) into Equation (2.4.9) we yield

$$\dot{\boldsymbol{\sigma}}_{t} = J^{-1}\mathcal{L}_{\varphi}[\boldsymbol{\tau}]. \tag{2.4.12}$$

Equation (2.4.9) may then be simplified into the most common form for the Treusdell rate of the Cauchy stress

$$\dot{\boldsymbol{\sigma}}_{t} = \dot{\boldsymbol{\sigma}} - \mathbf{l}\cdot\boldsymbol{\sigma} - \boldsymbol{\sigma}\cdot\mathbf{l}^{T} + tr(\mathbf{l})\boldsymbol{\sigma} \tag{2.4.13}$$

in which, $\mathbf{l}$, is the velocity gradient defined as

$$\mathbf{l} = \dot{\mathbf{F}}\cdot\mathbf{F}^{-1} \tag{2.4.14}$$

and

$$\dot{J} = tr(\mathbf{l}). \tag{2.4.15}$$

The second stress rate that should be identified is the Green-Naghdi rate of the Cauchy stress, $\dot{\boldsymbol{\sigma}}_{g}$. Recalling Equation (2.4.6), let us assume that $\mathbf{U} = \mathbf{I}$ so we have $\mathbf{F} = \mathbf{R}$.Combining this with Equation (2.4.9) gives

$$\dot{\boldsymbol{\sigma}}_{g} = \mathbf{R}\cdot[\frac{d}{dt}(\mathbf{R}^{-1}\cdot\boldsymbol{\sigma}\cdot\mathbf{R}^{-T})]\cdot\mathbf{R}^{T} = \mathbf{R}\cdot[\frac{d}{dt}(\mathbf{R}^{T}\cdot\boldsymbol{\sigma}\cdot\mathbf{R})]\cdot\mathbf{R}^{T}. \tag{2.4.16}$$

This can be simplified to give the common form of the Green-Naghdi rate

$$\dot{\boldsymbol{\sigma}}_g = \dot{\boldsymbol{\sigma}} + \boldsymbol{\sigma}\cdot\boldsymbol{\Omega} - \boldsymbol{\Omega}\cdot\boldsymbol{\sigma} \tag{2.4.17}$$

where

$$\boldsymbol{\Omega} = \dot{\mathbf{R}}\cdot\mathbf{R}^T . \tag{2.4.18}$$

$$\mathbf{R}\cdot\mathbf{R}^T = \mathbf{I} \tag{2.4.19}$$

and

$$\dot{\mathbf{R}}\cdot\mathbf{R}^T = -\mathbf{R}\cdot\dot{\mathbf{R}}^T . \tag{2.4.20}$$

The Jaumann rate of the Cauchy stress is simply a specialized version of the Truesdell rate and is expressed as

$$\dot{\boldsymbol{\sigma}}_j = \dot{\boldsymbol{\sigma}} + \boldsymbol{\sigma}\cdot\mathbf{w} - \mathbf{w}\cdot\boldsymbol{\sigma} \tag{2.4.21}$$

where $\mathbf{w}$ is the spin tensor or screw part of the velocity gradient defined as

$$\mathbf{w} = \dot{\mathbf{R}}\cdot\mathbf{R}^T = \boldsymbol{\Omega} \tag{2.4.22}$$

for pure rigid body motion.

With these objective rates defined, a new reference configuration is considered in a simpler form

$$\dot{\hat{\boldsymbol{\sigma}}} = \hat{\mathbf{E}} : \hat{\mathbf{d}}^e = \hat{\mathbf{E}} : (\hat{\mathbf{d}} - \hat{\mathbf{d}}^p) \tag{2.4.23}$$

where $\mathbf{d}$ is the rate of deformation tensor. In order to calculate the incremental stress, we must first assume that the displacement field at a current frame is known and a trial stress is defined in order to find the next incremental frame. This trial elastic stress is illustrated as

$$\hat{\boldsymbol{\sigma}}^{tr}_{n+1} = \hat{\boldsymbol{\sigma}}_n + \mathbf{E} : \hat{\mathbf{d}}\Delta t \tag{2.4.24}$$

in which

$$\boldsymbol{\sigma}_{n+1}^{tr} = \mathbf{Q}_{n+1} \cdot \hat{\boldsymbol{\sigma}}_{n+1}^{tr} \cdot \mathbf{Q}_{n+1}^{T} \tag{2.4.25}$$

to follow Equation (2.4.1). Utilizing Equation (2.4.6), we can define the rate of deformation tensor as

$$\hat{\mathbf{d}} = \mathbf{Q}^{T} \cdot \mathbf{d} \cdot \mathbf{Q} = \frac{1}{2}\mathbf{Q}^{T} \cdot \mathbf{R} \cdot (\dot{\mathbf{U}} \cdot \mathbf{U}^{-1} + \mathbf{U}^{-1} \cdot \dot{\mathbf{U}}) \cdot \mathbf{R}^{T} \cdot \mathbf{Q}. \tag{2.4.26}$$

Assuming that the reference frame is the same as the configuration at time $t = t_n$, we can assume that

$$\mathbf{Q}_n = \mathbf{I}. \tag{2.4.27}$$

Also, it is safe to assume that

$$\mathbf{Q}(t) = \mathbf{R}(t). \tag{2.4.28}$$

Utilizing these assumptions, it is then possible to simplify Equation (2.4.26)

$$\hat{\mathbf{d}} = \frac{1}{2}(\dot{\mathbf{U}} \cdot \mathbf{U}^{-1} + \mathbf{U}^{-1} \cdot \dot{\mathbf{U}}). \tag{2.4.29}$$

Adopting the midpoint rule results in Equation (2.4.29) to be

$$\hat{\mathbf{d}}\Delta t = \frac{1}{2}(\Delta\mathbf{U} \cdot \mathbf{U}^{-1}_{n+\frac{1}{2}} + \mathbf{U}^{-1}_{n+\frac{1}{2}} \cdot \Delta\mathbf{U}) \tag{2.4.30}$$

in which $\Delta\mathbf{U}$ and $\mathbf{U}_{n+\frac{1}{2}}$ correspond to each other as

$$\Delta\mathbf{U} = \mathbf{U}_{n+1} - \mathbf{U}_n, \ \mathbf{U}_{n+\frac{1}{2}} = \frac{1}{2}(\mathbf{U}_{n+1} + \mathbf{U}_n). \tag{2.4.31}$$

Now, the trial stress in Equation (2.4.25) can be expressed as

$$\boldsymbol{\sigma}_{n+1}^{tr} = \mathbf{R}_{n+1} \cdot (\boldsymbol{\sigma}_n + \frac{1}{2}\mathbf{E} : (\Delta\mathbf{U} \cdot \mathbf{U}^{-1}_{n+\frac{1}{2}} + \mathbf{U}^{-1}_{n+\frac{1}{2}} \cdot \Delta\mathbf{U})) \cdot \mathbf{R}_{n+1}^{T}. \tag{2.4.32}$$

The next task that must be considered is to define the inverse of $\mathbf{U}$ in order to accurately

calculate the trial stress. Following Simo and Hughes (Simo and Hughes, 1998), we can assume

$$\mathbf{U}(t) = \exp[(t - t_n)\mathbf{C} / \Delta t] \tag{2.4.33}$$

where $\mathbf{C}$ is a constant tensor that will be defined momentarily. By differentiating Equation (2.4.33) with respect to time and substituting it into Equation (2.4.29), the following expression is yielded

$$\hat{\mathbf{d}} = \mathbf{C} / \Delta t \,. \tag{2.4.34}$$

The constant tensor, $\mathbf{C}$, in the reference frame, n, is simply

$$\mathbf{U}(t_n) = \exp(\mathbf{0}) = \mathbf{I} \quad at \ (\mathbf{X}, t_n) \tag{2.4.35}$$

and in the current frame, $n+1$, is

$$\mathbf{U}(t_{n+1}) = \exp(\mathbf{C}_{n+1}) \quad at \ (\mathbf{x}, t_{n+1}) \,. \tag{2.4.36}$$

With these two compatibility equations, and expressing $\mathbf{U}(t_{n+1})$ as $\mathbf{U}_{n+1}$, the constant tensor can be expressed as

$$\mathbf{C}_{n+1} = \ln \mathbf{U}_{n+1} = \frac{1}{2} \ln \mathbf{U}_{n+1}^2 = \frac{1}{2} \ln(\mathbf{F}_{n+1}^T \cdot \mathbf{F}_{n+1}) \,. \tag{2.4.37}$$

Equation (2.4.37) shows that $\mathbf{C}$ embodies the incremental natural strain tensor between the reference frame and the current frame. Utilizing this new equation, Equation (2.4.32) may now be expressed as

$$\boldsymbol{\sigma}_{n+1}^{tr} = \mathbf{R}_{n+1} \cdot (\boldsymbol{\sigma}_n + \mathbf{E} : \mathbf{C}_{n+1}) \cdot \mathbf{R}_{n+1}^T \,. \tag{2.4.38}$$

This trial stress then follows the same procedure as described before to evaluate the final stress in the current configuration.

2.5 Damage Theory

As an expansion to this plasticity theory, this investigation should mention the effects of damage bestowed upon the material. First, it is important to introduce the initial damage density of the material, ϕ, which ranged from 0 to 1. Since the plasticity theory explained in (Voyiadjis et al., 2006) considers an effective medium with no damage, it is important to modify the stress of the damaged material to simulate that of an undamaged behavior. In other words, we create a new trial effective stress as

$$\bar{\sigma}_{ij} = \frac{\sigma_{ij}}{1-\phi} \tag{2.5.1}$$

With this effective stress, we may now execute the previous iterative plasticity calculations to obtain the effective stress for the next increment or $\bar{\sigma}_{ij}^{n+1}$. From the relationship described in Equation (1.32), the true stress, or stress of the damaged material at may be found. Before restarting this process, it is important to note that the damage density of metals increase through each increment of loading or strain. Thus, the damage density must also be updated at each increment since

$$\phi_{n+1} = \phi_n + \dot{\phi} \tag{2.5.2}$$

This damage density variable is found based on Lemaitre's damage model for metals (Lemaitre, 1992). The change in damage density, $\dot{\phi}$, according to Lemaitre is a function of the energy involved in each process or increment represented by a state variable, and a dissipation potential:

$$\dot{\phi} = \left(\frac{Y}{S}\right)^{P} \dot{\lambda} \tag{2.5.3}$$

where Y is the strain energy density release rate at each interval as

$$Y_{n+1} = Y_n + \frac{1}{2}\left|\dot{\sigma}_{ij}\dot{\varepsilon}^e_{ij}\right| \tag{2.5.4}$$

S is the total damage strength or energy, and P is the damage exponent. From these relationships, ϕ may be found for each iteration. Figure 4 illustrates a summary of this process when damage is considered.

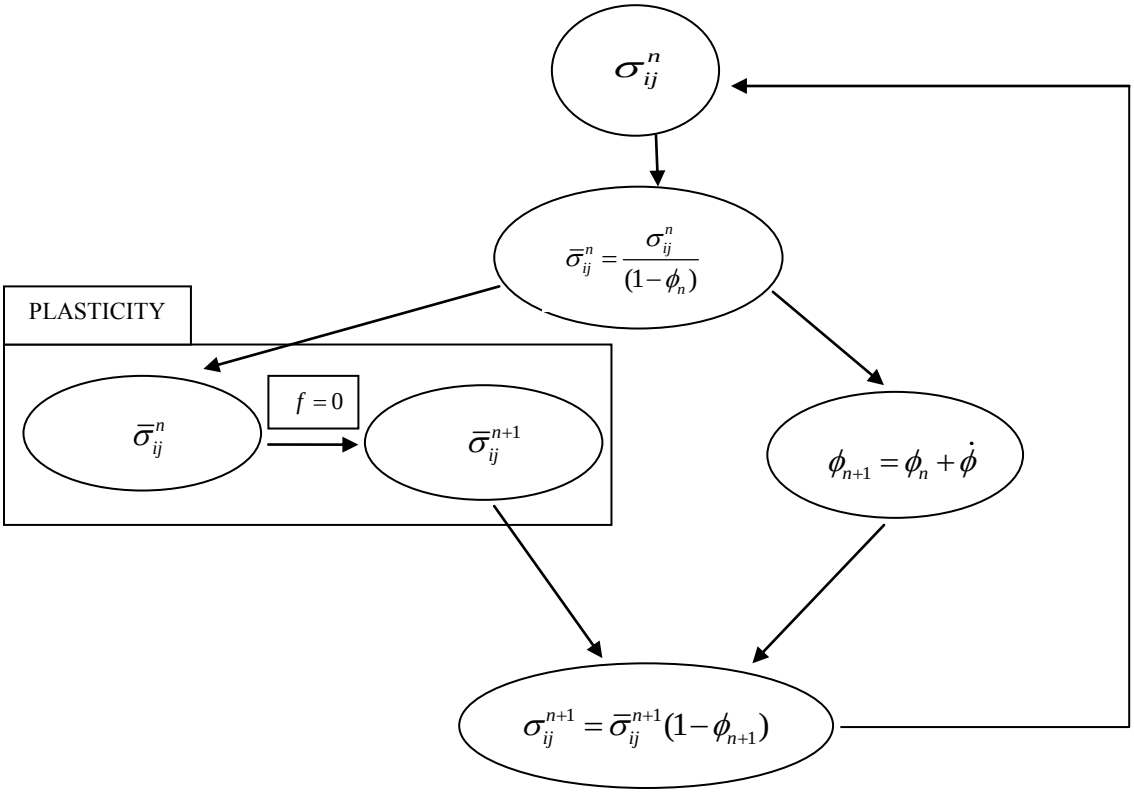

Figure 4 Summary of calculating stress with damage consideration

3. SIMULATION METHOD

An innovative RVE generator software called RVE_Maker was created for this project by Ardeshir Tehrani utilizing Borland C++ Builder 6.0. A variety of detailed parameters may be specified to construct an arbitrary representative volume element (RVE) of a microstructure with multiple phases of regular and/or irregular shapes. The irregular shapes are constructed through Fourier series analysis. Thus, a higher degree allows for a more irregular shape. Specified parameters, such as average radius, of particles or constituents define the fundamental basis of each phase. This RVE generator was utilized to construct 50 μm x 50 μm RVE's with three or four phases depending on the group under analysis. This software assures that particles are positioned or dispersed throughout the microstructure so as they do not intersect other constituents. After this, RVE_Maker creates a script file compatible with AutoCAD to draw the geometry. Once this is drawn in AutoCAD, the corresponding Python code is generated which allows the microstructure to be imported into ABAQUS where properties, loading conditions, and meshing parameters may be specified to create a complete finite element representation as a CAE file. Typical volume fractions and diameters for each phase in TRIP steels usually vary as illustrated in Table 1 (Uthaisangsuk et al., 2008; Zrnik et al., 2006).

Table 1 Typical volume fractions and grain diameters for TRIP steel (Uthaisangsuk et al., 2008; Zrnik et al., 2006)

Microstructure	Volume Fraction (%)	Grain Diameter (μm)
Ferrite	50-60	10-20
Retained Austenite	5-15	1-4
Martensite	0-15	1-4
Bainite	25-40	5-10

There will be five groups that will be studied here. Group 1 will consist of TRIP steel with specified volume fractions of each phase and will serve as the control. Group 2 will illustrate the similar parameters as the TRIP steel in Group 1, except with silicon carbide inclusions reinforcing the matrix . Group 3,4, and 5 will each contain the same parameters as Group 2 with the exception that the ceramics presented in the microstructure are now pure cementite (Fe_3C), zirconia, and 99.9% pure aluminum oxide, respectively. All groups will experience isothermal conditions, in which temperature will not vary. For clarification, Table 2 illustrates a summary of each group. Specific parameters for each case within each group will be described momentarily.

Table 2 Summary of analysis

GROUP	MICROSTRUCTURE	INCLUSION MATERIAL
1	TRIP	NONE
2	TRIP w/ inclusions	SILICON CARBIDE
3	TRIP w/ inclusions	CEMENTITE
4	TRIP w/ inclusions	ZIRCONIA
5	TRIP w/ inclusions	99.9% PURE ALUMINUM OXIDE

3.1 Elastic and Plastic Properties

The elastic and plastic parameters utilized in this experiment for each phase are illustrated in Table 3, Table 4, and Figure 5 (Choi, 2009; Choi et al., 2009; Choi et al., 2010; Delannay et al., 2008; Lani et al., 2007; Muransky et al., 2006; Sakaki et al., 1990; Sierra and Nemes, 2008).

Table 3 Elastic properties of TRIP steel phases (Choi, 2009; Choi et al., 2009; Choi et al., 2010; Delannay et al., 2008; Lani et al., 2007; Muransky et al., 2006; Sakaki et al., 1990; Sierra and Nemes, 2008)

Phase	E (MPa)	v
Ferrite	225000	0.3
Austenite	215000	0.3
Bainite	210000	0.3
Martensite	215000	0.3

Table 4 Plastic properties of TRIP steel phases (Choi, 2009; Choi et al., 2009; Choi et al., 2010; Delannay et al., 2008; Lani et al., 2007; Muransky et al., 2006; Sakaki et al., 1990; Sierra and Nemes, 2008)

Phase	$\sigma_{y,i}$ **(MPa)**	K_i **(MPa)**	η_i
Ferrite (i=F)	425	1200	0.6
Austenite (i= A)	570	1910	0.64
Bainite (i=B)	500	3400	0.65
Martensite (i=M)	3200	2000	1

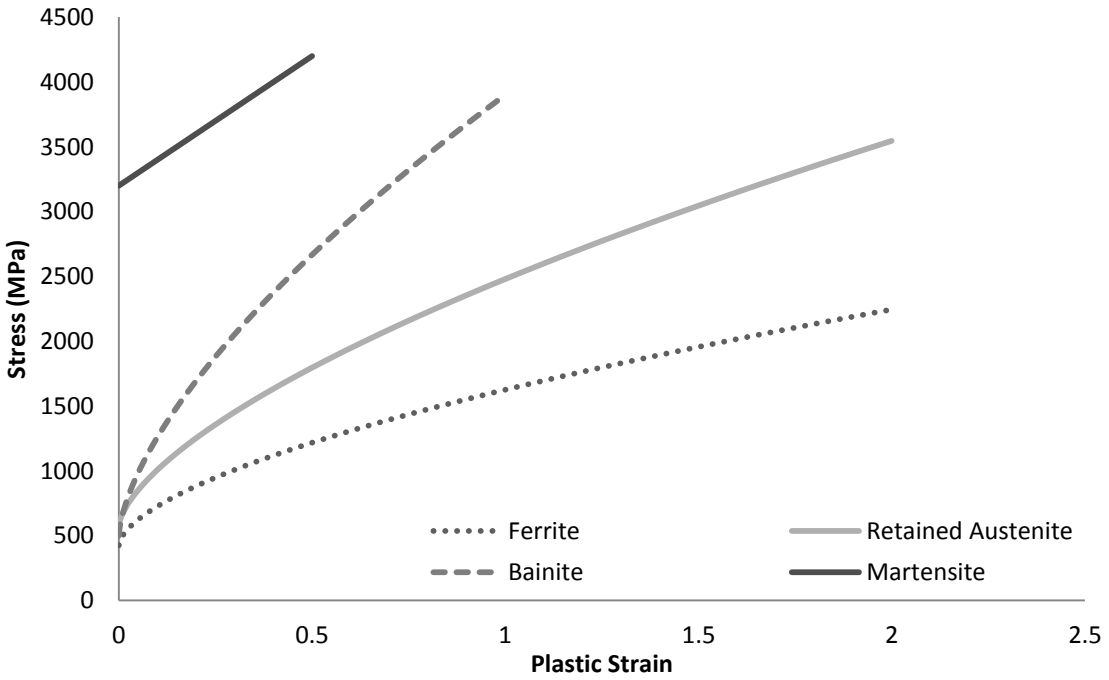

Figure 5 Stress vs. plastic strain behavior of TRIP steel phases

Due to the addition of reinforcing ceramic particles, it is also important to state their properties and expected behavior in this investigation. As explained previously, the

ceramics that will be utilized in this investigation are silicon carbide (SiC), pure cementite (Fe_3C), zirconia (ZrO_2), and 99.9% pure aluminum oxide (Al_2O_3). Due to the hardness and brittleness of these ceramics, the particles are expected to have elastic behavior with no plastic deformation, thus only the elastic properties in Table 5 are applicable (Callister, 2007; Umemoto et al., 2003) .

Table 5 Ceramic elastic properties (Callister, 2007; Umemoto et al., 2003)

Ceramic	**E (GPa)**	**v**
Silicon Carbide (SiC)	480	0.16
Cementite (Fe_3O)	190	0.32
Zirconia (ZrO_2)	205	0.31
99.9% Aluminum oxide (Al_2O_3)	380	0.22

It is important to note that parameters vary with different papers. The parameters in Tables 3 -5 were chosen in order to have the ability to compare the simulations in this investigation with the results of other coinciding studies.

3.2 Group 1 Description

The first group of RVE's are generated as three phase microstructures to simulate TRIP steel. Each phase is assigned their corresponding elastic and plastic material

properties in accordance to previous experiments and expected to follow the elastic behavior and the plastic theory previously described. Within this group, there will be two subgroups with some varying constituent volume fractions in order to get a range of the behavior of the pure TRIP steel "matrix" before and after transformation. For this study, grain diameter will not be varied for the constituent phases in the TRIP "matrix". The ferrite matrix grain diameter is not specified since it is considered the matrix and depends solely on the size of the other included constituents. This is due to the fact that after the RVE is generated with specific diameters for the "particle" constituents, the remaining area is defined as the matrix, or ferrite. Tables 6 and 7 illustrate the specific volume fractions and grain diameters that will be assigned to each group.

Table 6 Subgroups and volume fraction for each phase

Subgroup	**A**	**At**
	Volume Fraction (%)	
Ferrite	60	60
Austenite	15	0
Martensite	0	15
Bainite	25	25

Table 7 Grain diameter for each phase

	Grain Diameter (μm)
Ferrite	-
Austenite	1
Martensite	1
Bainite	5

Subgroup A represents the original microstructure before transformation. Although it is rare, this research assumes that all of the meta-stable retained austenite transforms into martensite. Thus, the transformed microstructure is illustrated by Subgroup At. This study will perform each analysis on the beginning (Subgroup A) and final stage (Subgroup At) assuming perfect and complete phase transformation. This analysis will give us an understanding of the change in behavior of an original TRIP steel "matrix" to compare to previous studies and to provide a comparison to a ceramic particle reinforced TRIP steel composite. This generated microstructure is illustrated in Figure 6.

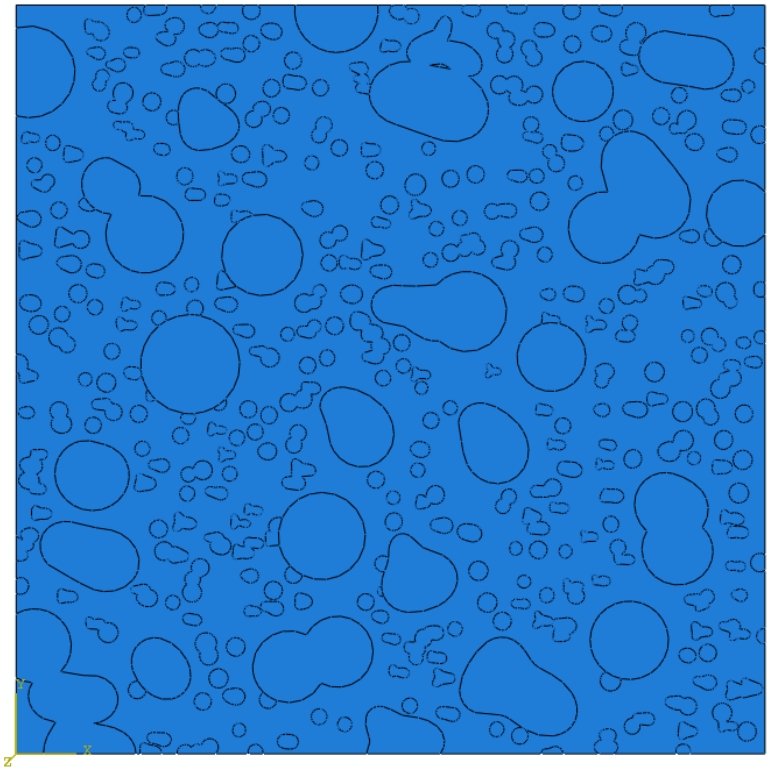

Figure 6 RVE for Group 1, Subgroups A and At

3.3 Group 2, 3, 4 and 5 Description

Group 2-5 entail a more broad set of RVE's, yet the same elastic plastic ABAQUS analysis as in Group 1. In Groups 2-5, we introduce ceramic inclusions of uniform diameters. The same subgroups are introduced as before, except now, these subgroups are modified. This modification involves altering the volume fractions of the ferrite matrix in order to include the volume fraction of the ceramic particles as illustrated in Table 8. The retained austenite and martensite volume fractions are not altered since these two phases act as particles themselves in the composite as a whole and are involved with the transformation behavior. The particles are introduced in order

to reinforce the composite and this transformation, thus the phases that are not directly associated with this behavior are modified.

Table 8 Volume fraction for each volume group and corresponding subgroup

	Volume Group	i	ii	iii
Subgroup		**Volume Fraction (%)**		
	Ferrite	59	55	50
	Austenite	15	15	15
	Martensite	0	0	0
	Bainite	25	25	25
A	**Ceramic**	1	5	10
	Ferrite	59	55	50
	Austenite	0	0	0
	Martensite	15	15	15
	Bainite	25	25	25
At	**Ceramic**	1	5	10

The diameter for the ceramic inclusions is another parameter that must be addressed. Thus, Table 9 depicts an expanded version of the parameters introduced in Group 1 in which the diameters of the inclusions are specified. These microstructures are also pictured in Figures 7-9.

Table 9 Categories and corresponding trials for each volume group

	Grain diameter (μm)
Ferrite	-
Austenite	1
Martensite	1
Bainite	5
Silicon	0.5

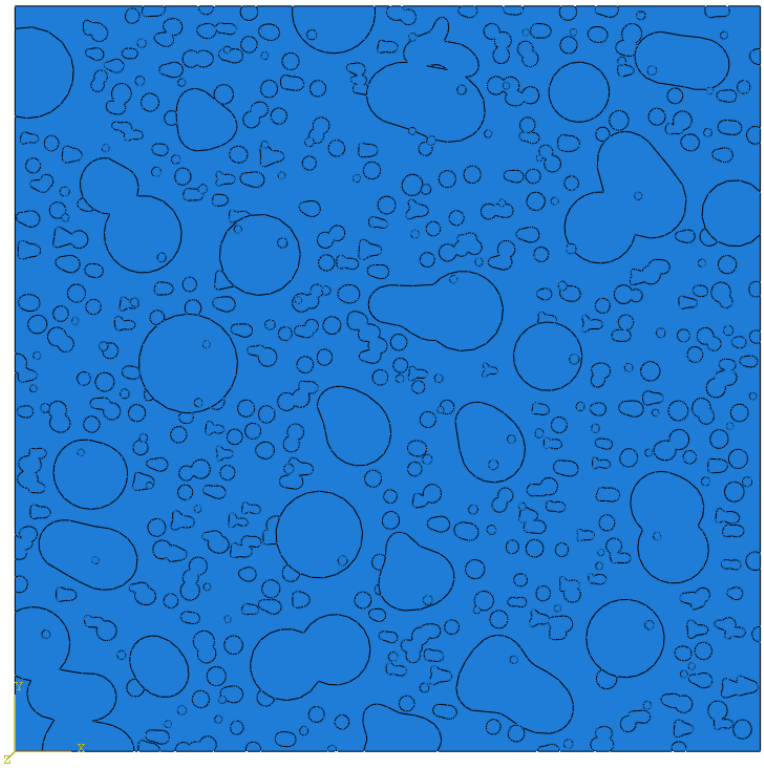

Figure 7 RVE for Subgroups Ai and Ati

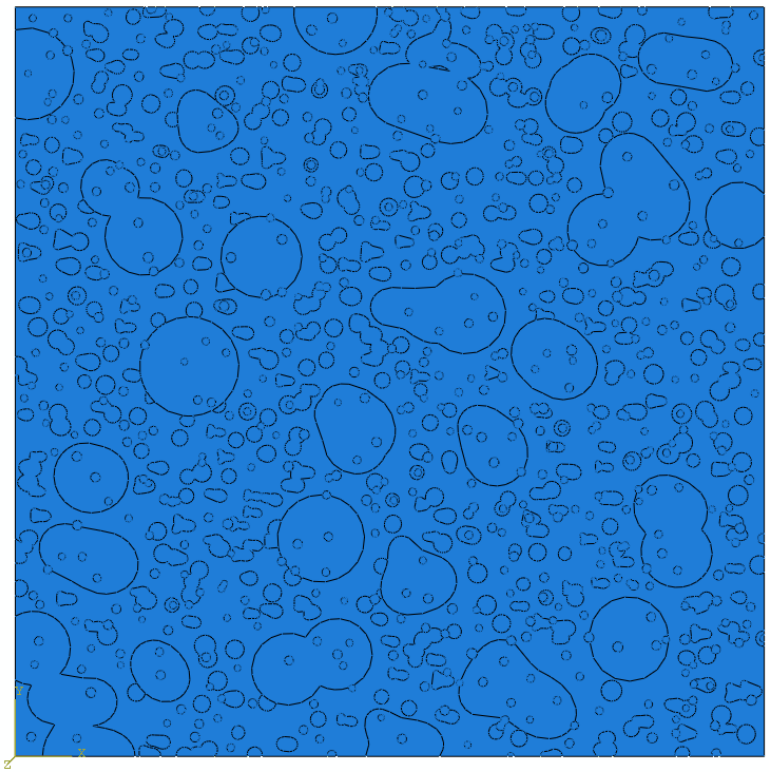

Figure 8 RVE for Subgroups Aii and Atii

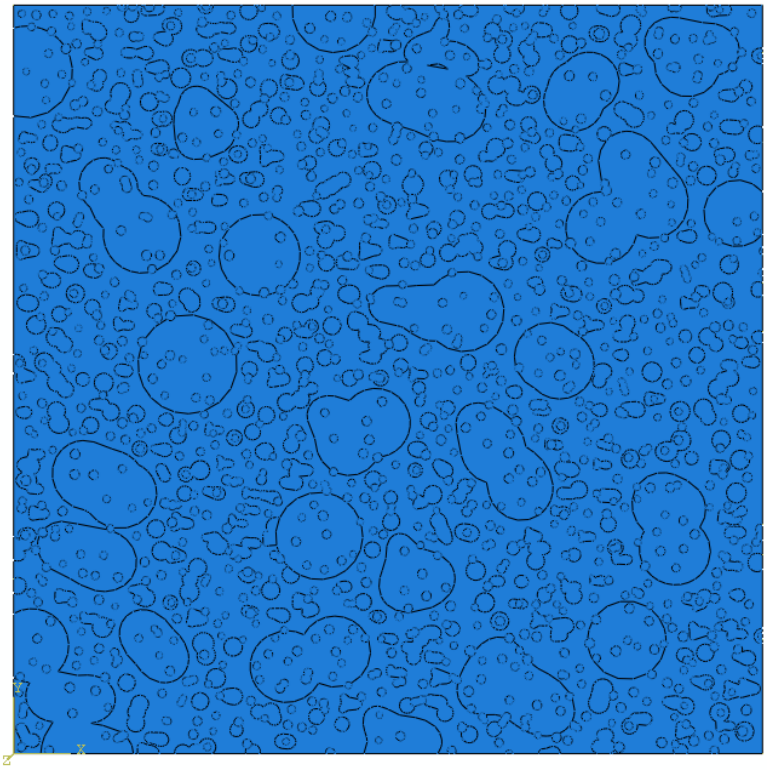

Figure 9 RVE for Subgroups Aiii and Atiii

3.4 Assumptions and Loading Conditions

There are a few assumptions that must be recognized and revisited for this study. As already described before, the materials utilized in this study are assumed to be isotropic. All phases are assumed to be perfectly bonded as well. Size effect, initial defects or geometric imperfections are not considered. Gradient theory is also neglected throughout this study.

In ABAQUS, after each RVE was assigned its proper properties, all microstructures experienced the same conditions as shown in Figures 10 and 11.

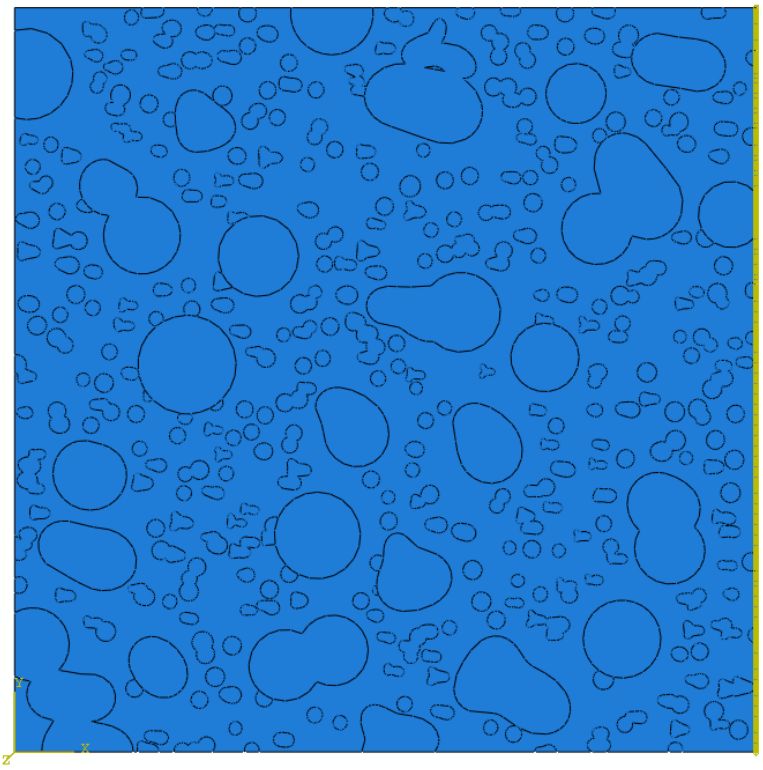

Figure 10 Connection of nodes on right side

Figure 10 illustrates that all the nodes on the right hand side of the microstructure are connected. This is done so the RVE will react as an actual specimen in which the right hand side will act as an actual edge. The nodes will follow the same behavior as its neighbors instead of experiencing high distortion to other locations independent of the neighboring nodes.

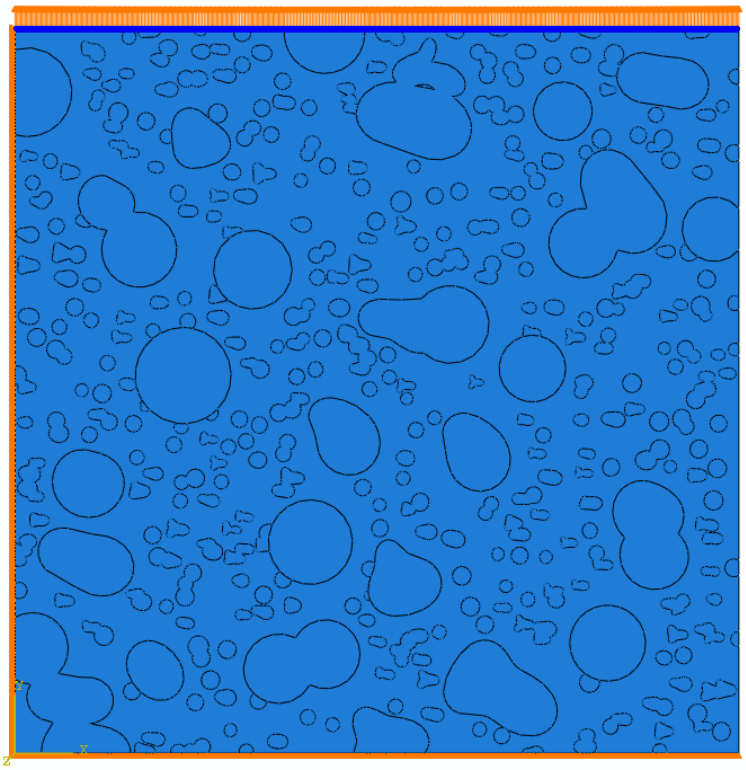

Figure 11 Boundary conditions and loading

Figure 11 illustrates the fixed boundary conditions at the base and left side of the microstructure. Also, the 50µm displacement on the top edge is also shown to simulate the 100% strain load. After these factors were identified and executed, the specimen was meshed. Figure 12 illustrates an example of a meshed microstructure.

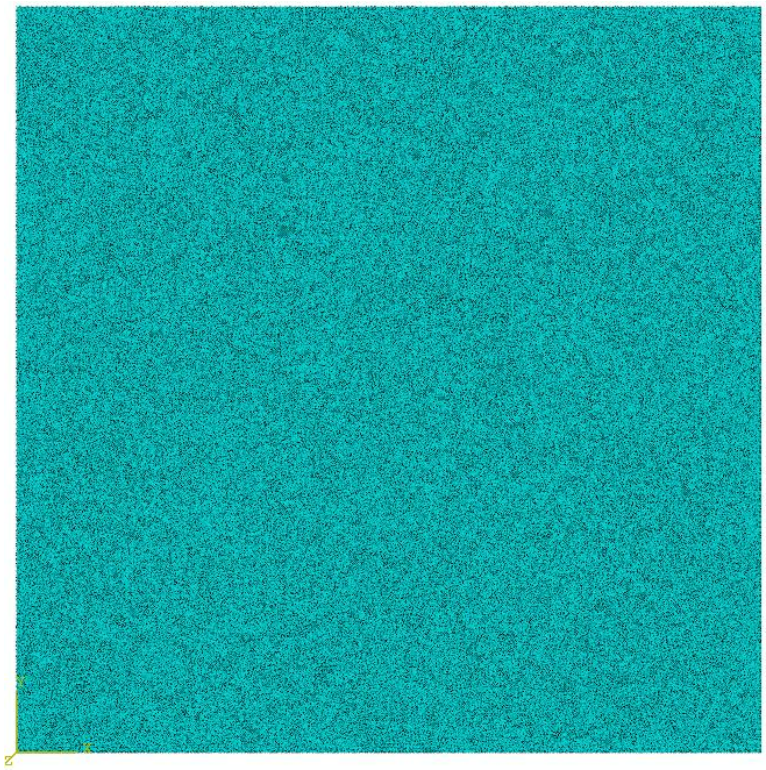

Figure 12 Meshed RVE for Group 1

4. RESULTS

4.1 Group 1- TRIP Steel With No Reinforcement

In Group I, only microstructures A and At were considered under elastic/plastic analysis with isothermal conditions. The first objective was to obtain the equivalent plastic strain (PEEQ) of each model and view where this strain localizes throughout the microstructure and what this proposes about failure in the microstructure. Strain localization allows for the determination of potential areas for cracks to begin and proliferate through the microstructure. For example, subgroup A, or the initial austenitic structure initially started the analysis at 0% strain. As the analysis continued, the following PEEQ output in Figures 13 - 37 were recorded at each corresponding percentage strain.

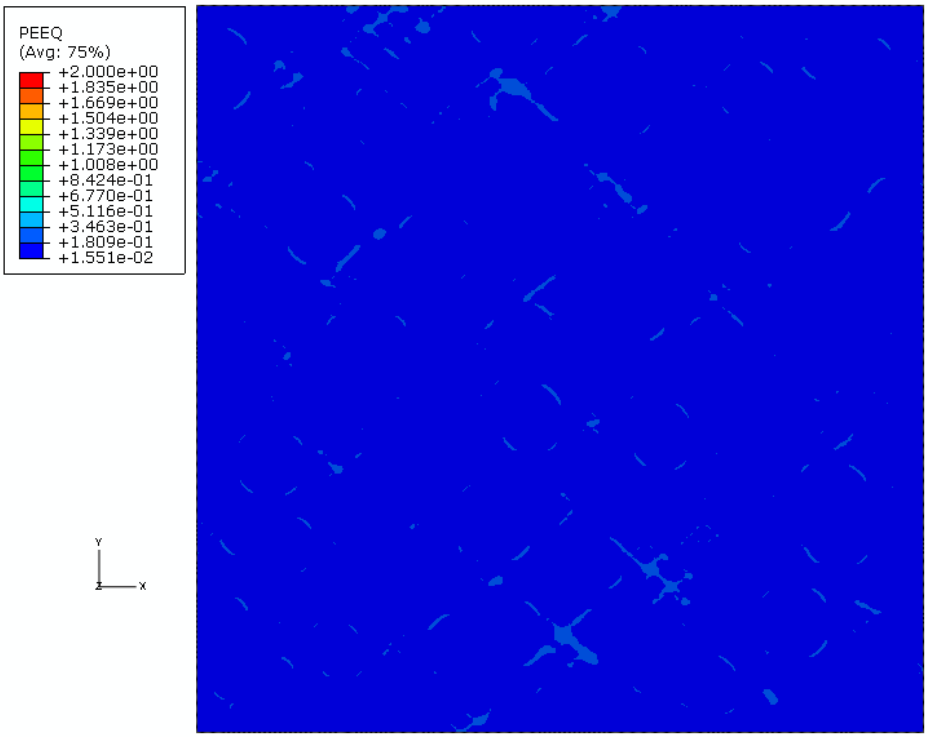

Figure 13 Subgroup A at 9% strain

Figure 13 at 9% strain begins to illustrate very small evidence of plastic strain, yet it begins to become more prevalent at 13% strain in Figure 14. From here, the microstructure continues to be loaded and the areas of strain localization become more prevalent.

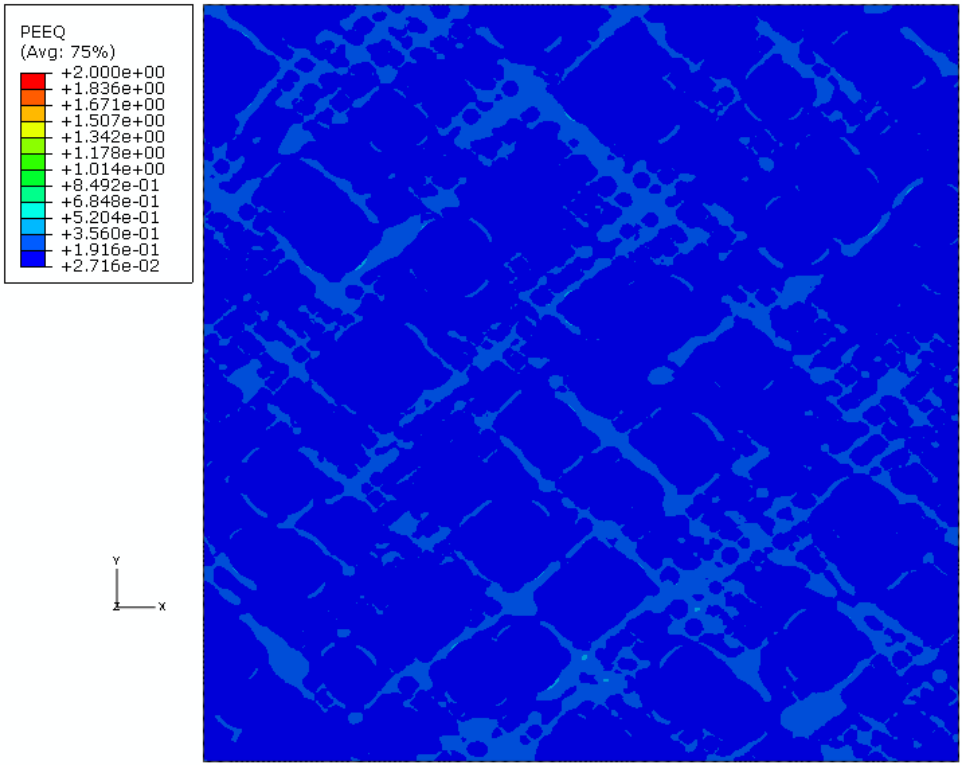

Figure 14 Subgroup A at 13% strain

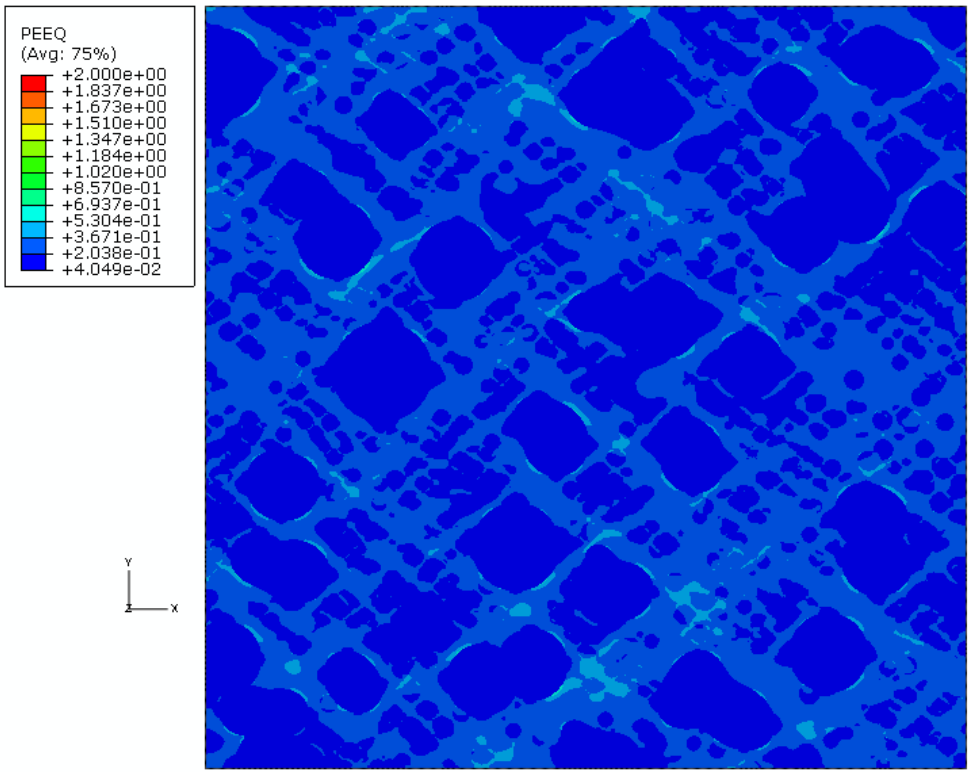

Figure 15 Subgroup A at 19% strain

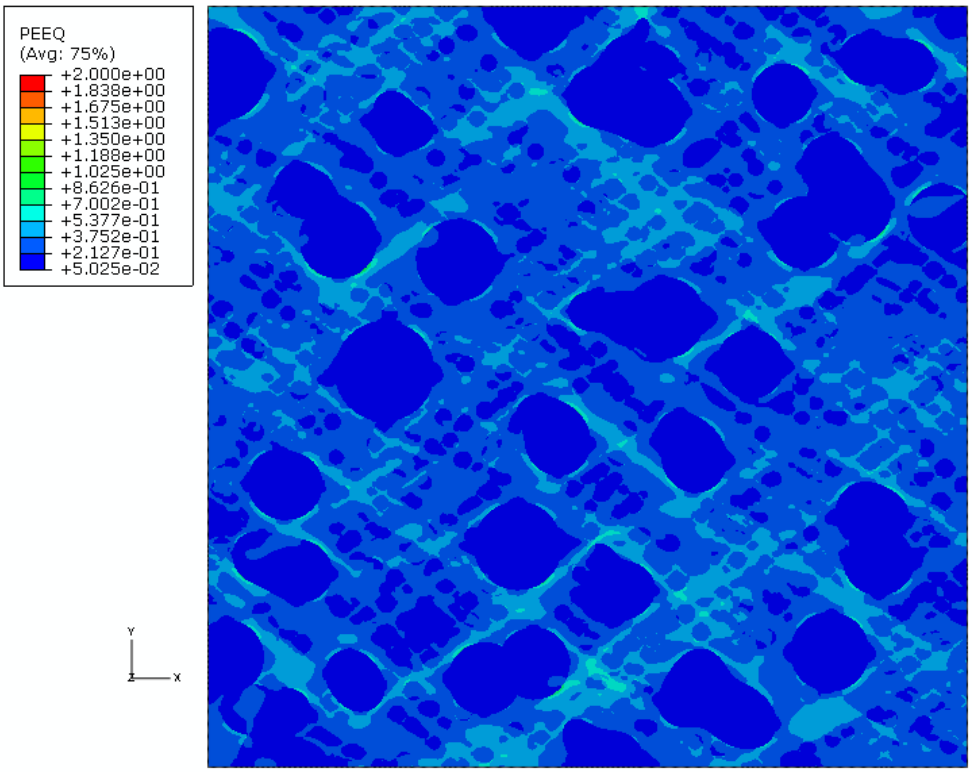

Figure 16 Subgroup A at 26% strain

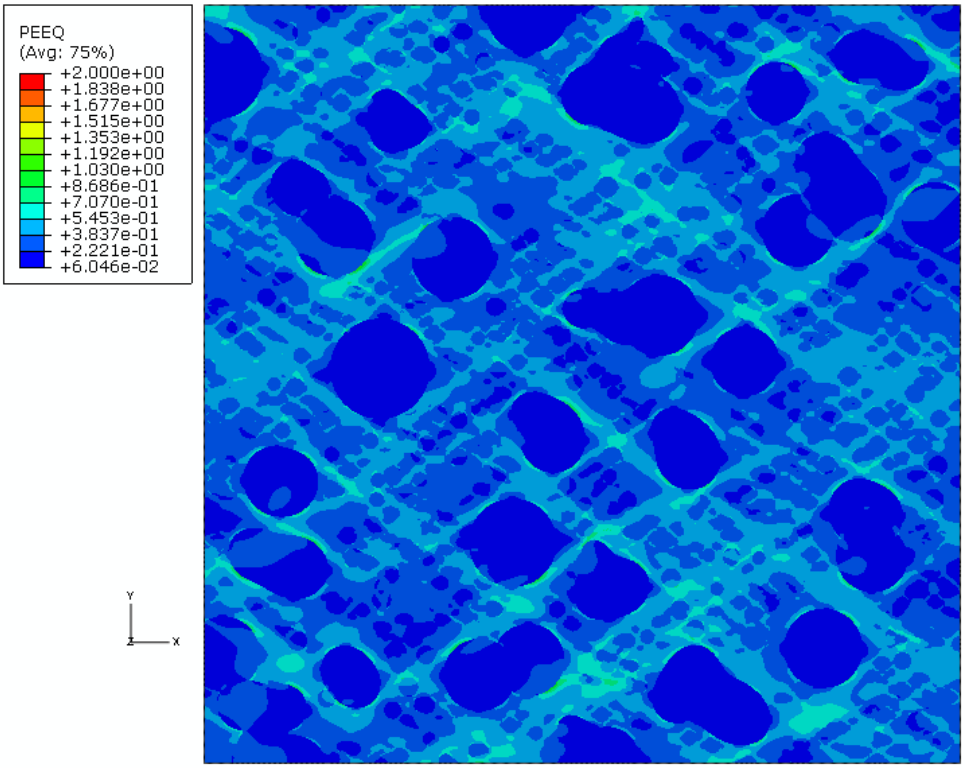

Figure 17 Subgroup A at 32% strain

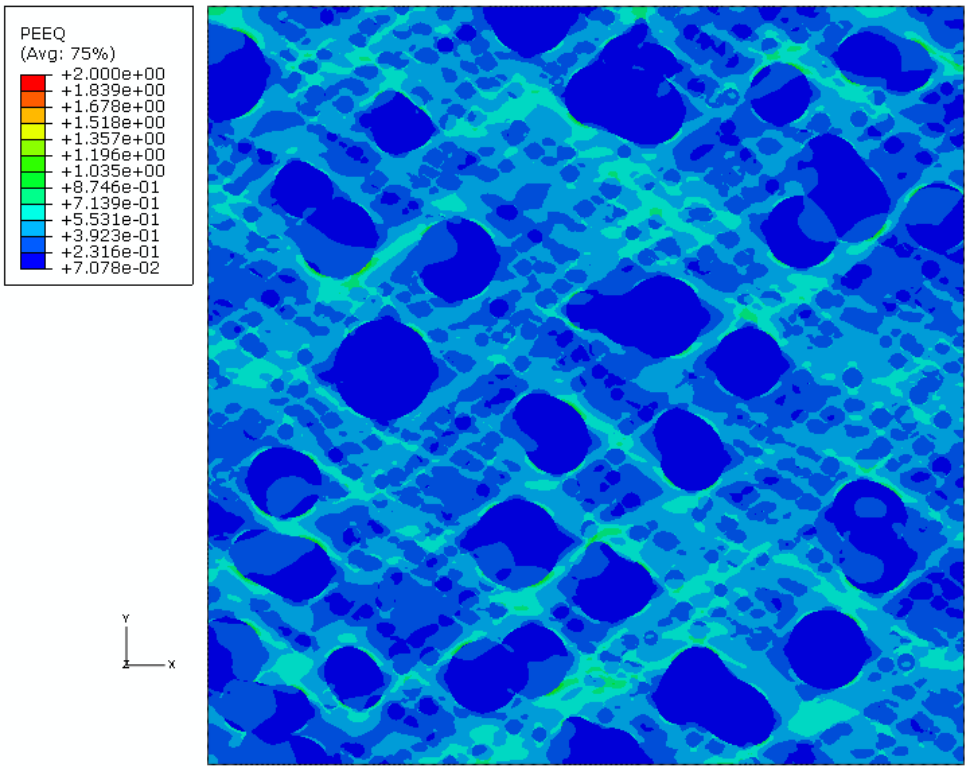

Figure 18 Subgroup A at 37% strain

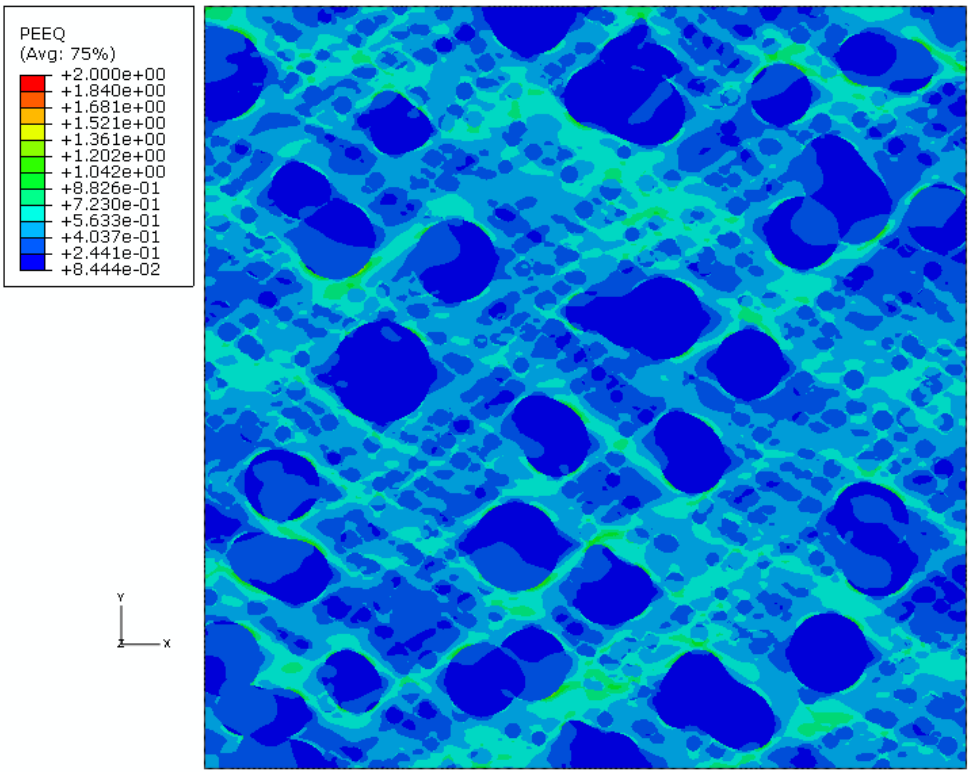

Figure 19 Subgroup A at 42% strain

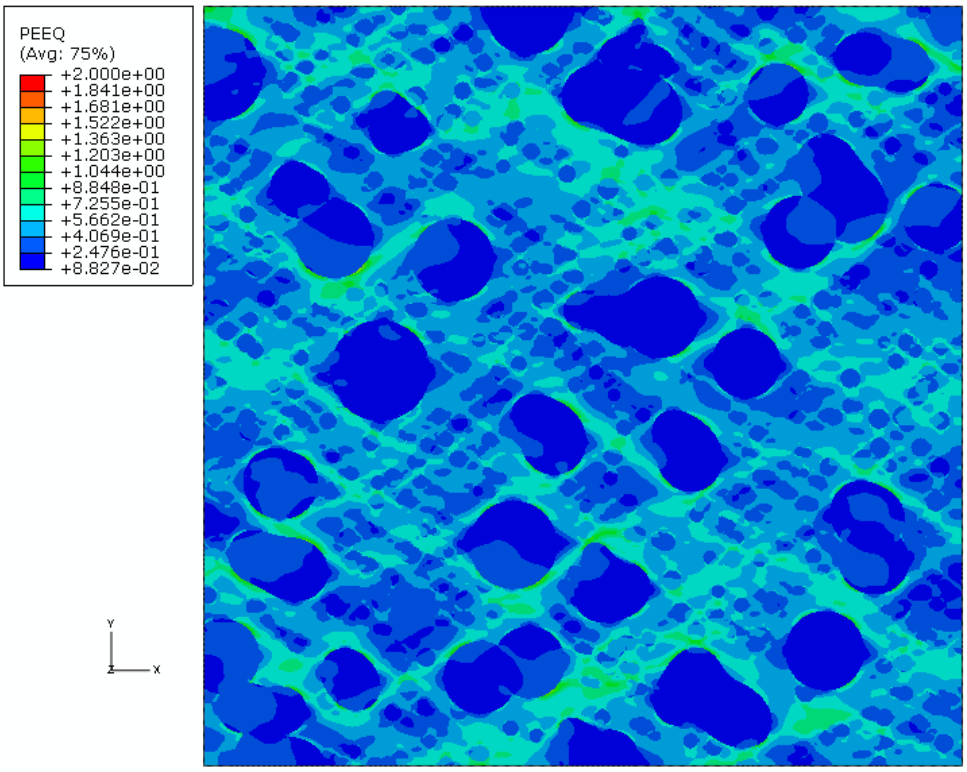

Figure 20 Subgroup A at 43% strain

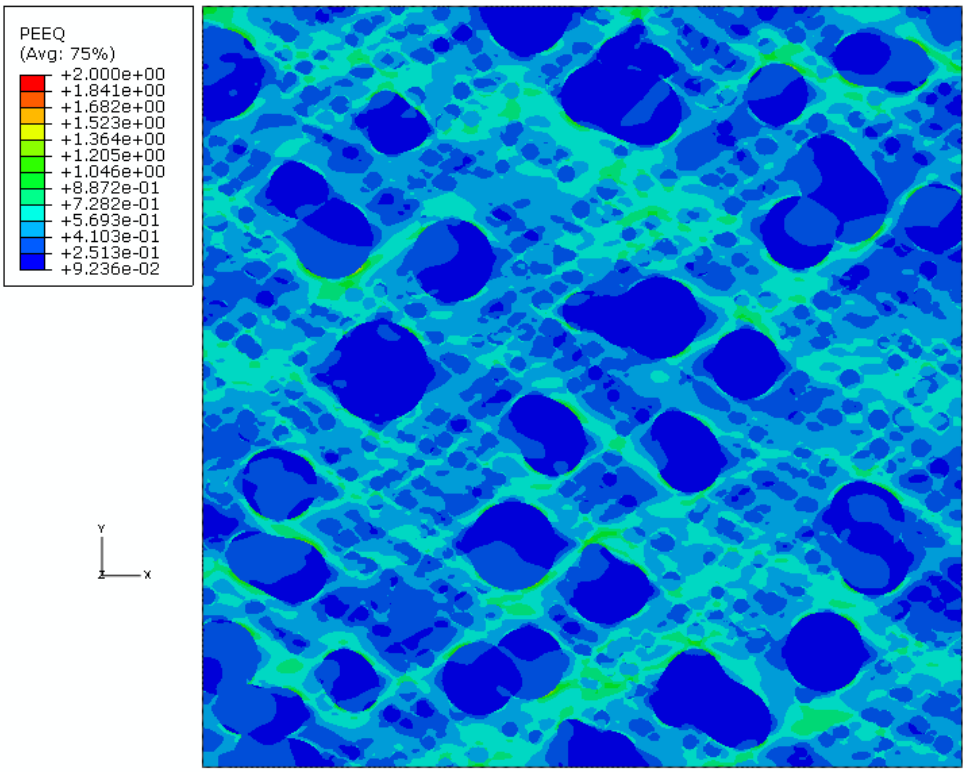

Figure 21 Subgroup A at 44% strain

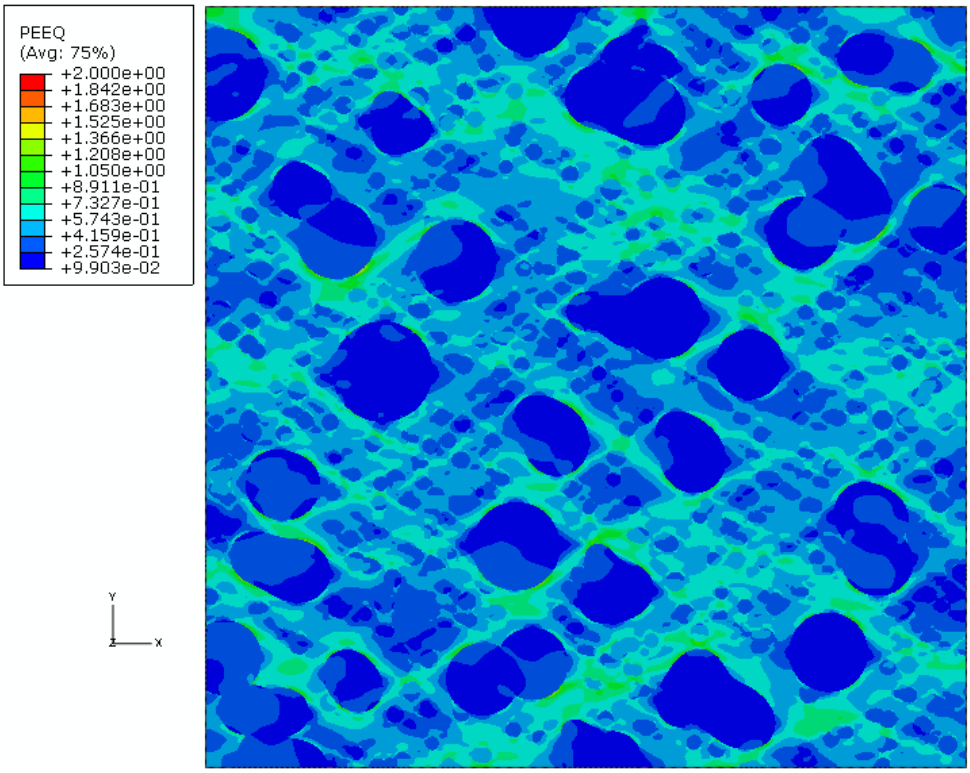

Figure 22 Subgroup A at 46% strain

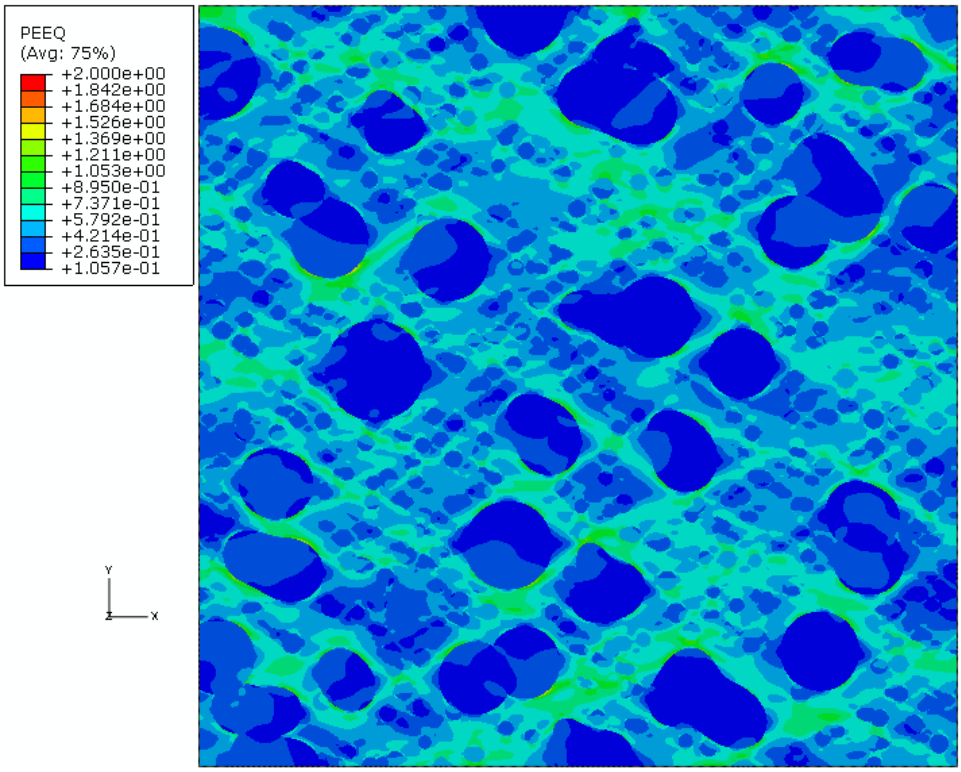

Figure 23 Subgroup A at 49% strain

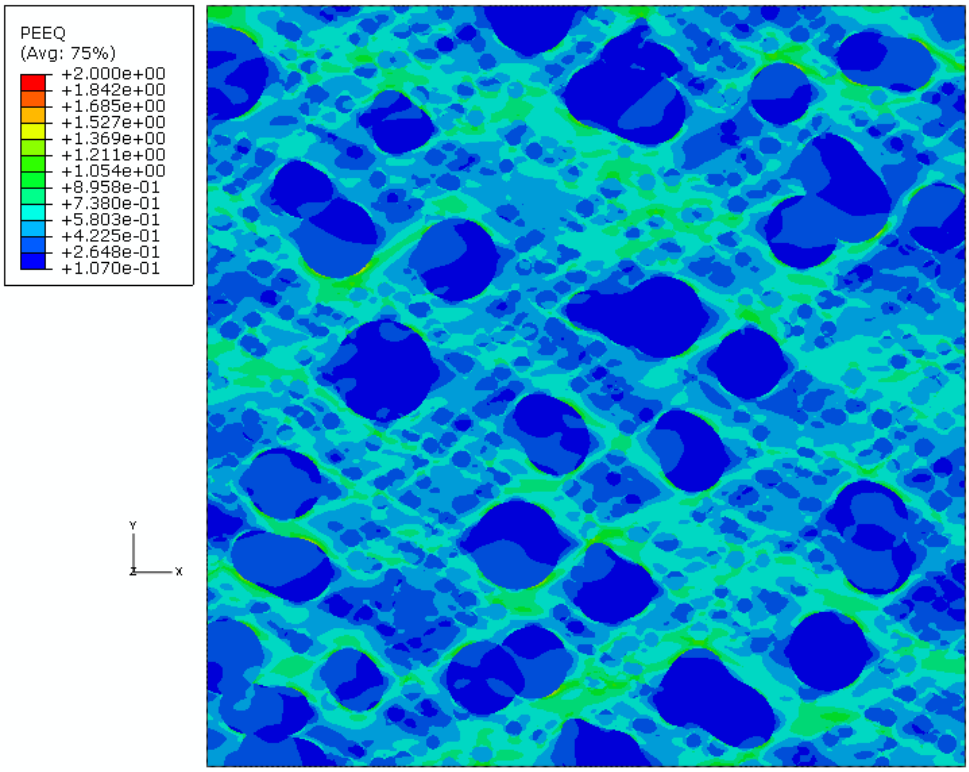

Figure 24 Subgroup A at 50% strain

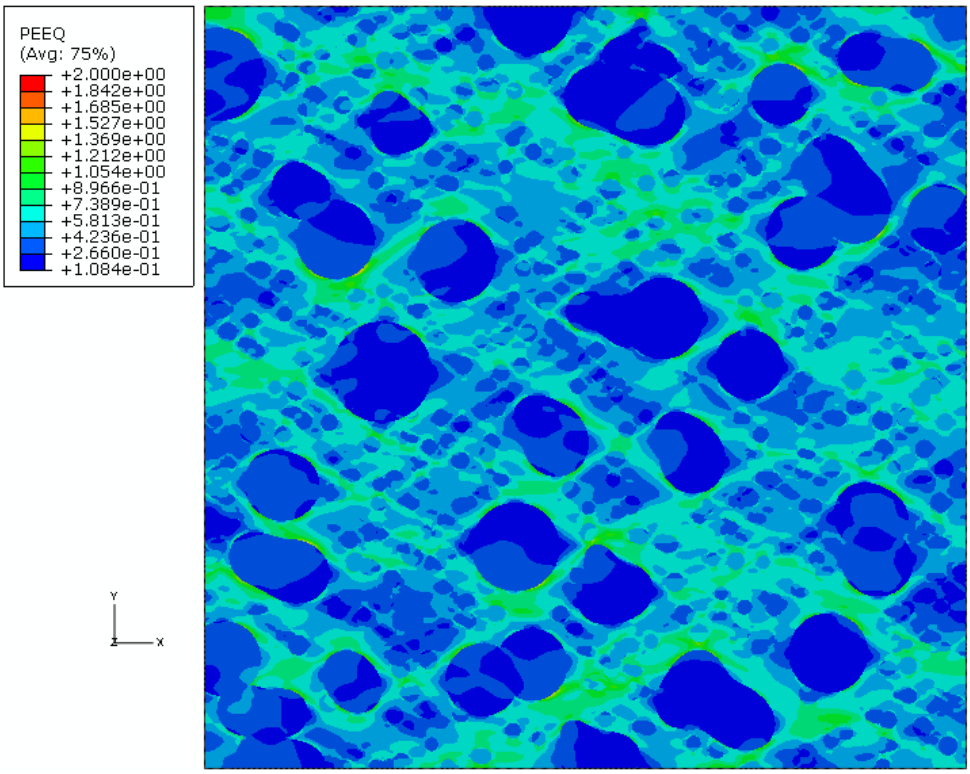

Figure 25 Subgroup A at 51% strain

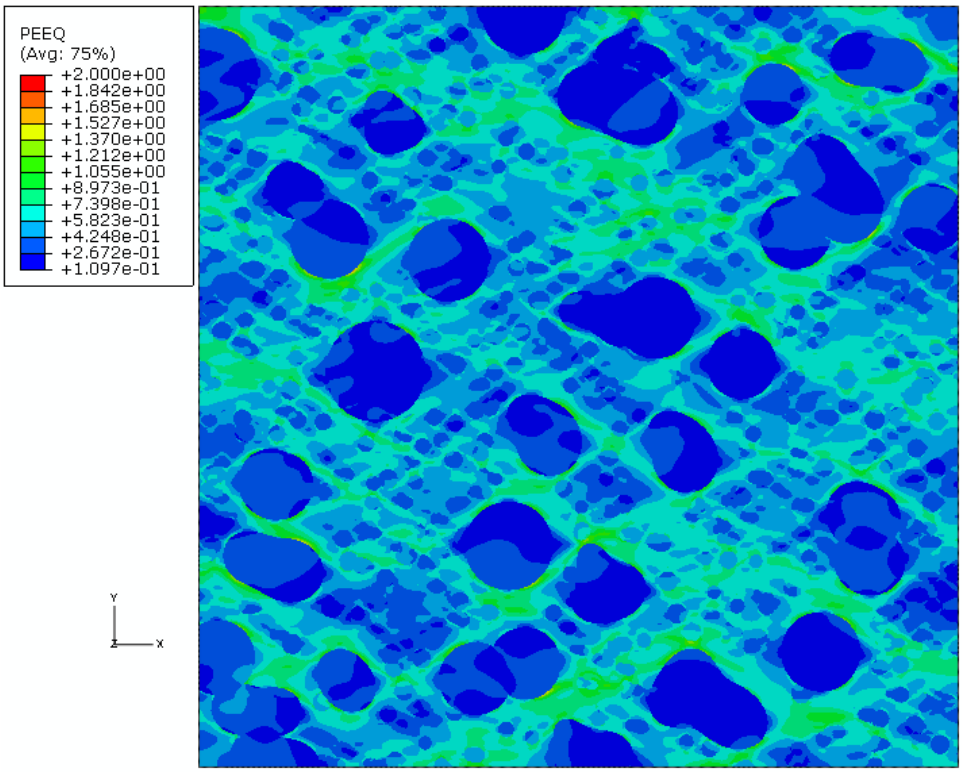

Figure 26 Subgroup A at 52% strain

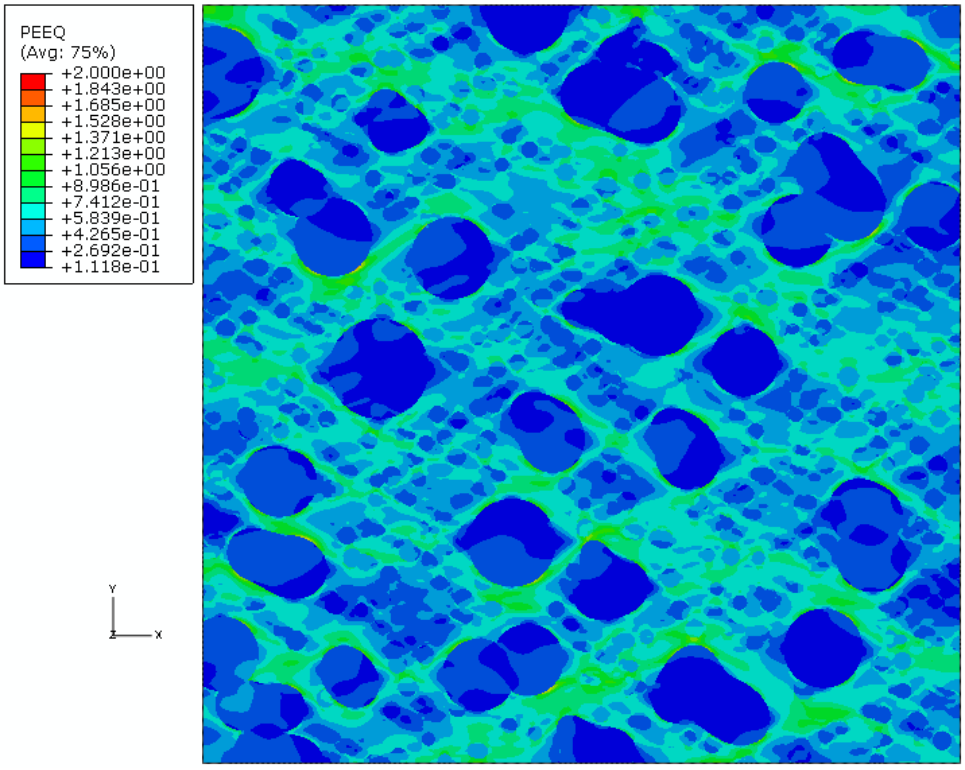

Figure 27 Subgroup A at 53% strain - ultimate tensile strength

Figure 27 illustrates the strain at the ultimate tensile strength for Subgroup A. The information at this strain becomes more important when we visit the stress vs. strain behavior of the microstructure and when compared to other microstructures and groups.

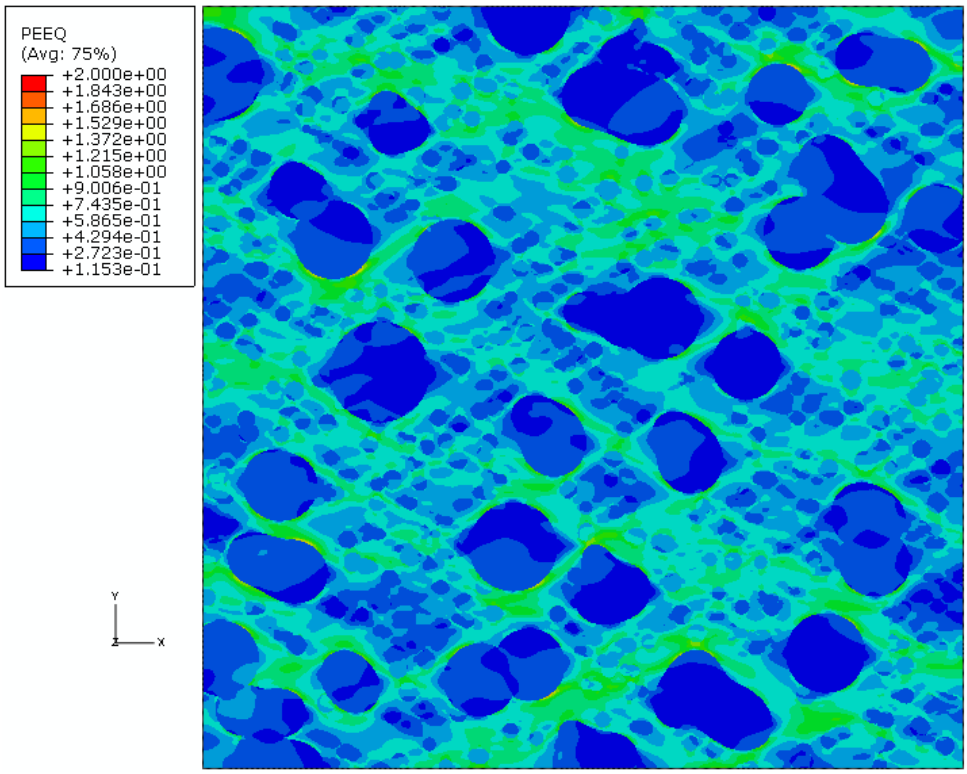

Figure 28 Subgroup A at 56% strain

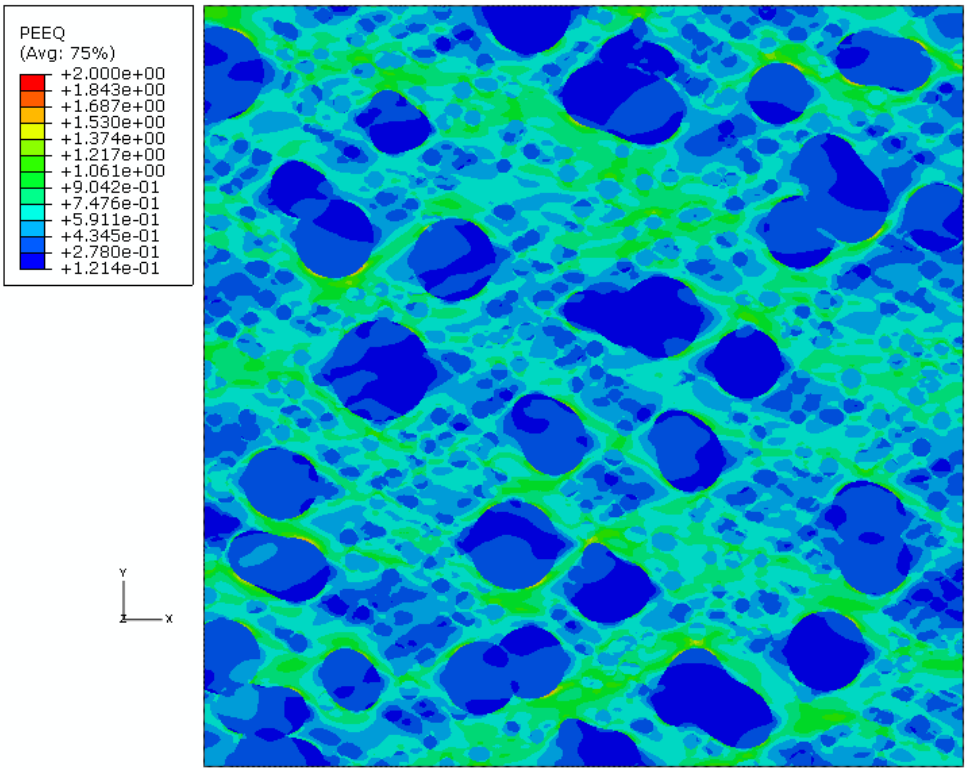

Figure 29 Subgroup A at 60% strain

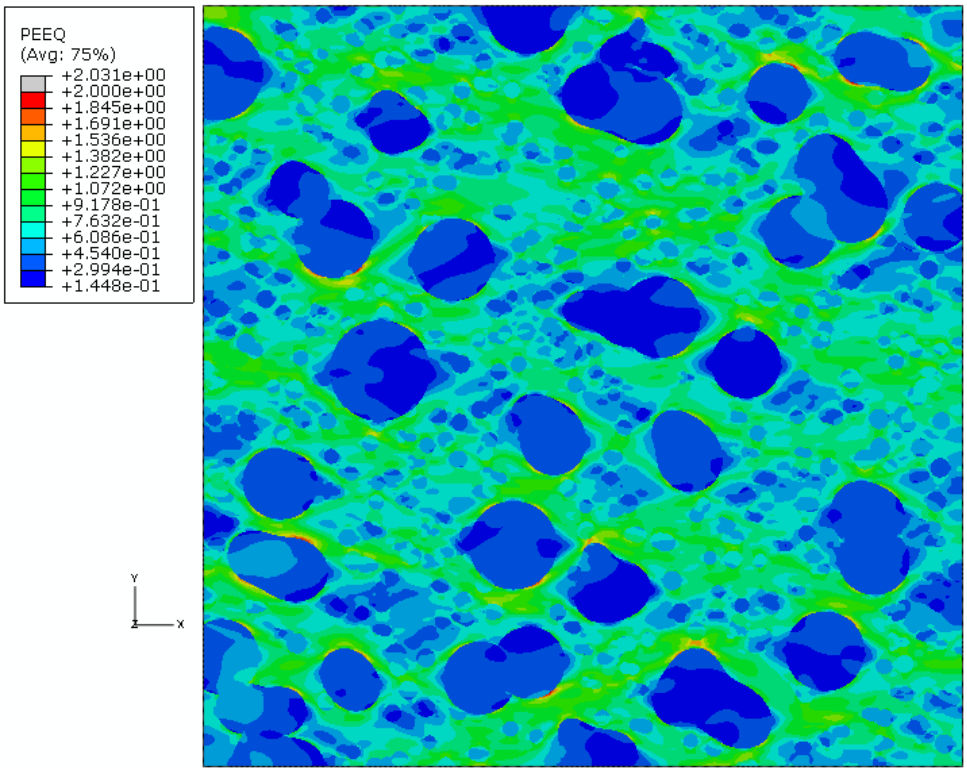

Figure 30 Subgroup A at 73% strain

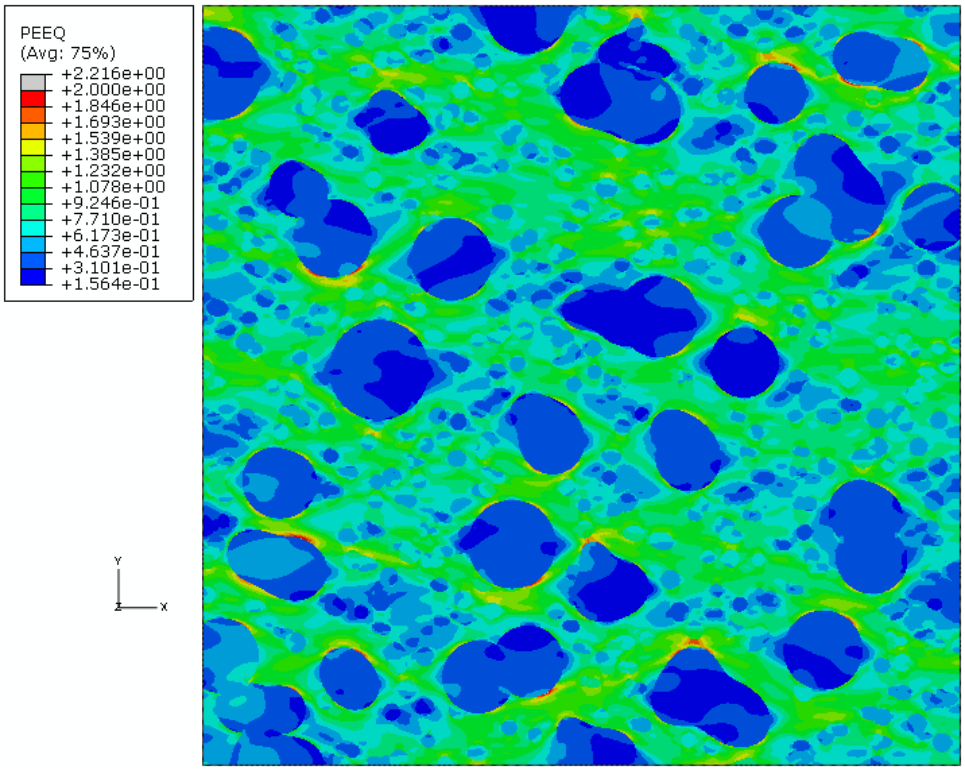

Figure 31 Subgroup A at 80% strain

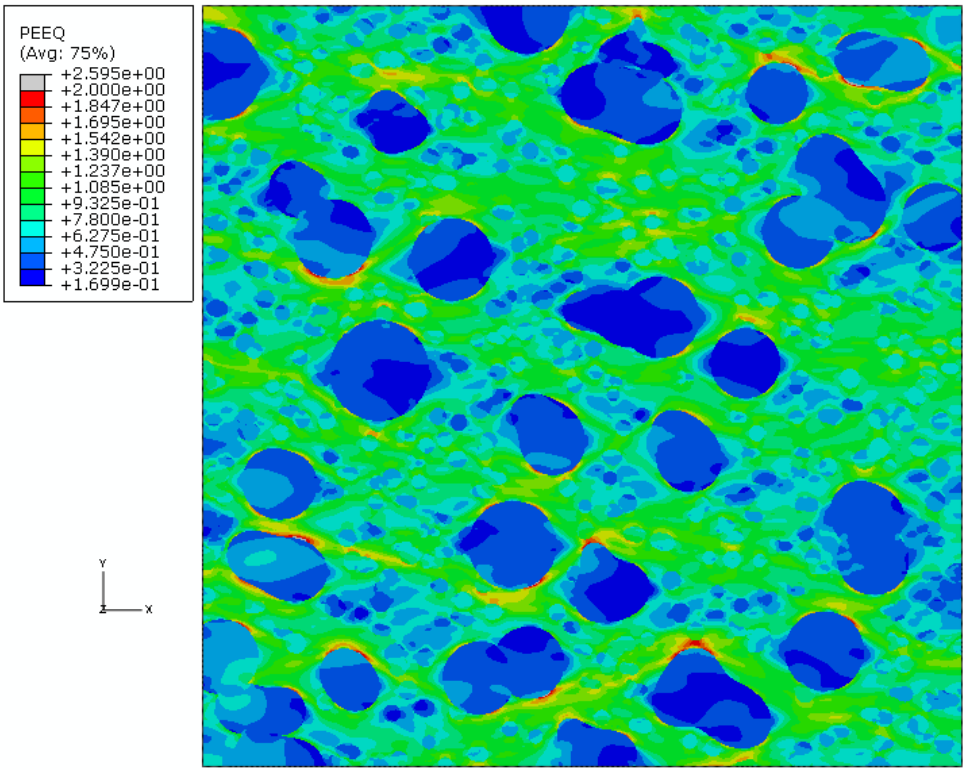

Figure 32 Subgroup A at 90% strain

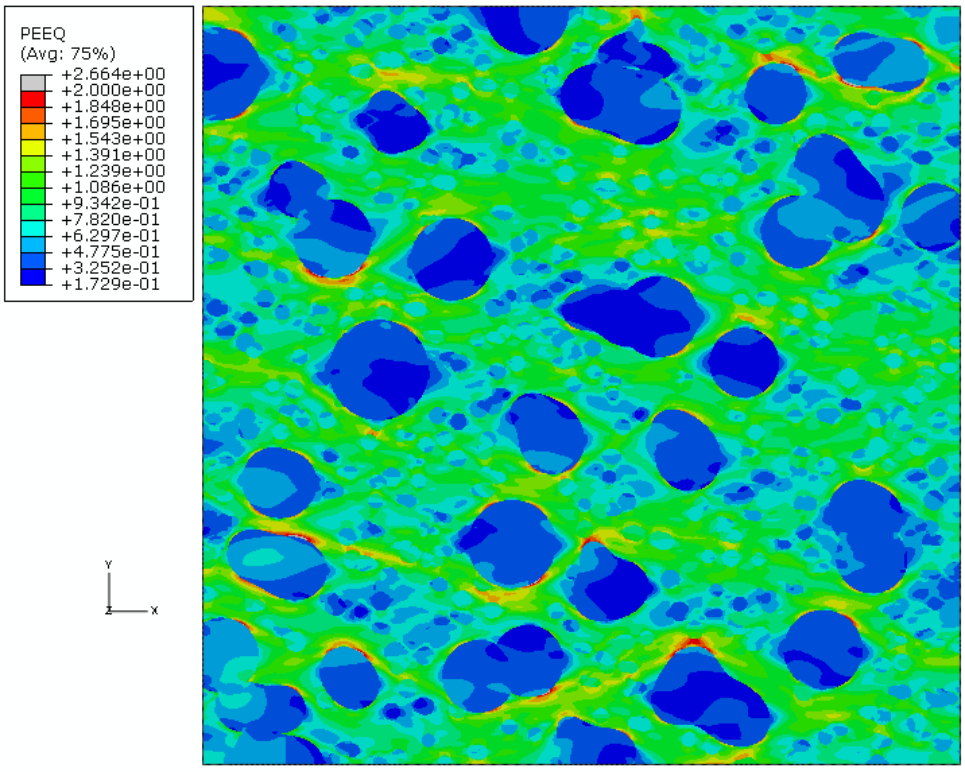

Figure 33 Subgroup A at 92% strain

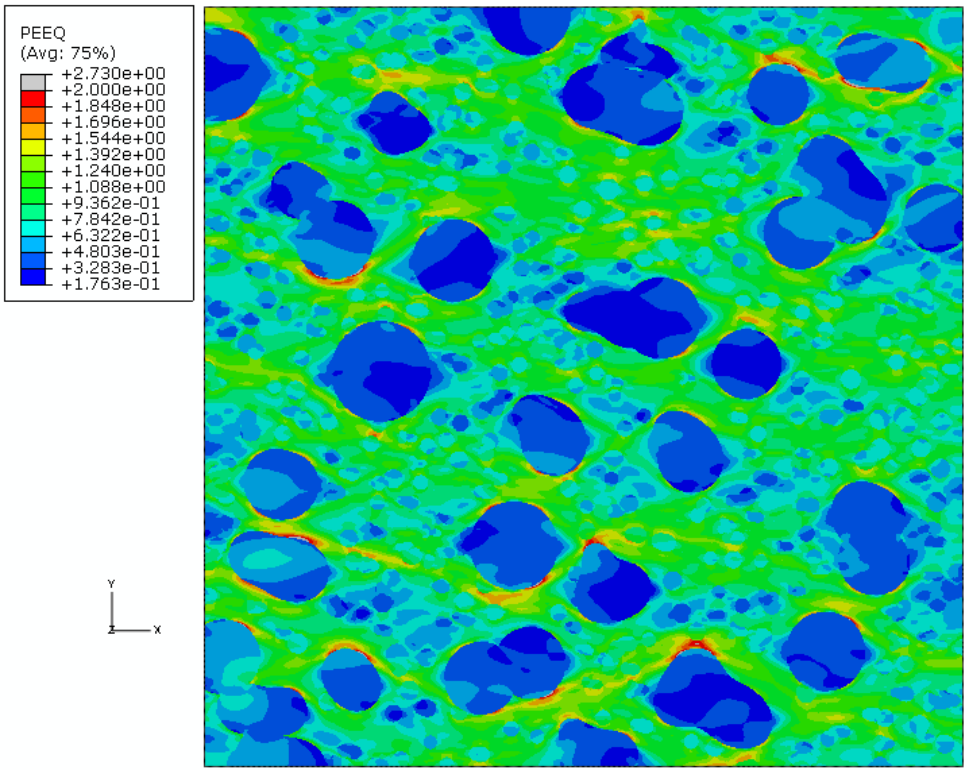

Figure 34 Subgroup A at 94% strain

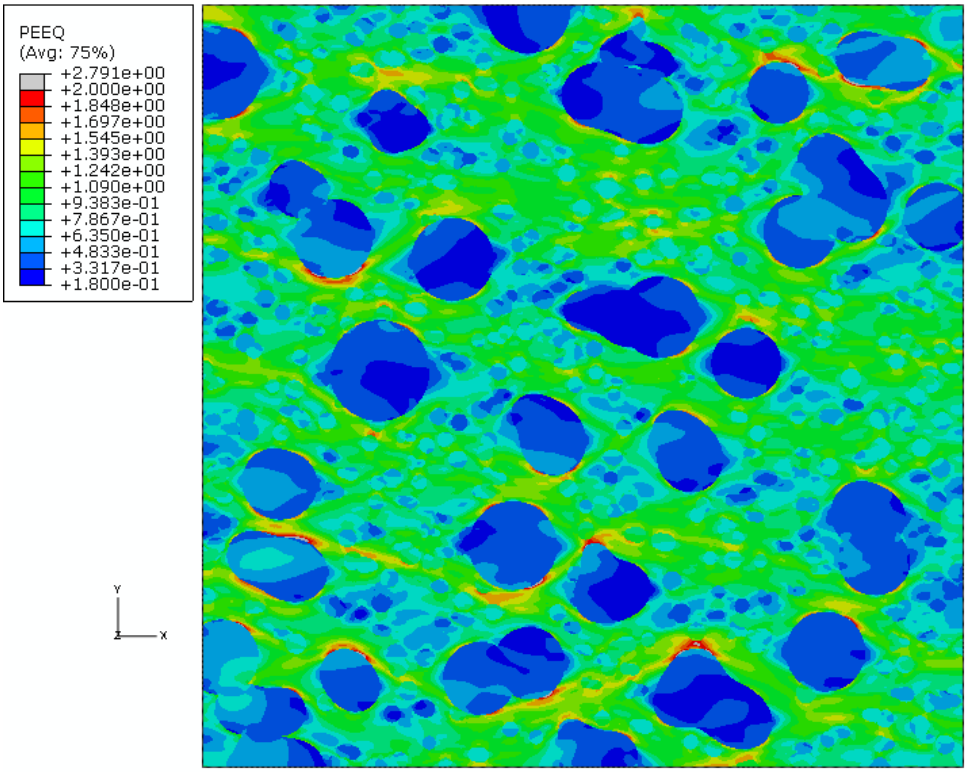

Figure 35 Subgroup A at 96% strain

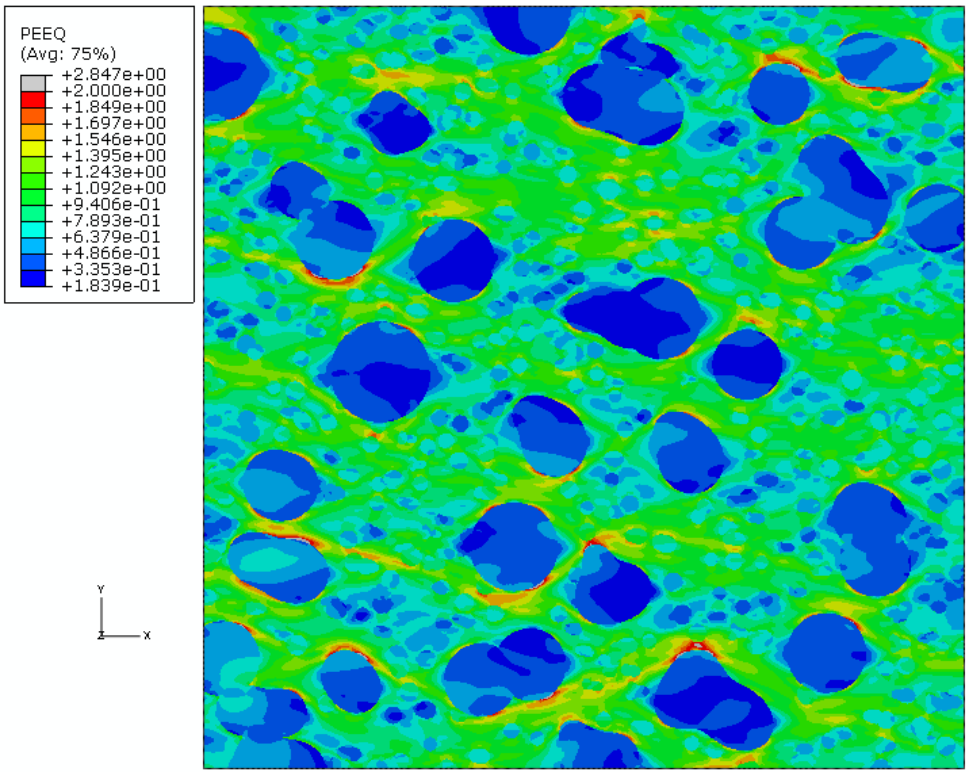

Figure 36 Subgroup A at 98% strain

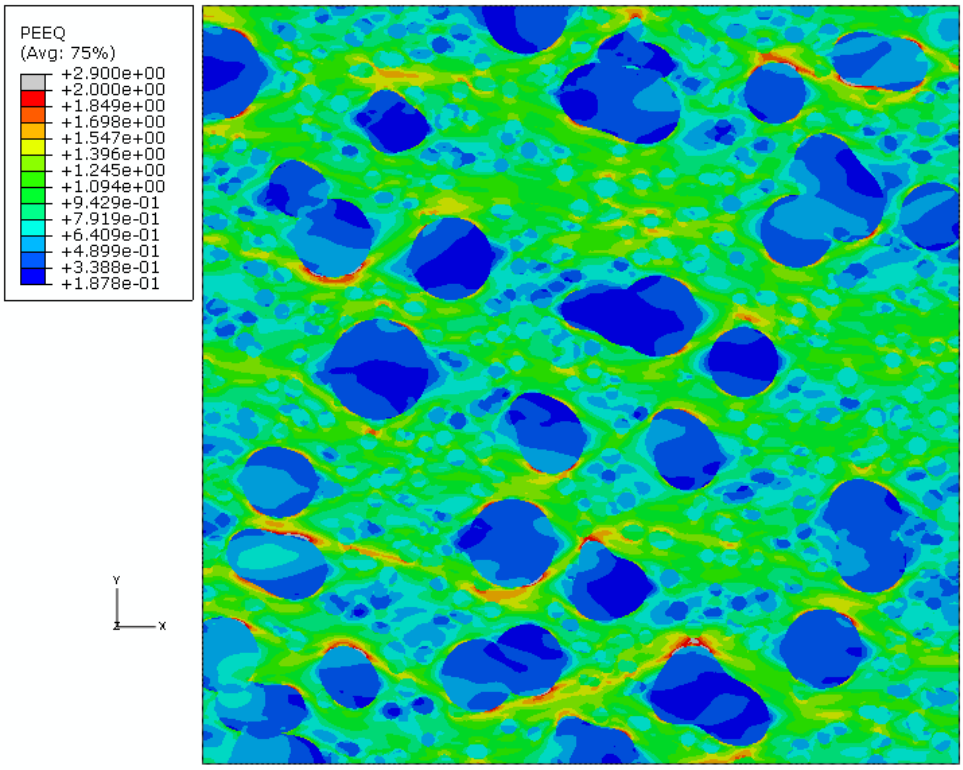

Figure 37 Subgroup A at 100% strain

As illustrated in the PEEQ figures of the austenitic microstructure in A, most of the strain localization begins around the harder bainite phases and slowly begin connecting to neighboring areas of localized strain around other neighboring bainite constituents. The maximum value of equivalent plastic strain that occurs in the microstructure at 100% strain is 2.90. The PEEQ is illustrated through the undeformed microstructure in order for the localization to be more prevalent and not distorted. For the purpose of clarification, Figure 37 illustrates the PEEQ of the microstructure at 100% strain. Figure 38 illustrates the same PEEQ as Figure 37, except in the deformed shape.

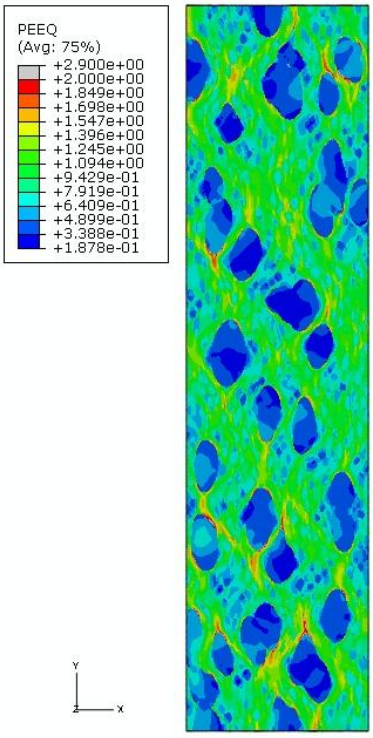

Figure 38 Subgroup A at 100% strain- deformed image

By comparing Figure 37 and 38, one is able to see the strain localization areas better in the undeformed shape. Due to this, the PEEQ will be recorded for all microstructures in the undeformed shape as done for subgroup A, but the final deformed shape will be shown for clarification. Also, through the deformed shape, one is able to visualize the strain bands during deformation. For example, as shown in Figure 38, the strain bands are stretching or branching out in the direction of loading as opposed to in the transverse direction in which one expects fracture to occur. Although the undeformed shape shows the PEEQ more clearly, the undeformed shape illustrates a more realistic proliferation of the strain bands throughout the microstructure during strain deformation.

Subgroup A was illustrated in detail in order to demonstrate the process of these simulations. The remaining subgroups will only illustrate significant chosen frames to identify the PEEQ behavior. To compare, subgroup At, or the transformed martensitic structure had the following PEEQ response in Figures 39 - 45 to the uniaxial loading test:

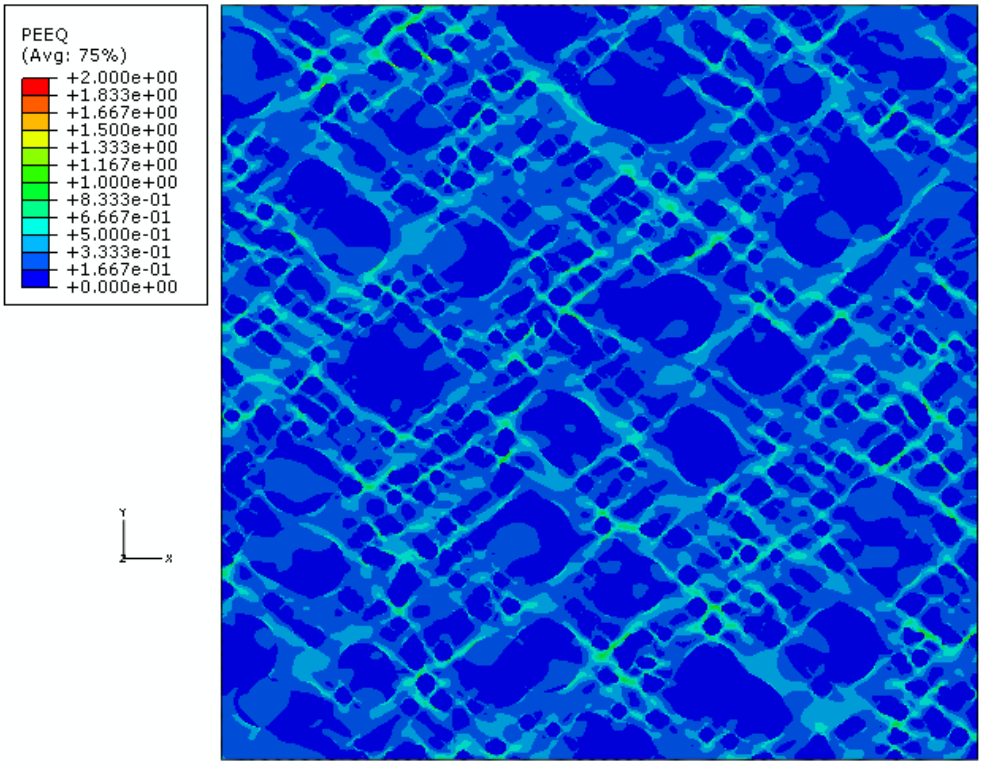

Figure 39 Subgroup At at 20% strain

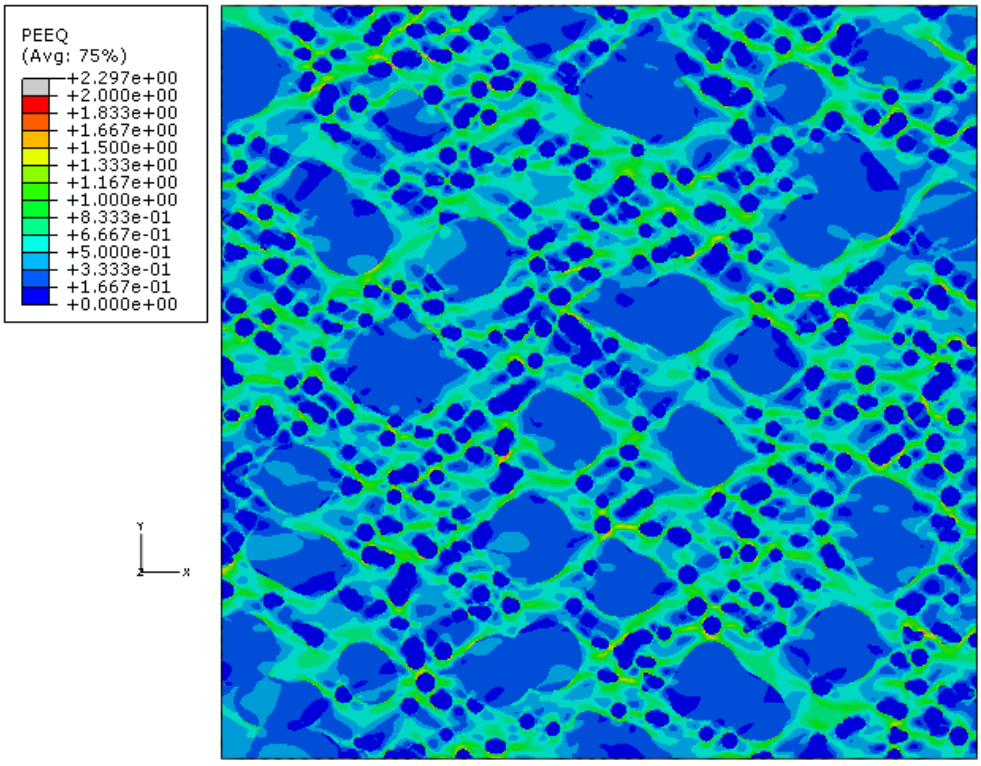

Figure 40 Subgroup At at 40% strain

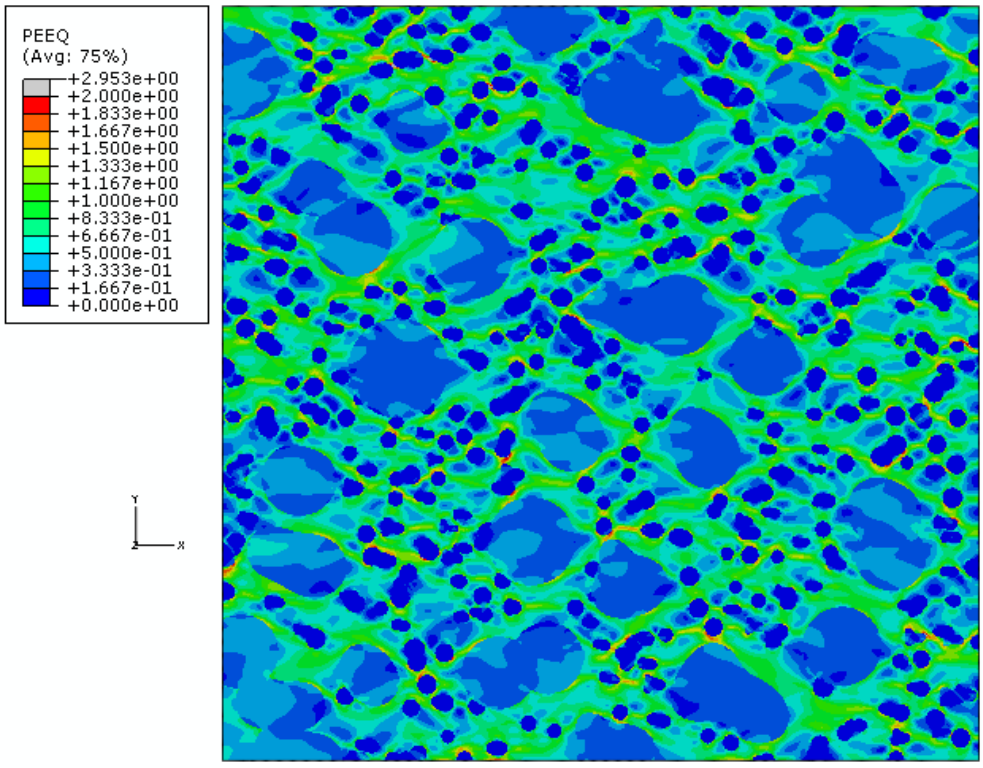

Figure 41 Subgroup At at 52% strain- ultimate tensile strength

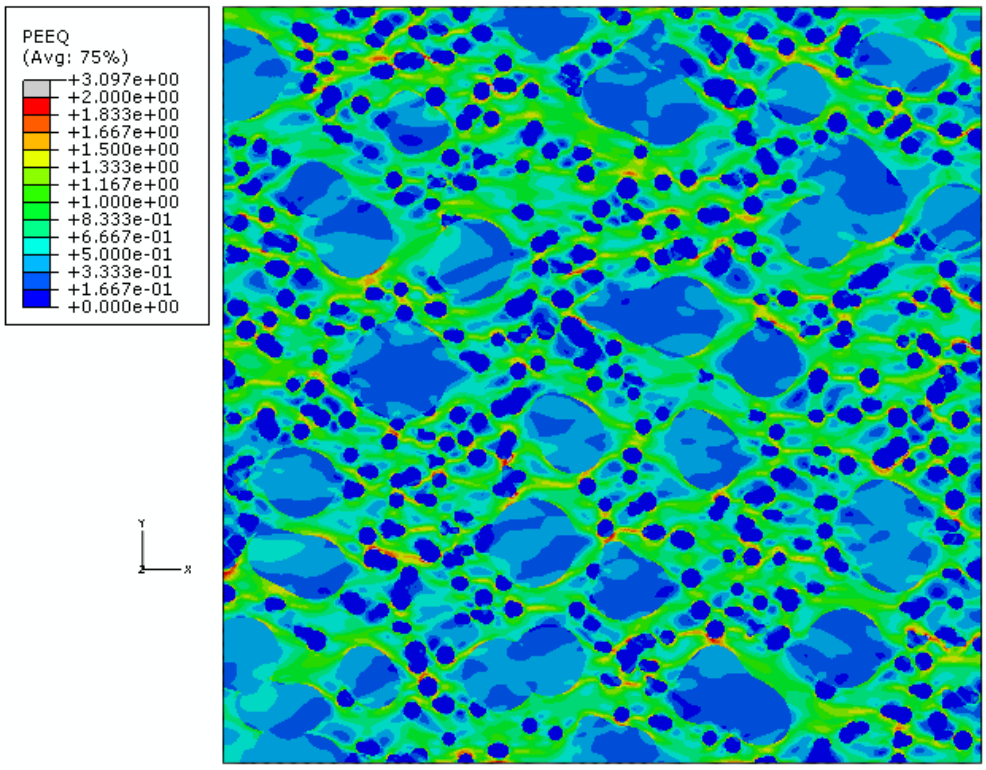

Figure 42 Subgroup At at 60% strain

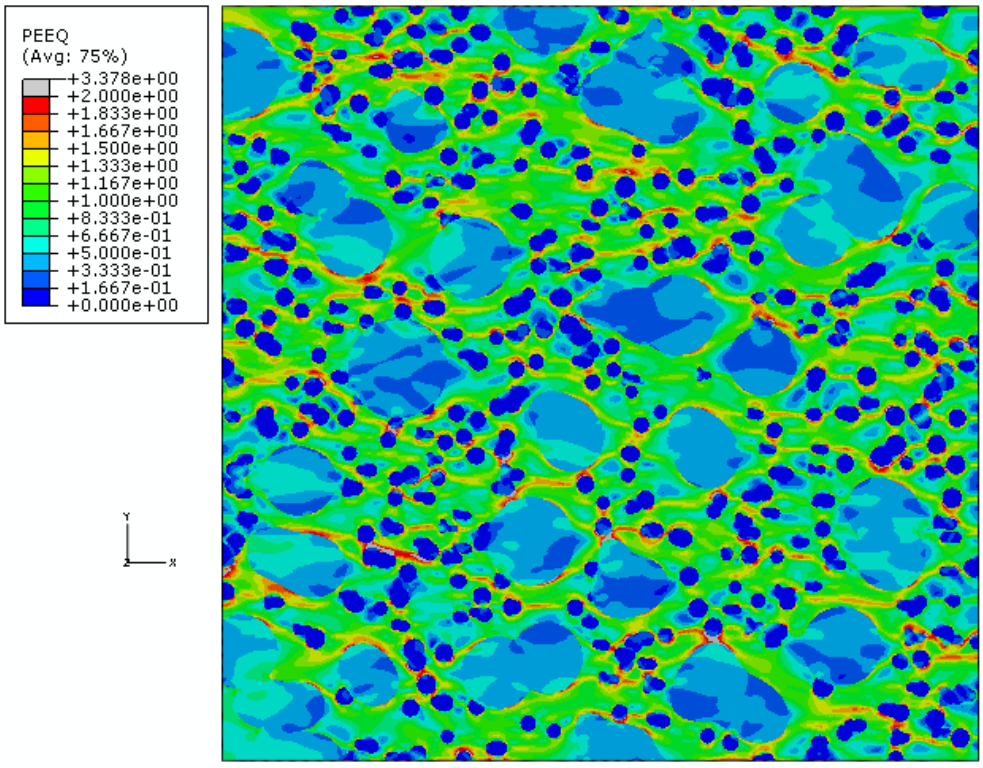

Figure 43 Subgroup At at 80% strain

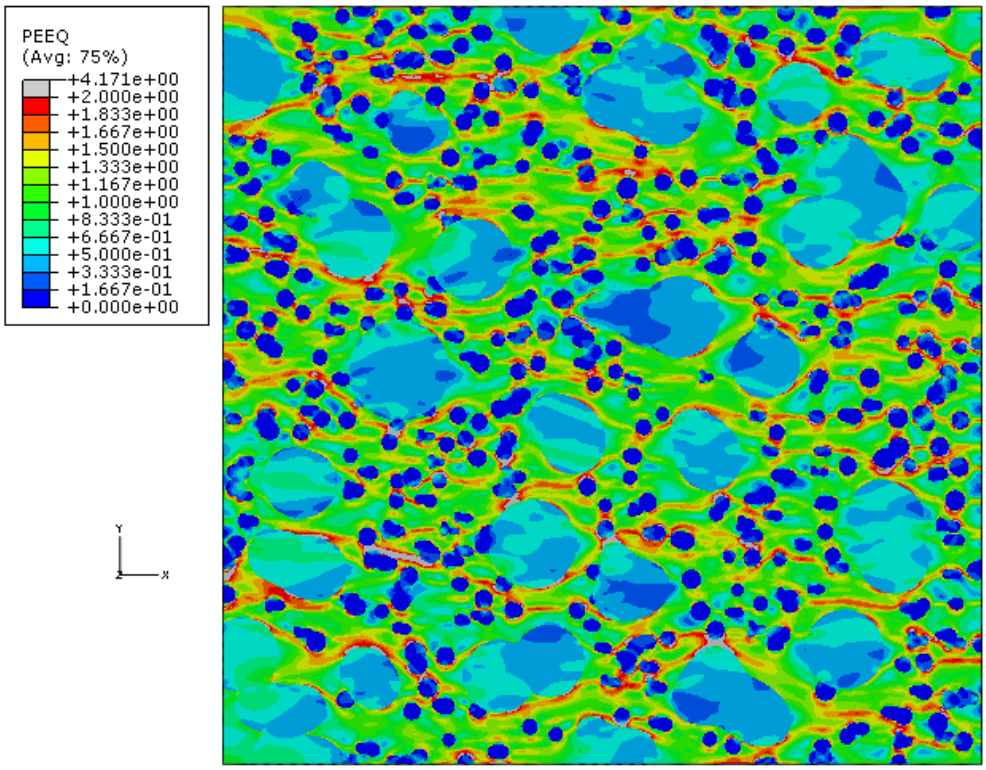

Figure 44 Subgroup At at 100% strain

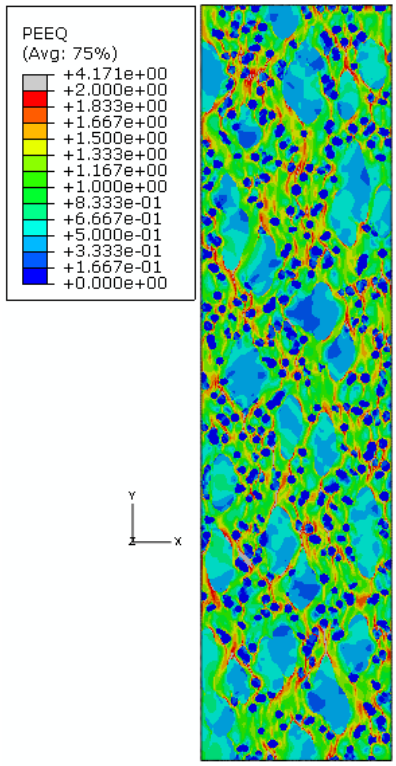

Figure 45 Subgroup At at 100% strain- deformed microstructure

By comparing subgroup A and subgroup At at 100% strain, much higher strain values and concentrations occur in the martensitic structure due to the presence of the harder phase. Subgroup A illustrates a maximum strain value of 2.9 while subgroup At shows a much larger value of 4.171. The significant difference in properties between the hard martensite and the soft ferrite matrix introduce an opportunity for large strain localization and consequently a potential area vulnerable to a crack engendering and propagating to similar neighboring areas. This difference in properties is not as prevalent in subgroup A compared to its transformed phase. Also, in microstructure At, the PEEQ

engenders higher concentrations around the martensite constituents verses microstructure A which begin to form around the bainite islands. This is also explained by the fact that these concentrations seem to begin to form around the hardest phase presented in the microstructure. Also, there seems to be many more areas of potential void coalescence or cracking in the martensitic microstructure. This cracking only occurs and spreads through the ferrite matrix. This suggests that ductile fracture will occur at failure for the microstructures in Group 1 verses cleavage fracture in which strain concentrations would also be illustrated inside the martensite and bainite phases. Yet, void initiation and coalescence cracks are suggested to occur more in At while microstructure A emphasizes the possibility of failure due to strain localization in the ferrite matrix. Also, these strain bands seem to spread in the direction of loading as opposed to the transverse direction in which fracture is predicted to occur.

In the history output, ABAQUS revealed the force reactions and displacements in the direction of loading on the nodes corresponding to the top surface of the RVE after the analysis was completed. From the final force, the stress was easily calculated by dividing the summed forces from the nodes on the top edge of the RVE by the cross sectional area of the top edge, which in this case is simply $50\,\mu m^2$. The percentage of strain was computed through dividing the average displacement of all the nodes corresponding to the top edge by the original length, $50\,\mu m$ and multiplying by 100 to obtain a strain percentage. Thus, it was possible to reveal the stress vs. strain behavior of each microstructure under uniaxial tensile loading as shown in Figure 46.

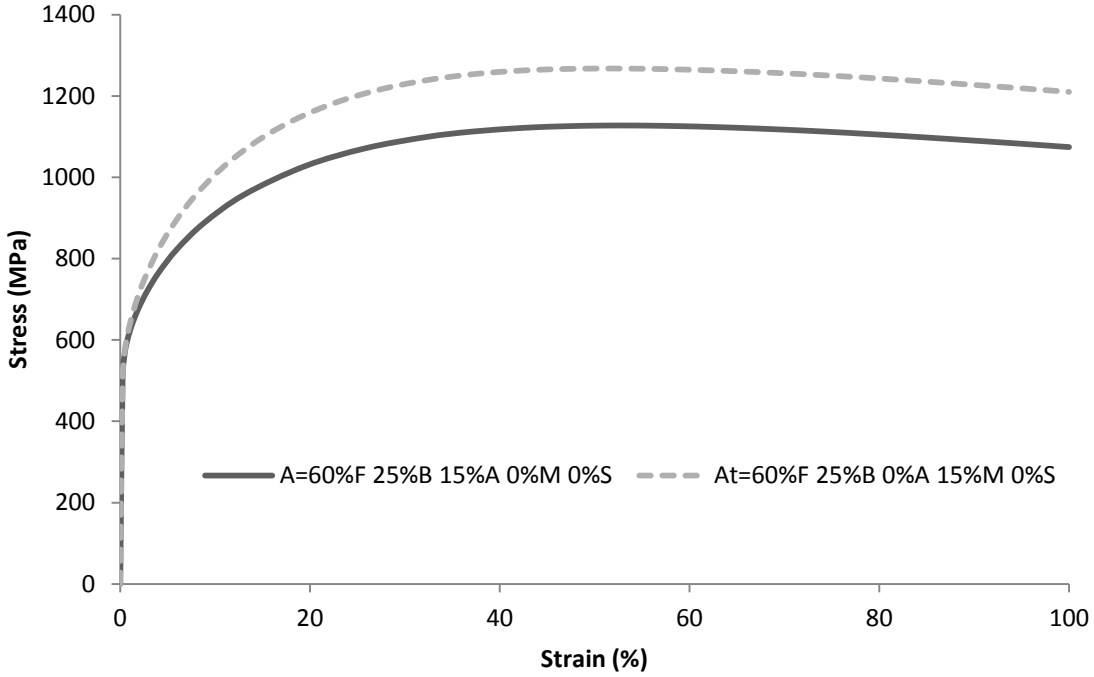

Figure 46 Stress vs. strain response for Group 1

From the tabulated values from Figure 46, the modulus of elasticity, initial yield strength, ultimate tensile strength, and percent strain at the ultimate tensile strength for each composite was calculated as well and can be shown in Table 10.

Table 10 Resulting properties for Group I TRIP steel microstructures

Subgroup	E (MPa)	σ_y (MPa)	σ_u (MPa)	$\%\varepsilon_u$ (μm/μm)
A	203546.4	407.0928	1127.374	53.3658
At	203547.2	407.0944	1268.156	51.7284

As expected, microstructure At, in which the austenite has completely transformed into martensite, illustrates a higher ultimate tensile strength due to the presence of martensite. The complete phase transformation resulted in a 12.49% increase in strength. The modulus of elasticity and initial yield strength of the composite are slightly higher in Subgroup At than Subgroup A. Also, the martensitic structure proves to be 1.637% less ductile than subgroup A, or the initial austenitic structure. Therefore, Group 1 ultimately illustrates that the strength after transformation in TRIP steel is much higher than that of the initial austenitic structure, yet ductility is slightly compromised.

4.2 PEEQ Responses For Groups 2-5: TRIP Steel With Ceramic Inclusions

Groups 2-5 consist of three main subgroups, each with an initial austenitic microstructure and the transformed martensitic microstructure clearly identified in the previous chapter. The first, i ,has 1% volume of ceramic inclusions, the second, ii, has 5% ceramic inclusions, and the third, iii, has 10% ceramic inclusions. The only variant between each main group is the ceramic material for the inclusions. The PEEQ responses for each ceramic material were recorded at specific strain levels- 40% strain, the strain at which the ultimate tensile strength occurs, 80% strain, and 100% strain. Each group will be compared at each strain level with its corresponding subgroup in order to visualize the effects caused by the different materials. Also, each subgroup will be compared with the other austenitic or martensitic structures along with its control structure in Group 1 to visualize the effects of varying ceramic volume fractions in the microstructures. First, we will focus on the austenitic structures at 40% strain. The control in Group 1 is illustrated first followed by the microstructures in Subgroups Ai, Aii, and Aiii from Groups 2-5 as shown in Figures 47 - 49.

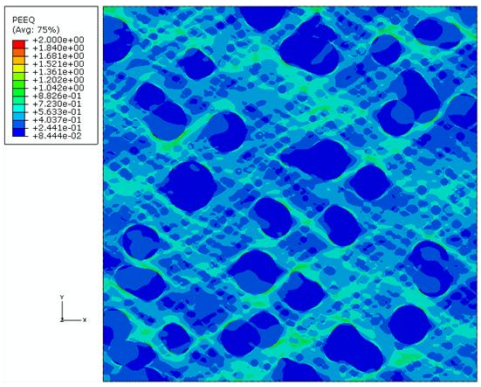

Group 1: A

Subgroup Ai

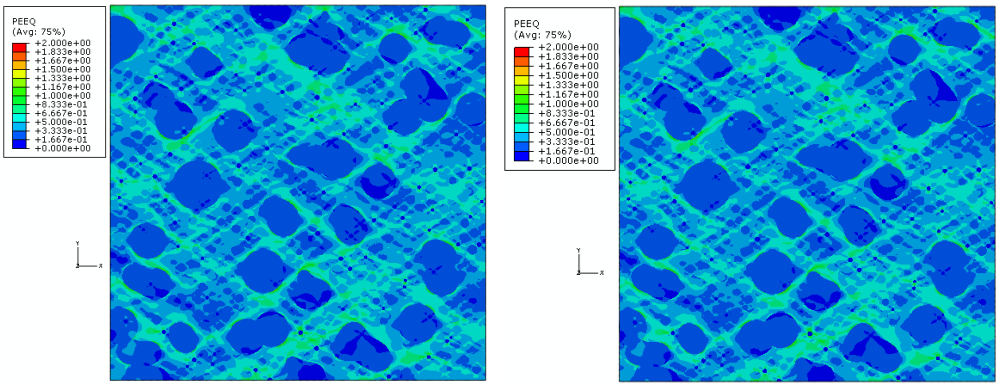

Group 2: Silicon Carbide **Group 3: Cementite**

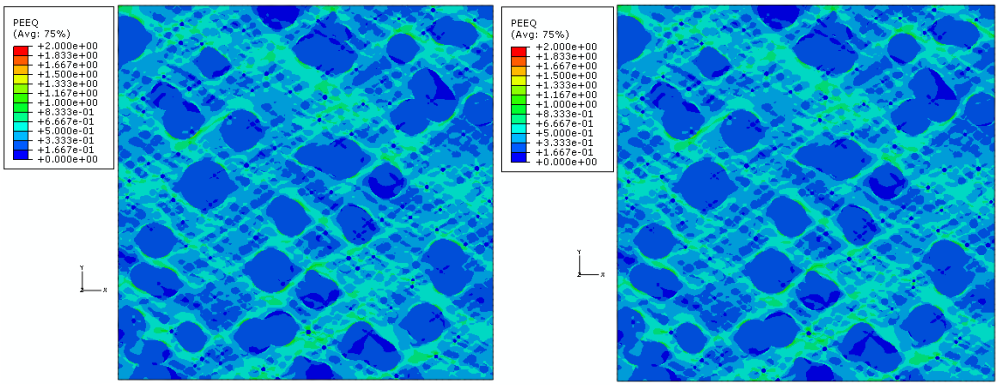

Group 4: Zirconia **Group 5: Aluminum**

Figure 47 PEEQ of Subgroup Ai compared to Group 1 at 40% strain

Subgroup Aii

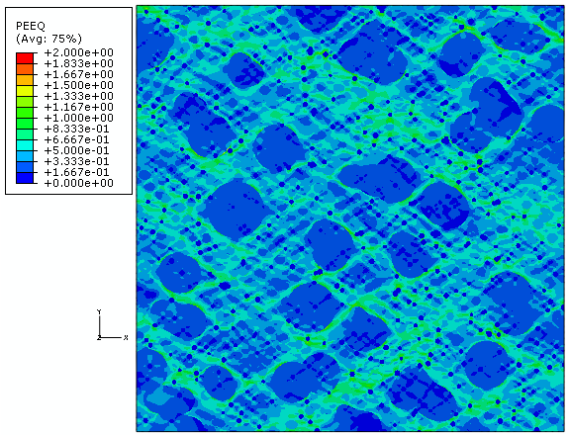

Group 2: Silicon Carbide

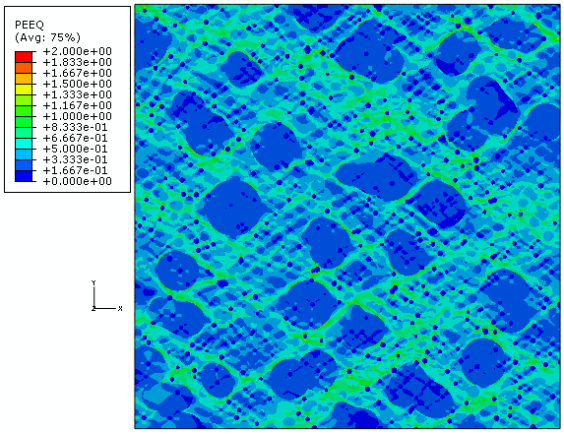

Group 3: Cementite

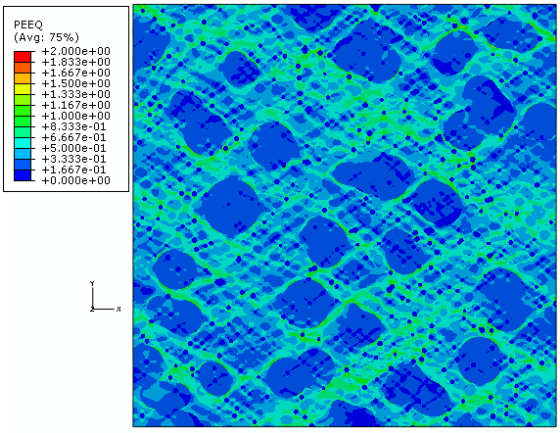

Group 4: Zirconia

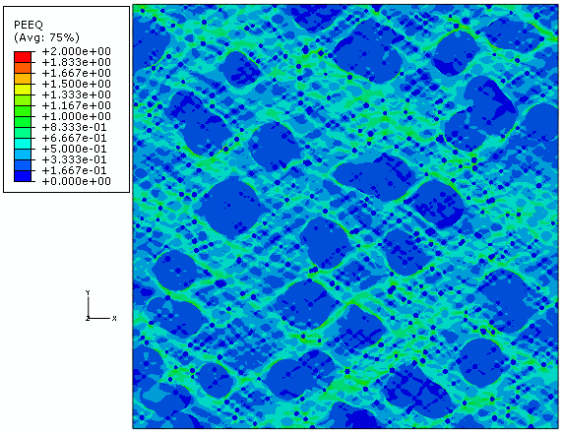

Group 5: Aluminum Oxide

Figure 48 PEEQ Subgroup Aii at 40% strain

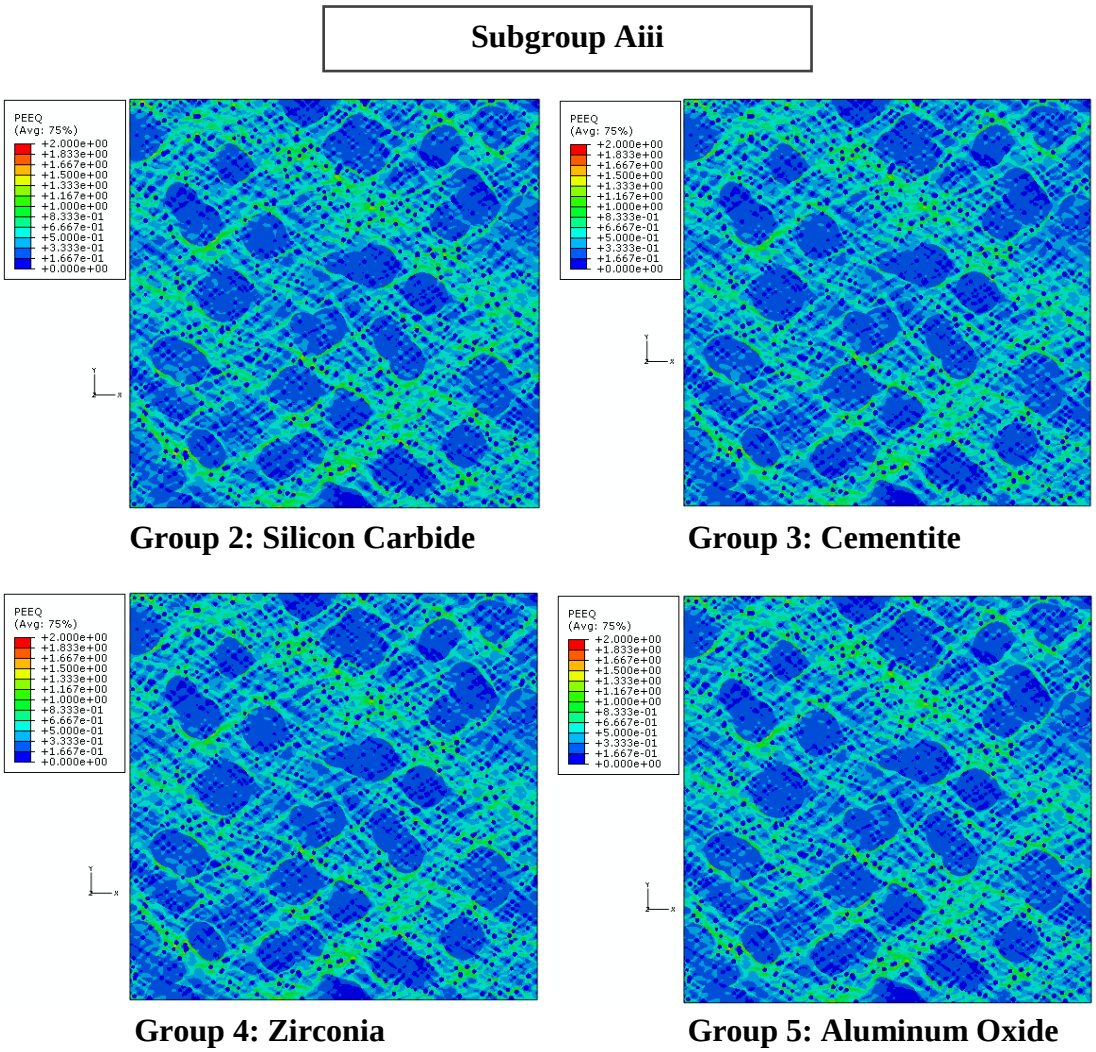

Figure 49 PEEQ of Subgroup Aiii at 40% strain

At 40% strain, the value of equivalent plastic strain throughout the microstructure increase with the increasing volume fraction of ceramic inclusions. Subgroup Ai illustrate higher values of PEEQ throughout the ferrite, bainite and retained austenite compared to the control, or Group 1. The ferrite now ranges from 0.333 to 1.0 while

both the austenite and bainite illustrate values ranging from 0.1667 to 0.3. These values increase in Subgroup Aii to the ferrite still ranging from 0.333 to 1.0 but illustrating more regions around the higher valued area of this scale, and the austenite and bainite now ranging from 0.1667 to 0.5. In Subgroup Aiii, these values increase to ferrite ranging from 0.1667 to 1.333 with concentrations of 1.333 to 1.7 of PEEQ surrounding the ceramics. The bainite and austenite constituents still illustrate a range of 0.1667 to 0.5, except illustrate more regions closer to the higher part of the scale, especially around the ceramic inclusions. As the volume of ceramic inclusions increase, the PEEQ bands become thinner, higher valued, and more prevalent throughout the ferrite matrix in the microstructures. In Subgroup Aiii, we also begin to see strain localization engendering around some ceramic inclusions in the lower left area of Groups 2-5. No plastic strain occurs in the ceramic inclusions in any of the austenitic microstructures at 40% strain. Within each subgroup, the RVE's presenting Groups 2-5 are visually the same. This indicated that at 40% strain, the PEEQ material behavior seems independent of the properties presented in the ceramic inclusions. Therefore, at this point in the investigation, the material response is independent of the ceramic material utilized for the inclusions. The next frames that will be observed in Figures 50 - 52 are the responses for each of the above microstructures at their corresponding strain at which they experience ultimate tensile stress.

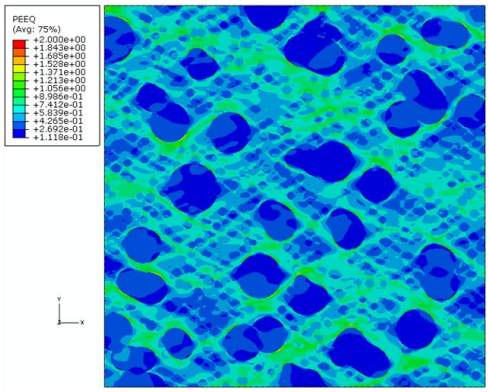

Group 1: A - 53% Strain

Subgroup Ai

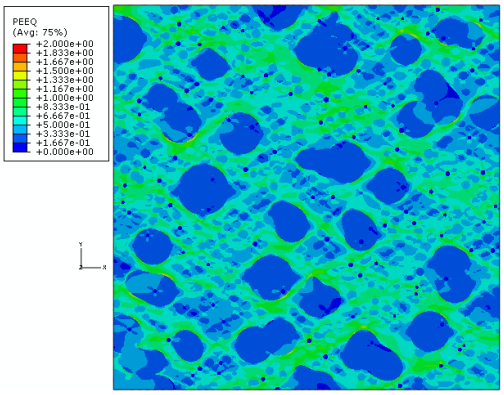

Group 2: Silicon Carbide-

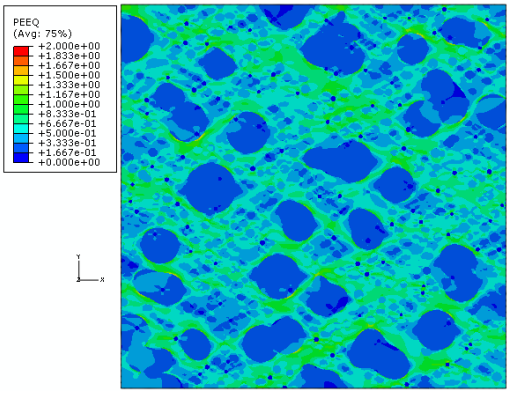

Group 3: Cementite-

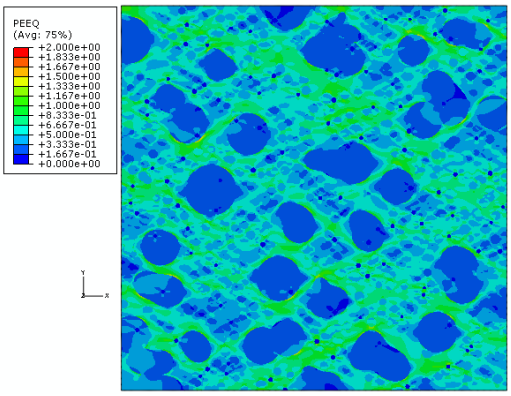

Group 4: Zirconia-52.8%

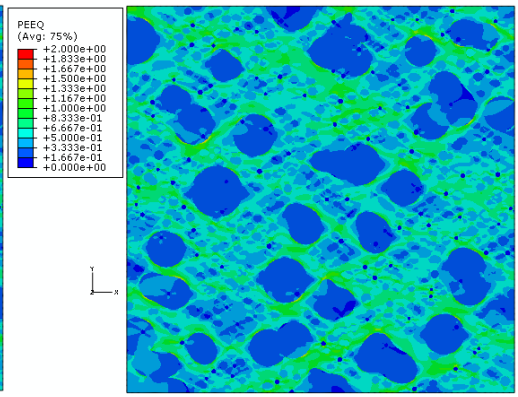

Group 5: Aluminum Oxide-52.8%

Figure 50 PEEQ for Group 1 and Subgroup Ai - ultimate tensile strength

Subgroup Aii

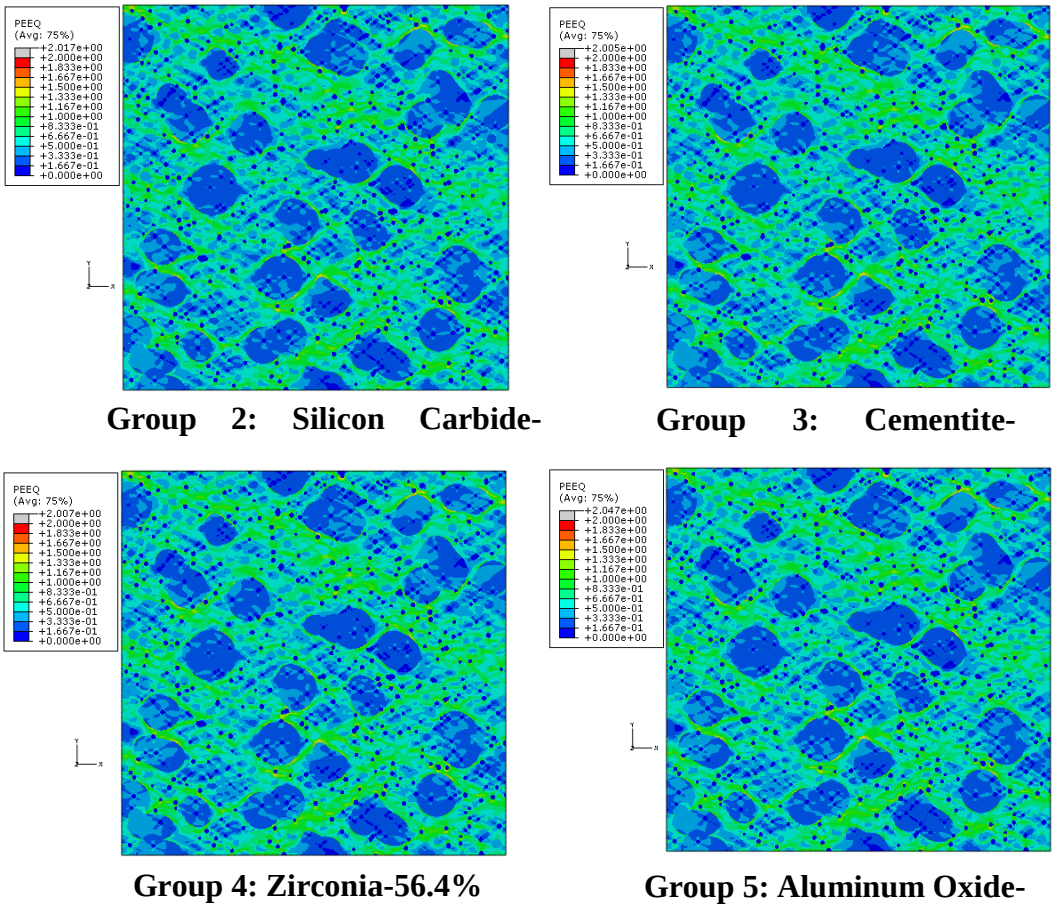

Group 2: Silicon Carbide- **Group 3: Cementite-**

Group 4: Zirconia-56.4% **Group 5: Aluminum Oxide-**

Figure 51 PEEQ for Subgroup Aii - ultimate tensile strength

Subgroup Aiii

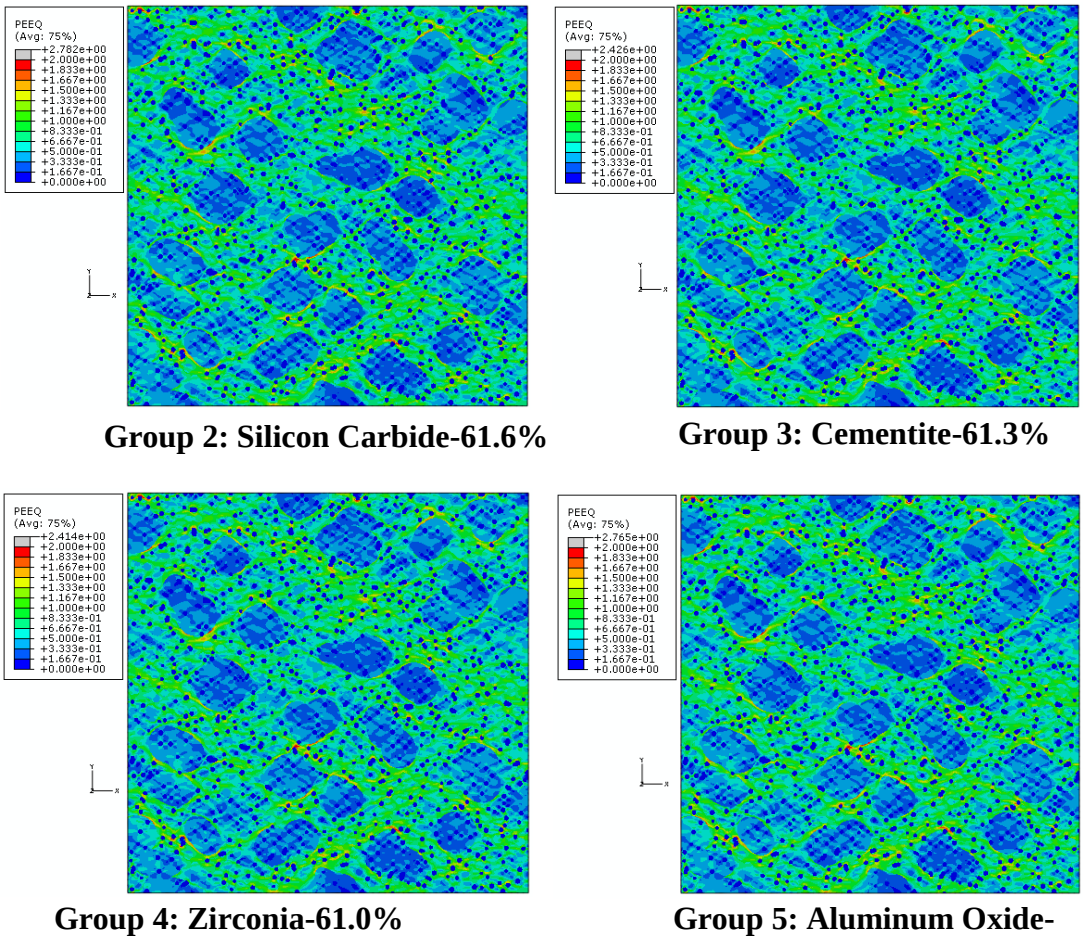

Group 2: Silicon Carbide-61.6% **Group 3: Cementite-61.3%**

Group 4: Zirconia-61.0% **Group 5: Aluminum Oxide-**

Figure 52 PEEQ for Subgroup Aiii - ultimate tensile strength

As seen earlier, in Group 1, or the control with no ceramic inclusions, very few small areas of strain concentrations ranging from 1.528 to 1.685 can be seen engendering at 53% strain around a few bainite islands. We concluded that this occurred due to bainite embodying the hardest constituent in the microstructure, thus introducing an interface serving as an area vulnerable to strain localization. This idea is also presented through

the ceramic reinforced microstructures. As before, more areas of higher valued strain can be seen as more ceramic inclusions are introduced into the microstructure. For Subgroup Ai, the ultimate tensile strength for Groups 2-5 occur at nearly the same strain as Group 1, exactly 52.8% strain for Groups 2-5. Despite this similarity, the RVE's illustrate more and thinner green strain bands than blue in Subgroup Ai, indicating more areas of higher valued PEEQ. The ferrite PEEQ ranges from 0.5 to 1.333 with small areas of high values of strain concentrations occurring on the interface of the bainite islands. No visual high strain concentrations seem to occur at the ceramic interfaces. This may be due in part to the fact that since there is only a 1% volume increase in ceramics, the presence of the bainite may still control the overall behavior of the microstructure at this point in time. The bainite shows PEEQ ranging from 0.1667 to 0.5, but closer to the larger side of the color scale. Also, the PEEQ of the retained austenite now ranges from 0.3 to 0.5, while the ceramic inclusions exhibit no plastic strain.

Subgroup Aii, illustrates even higher values of PEEQ throughout the microstructure, most notably, the ferrite matrix and interfaces around some bainite islands and ceramic inclusions. The PEEQ bands are also thinner and more prevalent through the microstructure than those in Subgroup Ai. The ferrite matrix illustrates PEEQ ranging from 0.333 to 1.333 with small areas of high PEEQ concentrations ranging from 1.333 to 1.833 occurring on the interfaces of some bainite islands and neighboring ceramic inclusions. The bainite and retained austenite constituents illustrate PEEQ values ranging from 0.1667 to 0.5, where the austenite shows much lighter areas indicating a higher PEEQ than that occurring in the bainite. A very slight difference in

maximum PEEQ values can be seen between the different ceramic material groups in Subgroup Aii, yet this most likely due to the different strain frame indicated. Groups 2,3,4 and 5 each respectively show a maximum PEEQ value of 2.017, 2.005, and 2.007. and 2.047. Thus, it is still safe to indicate that material properties of the ceramic inclusions are ineffective towards the overall equivalent plastic strain behavior of the reinforced TRIP steel composite at ultimate strength. Compared to Group 1 and Subgroup Ai, the microstructures in Subgroup Aii illustrate the ultimate tensile strength occurring at higher strain values with Group 4-Zirconia being the most ductile with a strain value of 56.4%. This group is then followed in descending order by Group 3-Cementite, Group 5- Aluminum Oxide, and Group 2- Silicon Carbide, each with a corresponding strain of 55.9%, 55.5%, and 54.5%. Even at this stage, the ceramic inclusions also show no sign of PEEQ.

Subgroup Aiii, with 10% volume fraction of ceramic inclusions present illustrate the highest strain values at which ultimate strength occurs among the austenitic microstructures. Now, the most ductile microstructure embodies that presented by Group 5-Aluminum Oxide with ultimate tensile stress occurring at 62.7%. The next highest ductile microstructure is Group 2-Silicon Carbide with ultimate at 61.6% strain followed by Group 3-Cementite and finally Group 4- Zirconia with strain values of 61.3% and 61.0% respectively. Also, the maximum PEEQ values presented in the microstructures in Subgroup Aiii are higher than those in the previous microstructures. Again, though, this might be due to the higher strain value frames that are observed at the time of the ultimate tensile strength. None the less, these values have increased in Group 2,3,4 and 5

to 2.782, 2.426, 2.414, and 2.765 respectively. The ferrite matrix contains PEEQ values ranging from 0.667 to 1.333 with concentrations of 1.333 to 2.0 occurring more prevalent around most bainite and some ceramic particles. In these particle reinforced TRIP steel microstructures, these concentration areas are also beginning to branch together and connect to neighboring areas of high concentrations. The bainite and austenite constituents are also illustrating higher areas of PEEQ than the previous microstructures, now ranging from 0.1667 to 0.667 and 0.3 to 1.167, respectively. The ceramic particles still exhibit no PEEQ. Also, again, the PEEQ response of the material still seems to be independent of the ceramic material presented since the microstructures illustrate very similar behavior. This can be seen while comparing Groups 2-5 within each Subgroup. The PEEQ responses and concentrations prove to be identical regardless of ceramic material properties. Yet, with this in mind, the ceramic properties do indeed produce a difference in ductility. At this point, it is also observed that for the austenitic structure, ductility increases proportionally to the increasing volume fraction of ceramic particles.

The next time frame that these microstructures are evaluated is at 80% strain, indicated by Figures 53 -55.

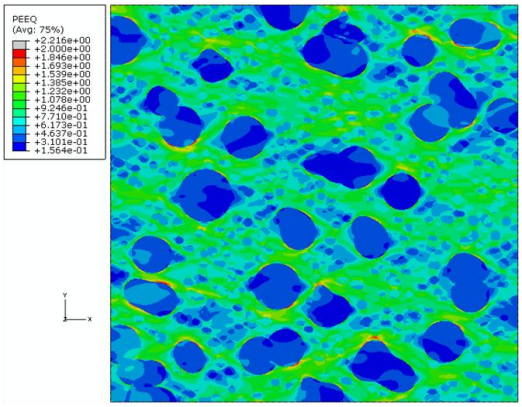

Group 1: A

Subgroup Ai

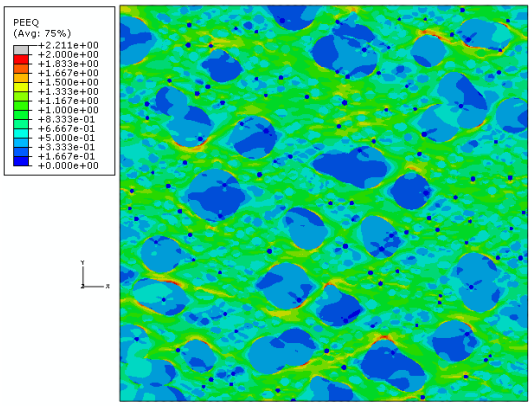

Group 2: Silicon Carbide

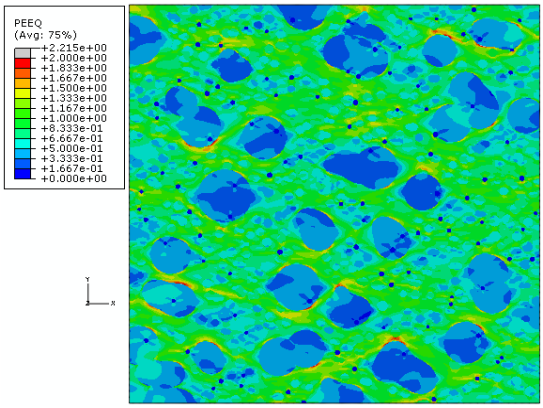

Group 3: Cementite

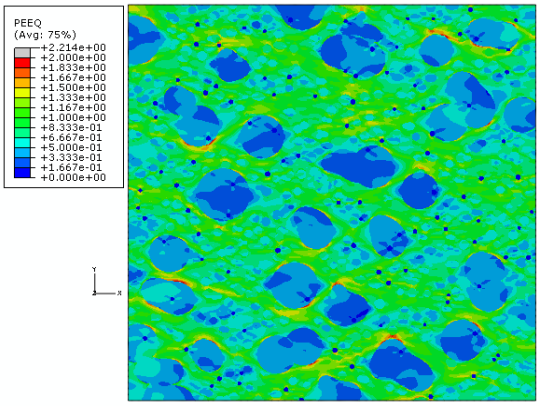

Group 4: Zirconia

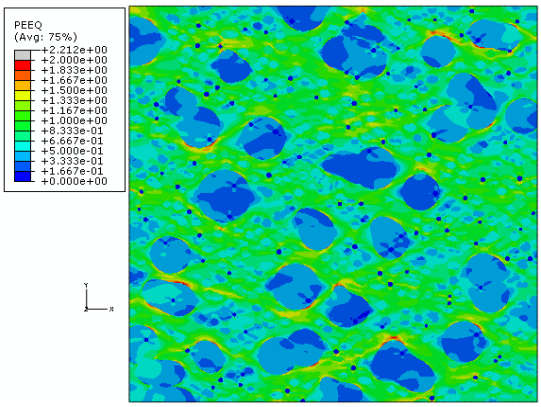

Group 5: Aluminum Oxide

Figure 53 PEEQ for Group 1 and Subgroup Ai at 80% strain

Subgroup Aii

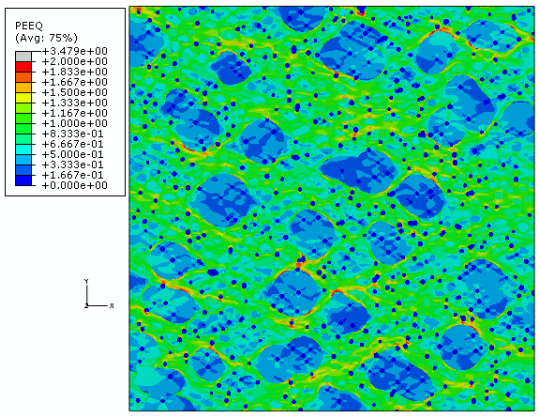

Group 2: Silicon Carbide

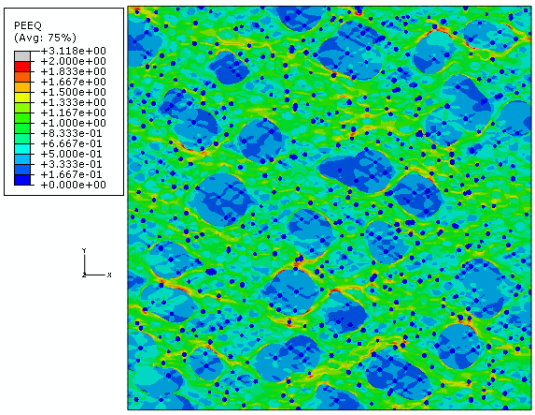

Group 3: Cementite

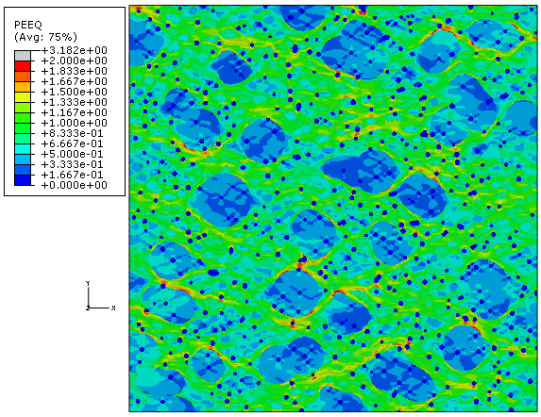

Group 4: Zirconia

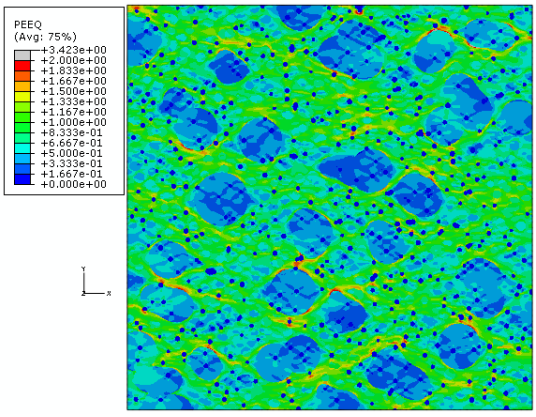

Group 5: Aluminum Oxide

Figure 54 PEEQ for Subgroup Aii at 80% strain

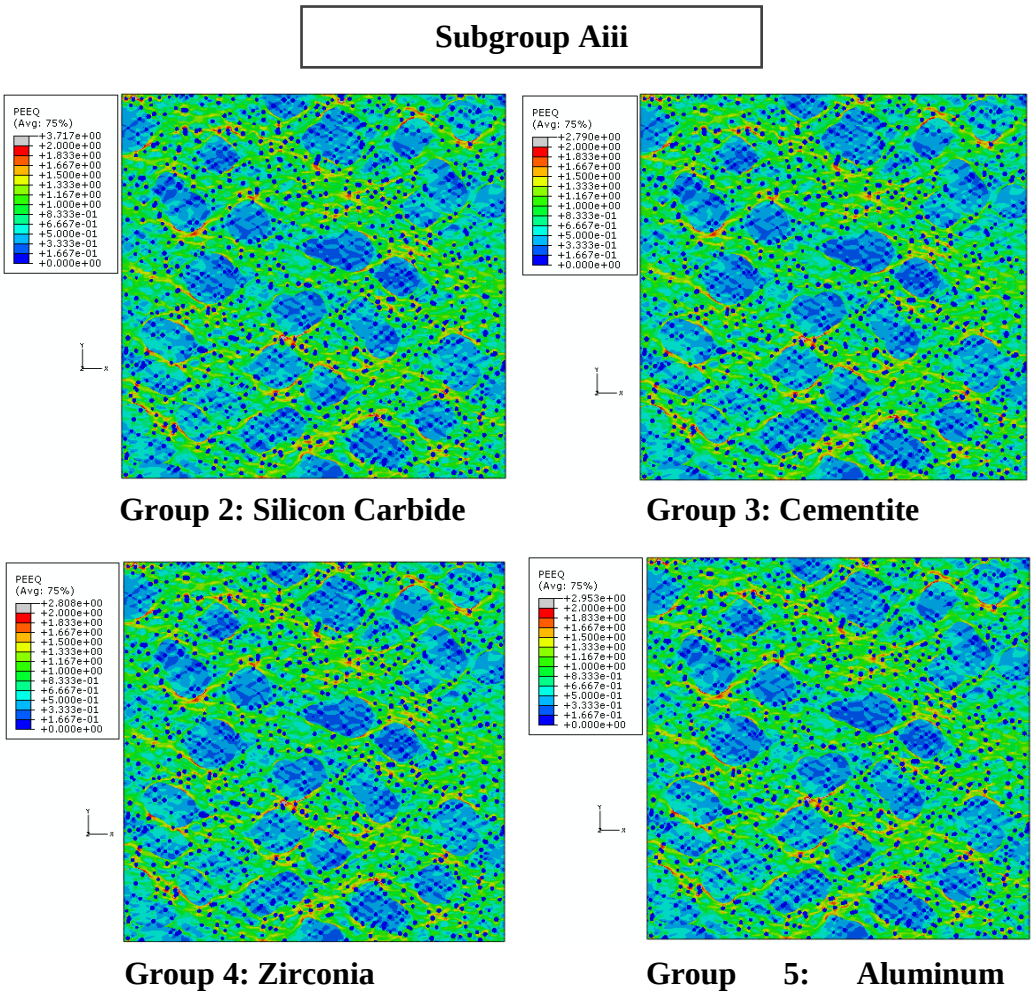

Figure 55 PEEQ for Subgroup Aiii at 80% strain

To revisit, Group 1 at 80% strain indicates more strain localization occurring around the bainite islands, or at the bainite island interfaces with values ranging from 1.539 to 2.216. the formation of branches connecting these concentrated areas can also be seen in the ferrite ranging from PEEQ values of 1.385 to 1.539. These values all occur in the ferrite matrix. The remaining portions of the ferrite matrix range from PEEQ values of 0.6173 to 1.385 in which the higher values of PEEQ occur near the bainite islands. Within the bainite, PEEQ values of 0.1564 to 0.6173 can be seen while the retained austenite illustrates PEEQ values of 0.4637 to 0.6173. The retained austenite seems to be undergoing more equivalent plastic strain than that of the bainite. Naturally, this occurs due to the fact that bainite is a harder phase with a higher modulus of elasticity as described earlier.

With this observed factor, Subgroup Ai illustrates much higher PEEQ value strains throughout the microstructure. Although microstructure A in Group 1 illustrates a maximum PEEQ value of 2.216, while the maximum PEEQ in Subgroup Ai out of Groups 2-5 is 2.215, which is almost a negligible difference, the PEEQ distribution throughout the microstructure is extremely different in Subgroup Ai. The ferrite PEEQ values now range from 0.5 to 1.5 with many more areas illustrating a lighter green color than blue, revealing more areas of higher valued PEEQ. Also, the interfaces between the ferrite and most bainite phases indicate high PEEQ concentrations that are branching out through the ferrite to other areas of high concentrations. Although these high concentrations are most notable around the bainite phases, some are observed around ceramic particles, especially those that are closer to bainite islands. These also facilitate

the branches forming from one high PEEQ localization area to another. None of these high PEEQ regions occur around the austenite interfaces. Within the bainite islands and austenite phases, higher PEEQ values can be observed than Group 1, since the areas are much lighter. These PEEQ values now range between 0.1667 to 0.667 for both phases, although the retained austenite illustrates more of the lighter areas of the scale. To this point, in Subgroup Ai, no PEEQ response is observable in the ceramic inclusions. Also, within Groups 2-5, no significant difference can be noticed between the microstructures, indicating that the material properties of the ceramic inclusions still have no feasible effect on the over PEEQ response.

With the addition of 4% more ceramic inclusions in Subgroup Aii, more areas of high PEEQ concentrations form more notably around the ceramic inclusions and bainite islands. The bainite constituents now indicate PEEQ ranging from 0.1667 to 0.667 but indicating more areas closer to the higher end of the scale, while the retained austenite phases are now ranging from 0.333 to 1.0. The ferrite is also, as predicted, shows more prevalent branches and areas of higher PEEQ ranging from 0.5 to 1.333 with branches and concentration areas ranging from 1.333 to 2.0. Much higher maximum PEEQ values can also be seen compared to those presented in Subgroup Ai. Now, Group 2-Silicon Carbide illustrates a maximum PEEQ value of 3.479 followed by Group 5- Aluminum Oxide with 3.423, Group 4- Zirconia with 3.182, and finally Group 3-Cementite with 3.118. Now that more percentage of ceramic particles are presented into the microstructure, the PEEQ does not solely concentrate on the bainite phases, but also engender and spread to neighboring ceramic inclusions. This fact also explains why

these branches or paths are created between PEEQ concentrated regions, simulating potential areas of crack propagation and ultimately, fracture.

In Subgroup Aiii, this is further supported. As shown in Figure 56, due to a 5% increase in the volume fraction of ceramic inclusions and a 5% decrease in the volume of ferrite, more hard interfaces are vulnerable to strain localization, allowing for the high PEEQ concentrated areas around the bainite phases and ceramic particles to spread and connect easier to similar neighboring areas. Thus, the ceramic interfaces allow for a simpler "path" for the high PEEQ regions to spread throughout the microstructure. Also, the PEEQ has increased in value, or visually become lighter, throughout the microstructure except within the ceramic inclusions which still illustrate no plastic strain. Although the bainite still ranges from 0.1667 to 0.667, there are more quantities of lighter regions that illustrate higher values of PEEQ. Some areas around the border of the bainite islands are also beginning to match the colors or PEEQ of the ferrite. The austenite PEEQ values have also increased to a range of 0.333 to 1.167 and in some areas is extremely difficult to depict from the ferrite matrix. Few and small areas of maximum PEEQ can also start to be seen, particularly between ceramic inclusions that are very close together and also close to a bainite island. Besides Group 2-Silicon Carbide, the maximum PEEQ values at 80% strain for Subgroup Aiii are less that those presented in Subgroup Aii. Now, these maximum values for Groups 3,4 and 5 are 2.790, 2.808, and 2.953 respectively. Group 2 is the only microstructure that illustrates a higher maximum PEEQ value in Subgroup Aiii than Subgroup Aii of 3.717. This is due to the fact that silicon carbide illustrates the largest modulus of elasticity, thus provides the

highest difference in properties from the neighboring constituents in the particle reinforced TRIP microstructure. Therefore, this material interface provides the highest vulnerability to high PEEQ concentrations than the other materials. This may be explained better at the final observed strain of these microstructures.

Besides the strain at which the ultimate tensile stress occurs, the final stage of loading, or 100% strain illustrates the most important PEEQ behavior for each microstructure for analysis in terms of comparing subgroups. This stage of strain indicates how the material would behave if the microstructure had the ability to deform to 100%. At this strain level it is possible to visualize where and how severely the strain localizes throughout the structure. The areas and localizations of strain at this stage will also allow a clear visualization of the main mechanism that would drive each microstructure to failure. This behavior is shown in the following responses illustrated through Figures 56 - 58.

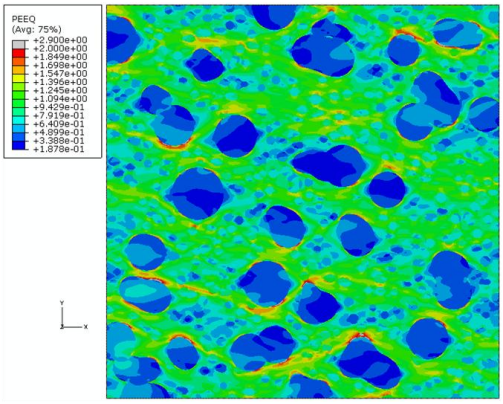

Group 1: A

Subgroup Ai

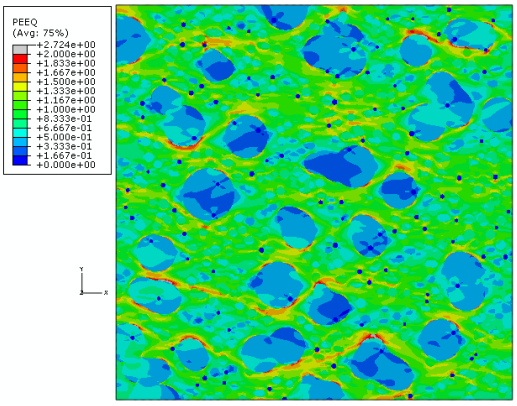

Group 2: Silicon Carbide

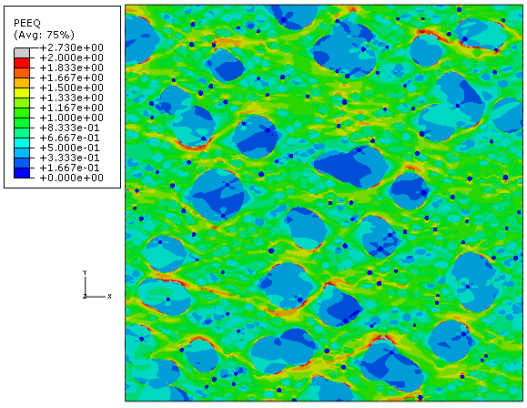

Group 3: Cementite

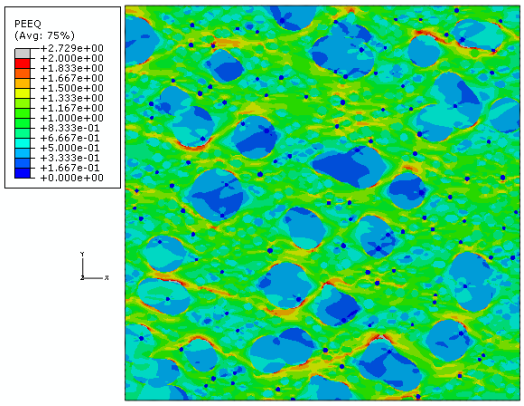

Group 4: Zirconia

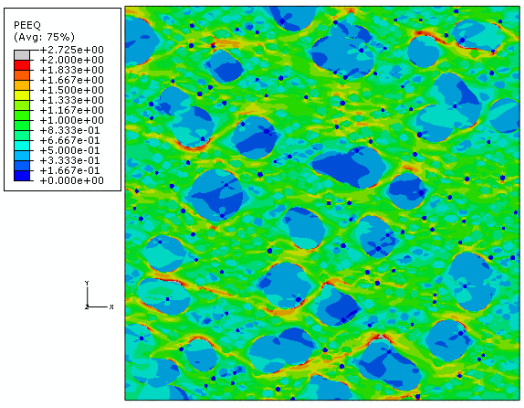

Group 5: Aluminum Oxide

Figure 56 PEEQ for Group 1 and Subgroup Ai at 100% strain

Subgroup Aii

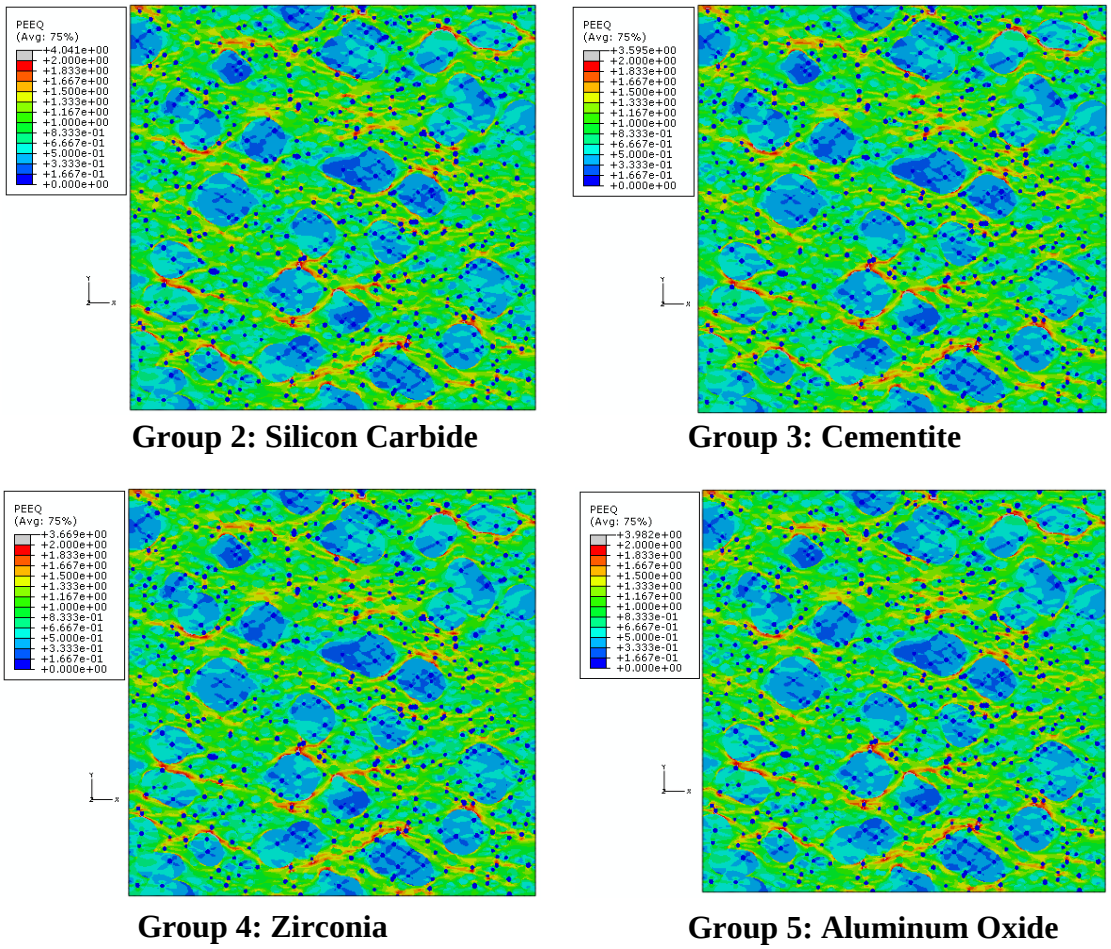

Figure 57 PEEQ for Subgroup Aii at 100% Strain

Subgroup Aiii

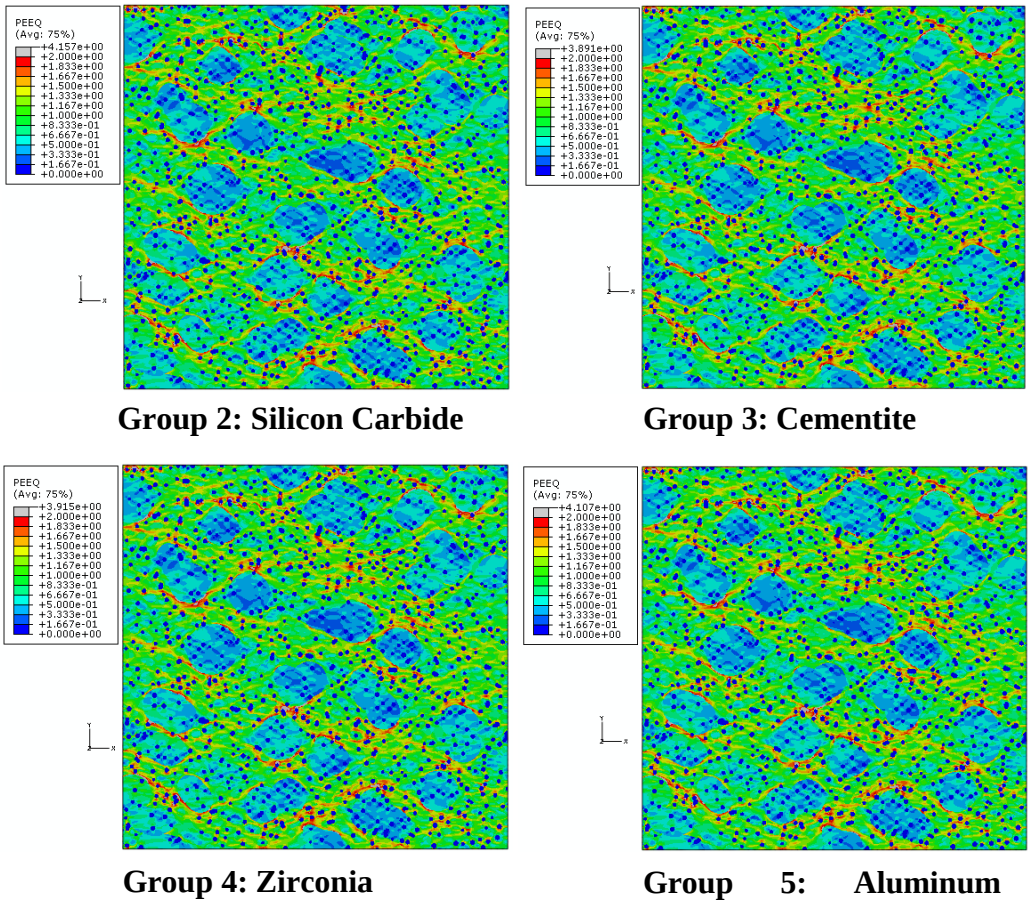

Group 2: Silicon Carbide **Group 3: Cementite**

Group 4: Zirconia **Group 5: Aluminum**

Figure 58 PEEQ for Subgroup Aii at 100% strain

At 100% strain, Group 1was described to illustrate the strongest localized PEEQ concentrations around the bainite interface with PEEQ's ranging from 1.698 to 2.90. Few concentrations were beginning to form around the austenite interfaces. This is where the high PEEQ concentrations began, and are nor seen to proliferate through the microstructure towards similar areas nearby. The PEEQ illustrated by the bainite ranges from 0.1878 to 0.7919, while the retained austenite phases illustrate a PEEQ ranging from 0.3388 to 0.7919. As usual, the retained austenite shows many more lighter color or higher PEEQ areas than the bainite. Besides the concentrations, the branches spreading through the ferrite in the microstructure that exhibit a yellow or orange color indicate a PEEQ range from 1.396 to 1.698. The remaining ferrite illustrates regions of PEEQ ranging from 0.641 to 1.396.

With the addition of 1% ceramic particles, at 100% strain, visually, a much lighter green and minimal shades of dark blue are now presented through the ferrite. Although the ferrite PEEQ seems to have a range of 0.5 to 1.333 with more areas concentrated on the higher end of the scale, the branches indicated in Group 1 are slightly longer in Subgroup Ai with PEEQ values of 1.333 to 1.6667. As explained before, the presence of ceramics, even with a 1% volume fraction, offers another vulnerable interface to localized plastic strain, and thus allows for another pathway for these localizations to travel throughout the ferrite in the microstructure. This will become more prevalent as the other subgroups are observed. Higher values of PEEQ are also seen throughout the bainite and austenite compared to Group 1. Again, although the bainite PEEQ seems to range from about 0.1667 to 0.667, there are many more light

regions than Group 1. Retained austenite also follows the same trend as bainite in which more of the higher part of the scale is exposed in the PEEQ with a range of 0.33 to 1.333. As for the maximum strain values between the different groups, all the groups are extremely similar and are about 2.73. There difference at 100% strain for Subgroup Ai is negligible between Groups 2-5. Thus, for the austenitic structures in Subgroup Ai, the material properties of the ceramic inclusions have no direct effect on the equivalent plastic strain behavior of the particle reinforced TRIP steel. Yet, the presence of ceramic inclusions does have an effect on the PEEQ of all the constituents presented in which the PEEQ increases and seems more distributed throughout the microstructure. Also, this also may explain why with 1% ceramic inclusions, the maximum PEEQ presented throughout the microstructure decreases from Group 1 with a maximum PEEQ of 2.90 to Subgroup Ai that all illustrate maximum PEEQ's close to 2.73. Also, even at 100% strain for the austenitic structures in Subgroup Ai, the ceramic inclusions still illustrate no sign of equivalent plastic strain.

As illustrated in the previous strain configurations, the addition of more ceramic inclusions causes higher areas of PEEQ concentrations and more branches connecting them. For Subgroup Aii, the ferrite now has regions of PEEQ ranging from 0.67 to 1.333 with more thin branches or paths that contain much more yellow, orange and even red colors indicating PEEQ ranges of 1.33 to 1.833. These connect the very large localized strain areas of 1.833 to about 4.0 surrounding the bainite constituents and most ceramic inclusions. The bainite has increased its PEEQ range to 0.1667 to 0.833 illustrating many more light areas as does the austenite which has PEEQ regions ranging from 0.5 to

1.333. Unlike Subgroup Ai, the material groups within Subgroup Aiii show some differences in maximum PEEQ values. Group 2- Silicon Carbide illustrates the highest maximum PEEQ value in Subgroup Ai with 4.041 followed by Group 5- Aluminum Oxide with 3.982, Group 4-Zirconia with 3.669, and finally Group 3-Cementite with 3.595. This trend follows the descending values of Young's modulus for each ceramic material. For example, silicon carbide illustrates the highest Young's modulus of 480GPa, followed by aluminum oxide with 380GPa, zirconia with 205GPa, and cementite with 190GPa. This sequence is congruent to that of the maximum PEEQ for each group presented in Subgroup Aii. The larger the difference in material properties between the TRIP steel constituents and the reinforcing ceramic particles, the higher PEEQ values are presented in the microstructure, especially around the harder constituent interfaces. Thus, the larger the modulus of elasticity of the ceramic inclusion, the more susceptible the interface between it and the TRIP steel constituents becomes too high strain localization.

This trend is also supported through Subgroup Aiii, in which a total of 10% volume of ceramic particles is introduced into the microstructure. The PEEQ responses for Subgroup Aiii illustrate the same continuing behavior as the previous explained frames. To reiterate, more large valued PEEQ branches are shown spreading more rigorously through the microstructures in this subgroup due to the addition of more inclusions as previously described. Also, the PEEQ values have also increased within all constituents except the ceramic inclusions which still illustrate no PEEQ values above 0. The bainite phases range from 0.333 to 1.167 with many more light regions than the

other subgroups and the control. The austenite phases have also increased their range from 0.5 to 1.333 to be extremely similar to the surrounding ferrite. The ferrite illustrates areas with PEEQ ranging from 0.667 to 1.333 with numerous branches simulating potential crack areas with PEEQ ranging from 1.333 to 2.0 connecting high strain localization areas illustrating PEEQ values of 2.0 to the maximum PEEQ of the microstructure. These maximum strain values occur mainly within these spreading branches near the interfaces of ceramic inclusions. As in Subgroup Aii, Subgroup Aiii also illustrates the same relationship between the material groups in which Group 2-Silicon Carbide illustrates the largest maximum PEEQ of 4.157 followed by Group 5-Aluminum Oxide with 4.107, Group 4-Zirconia with 3.915, and finally Group 3-Cementite with 3.891. These values are much higher than the maximum PEEQ displayed in the corresponding microstructure in Subgroup Aii. The increase in this value from Subgroup Aii entails the addition of more ceramic inclusions. The deformed microstructures for each RVE are illustrated below in Figures 59 - 61 as well to show how these microstructures look at the final stage of deformation and how these cracks spread through the deformed structure as the volume fraction of ceramic particles increase.

Subgroup Ai

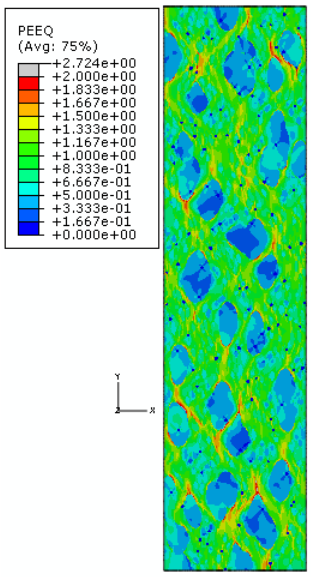

Group 2: Silicon Carbide

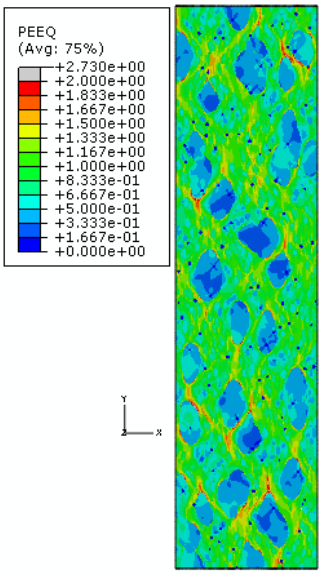

Group 3: Cementite

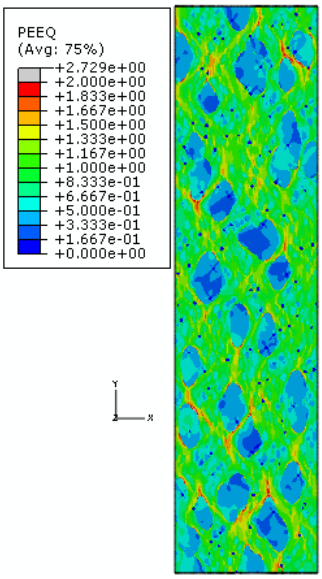

Group 4: Zirconia

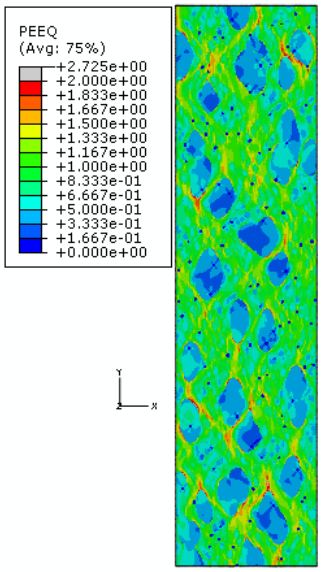

Group 5: Aluminum Oxide

Figure 59 PEEQ for Subgroup Ai at 100% strain-deformed microstructure

Subgroup Aii

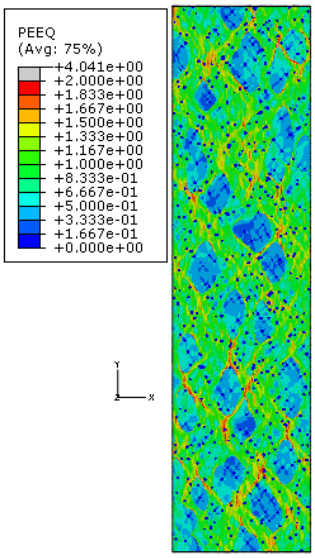

Group 2: Silicon Carbide

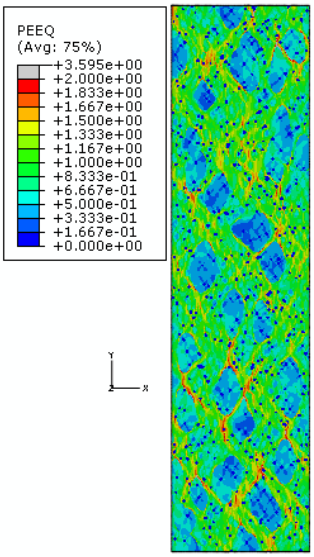

Group 3: Cementite

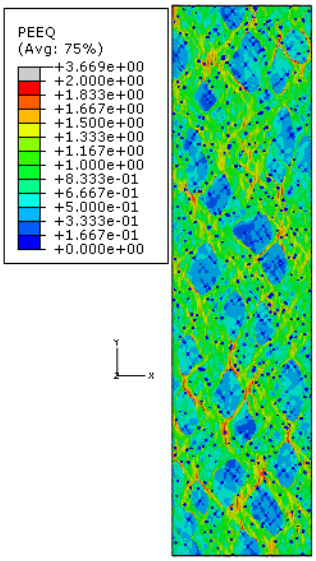

Group 4: Zirconia

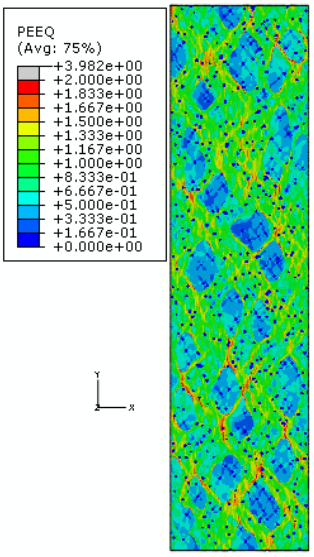

Group 5: Aluminum Oxide

Figure 60 PEEQ for Subgroup Aii at 100% strain-deformed microstructure

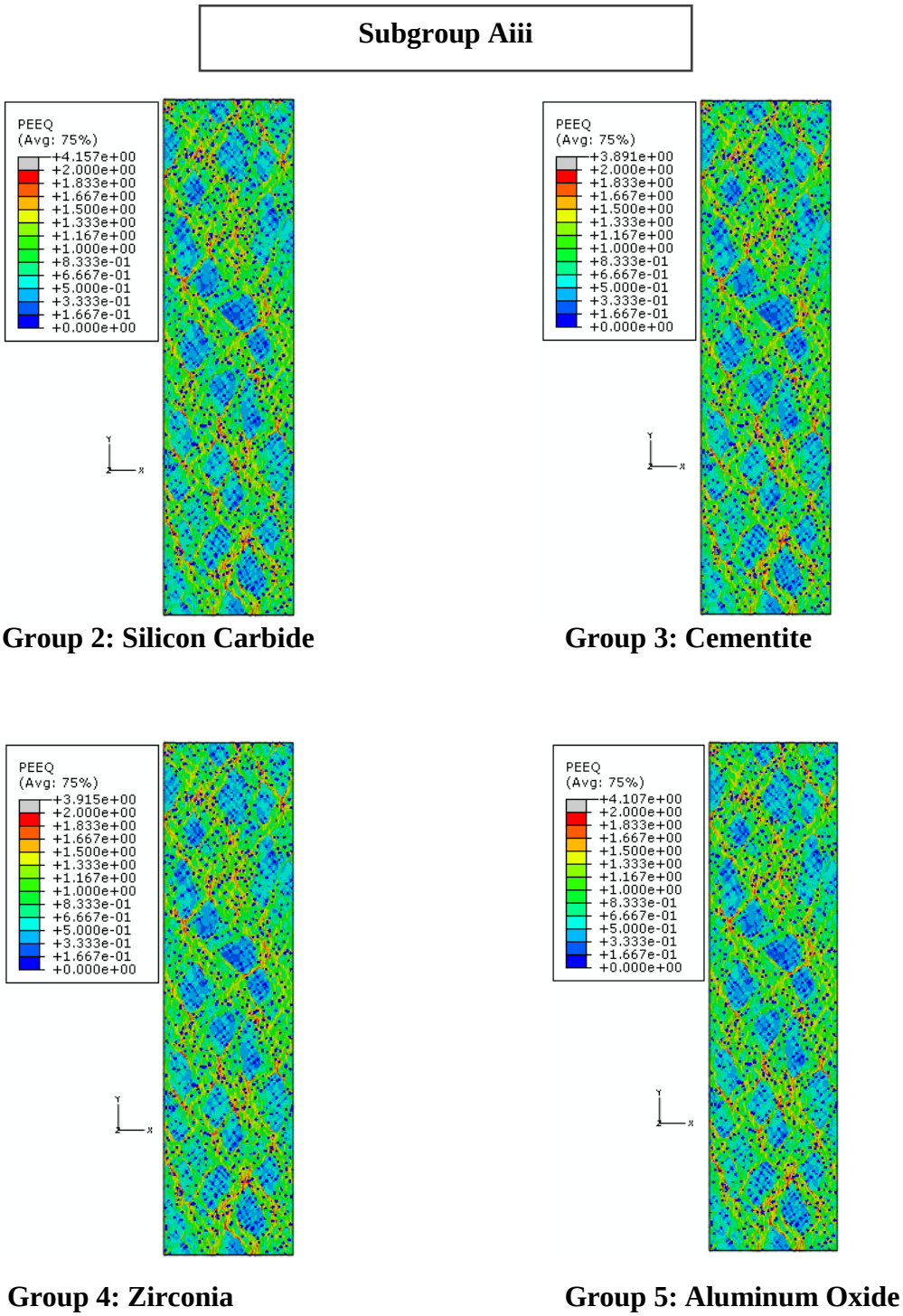

Figure 61 PEEQ for Subgroup Aiii at 100% strain-deformed microstructure

Now that the austenitic or initial structure has been analyzed for each case, the corresponding transformed or martensitic phase will be compared to the other RVE's in the same manner to see how different the PEEQ behaviors are and how the full transformation of austenite to martensite affects the reinforced ceramic particle TRIP steel composite. These RVE's are exactly the same as the previous analyzed RVE's with the only modification being that the austenite within each phase is now martensite, thus introducing a harder more brittle phase into the microstructure that is predicted to perform similar to the ceramic particles. First, as done previously, the microstructures are presented at 40% strain and also compared to their corresponding control structure At from Group 1. As before, depending on the microstructure, 40% strain will most likely indicate the beginnings of plastic strain for the softer phases presented in the microstructure. Unlike the austenitic structures, since martensite is now presented in the TRIP steel, plastic strain will most likely not occur in the martensite at this strain level. These PEEQ responses that were recorded, compared, and analyzed at this strain level are shown through Figures 62 - 64.

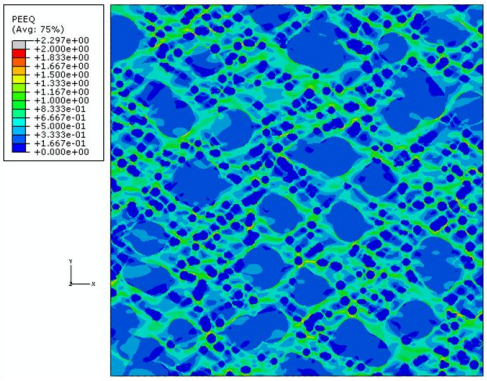

Group 1: At

Subgroup Ati

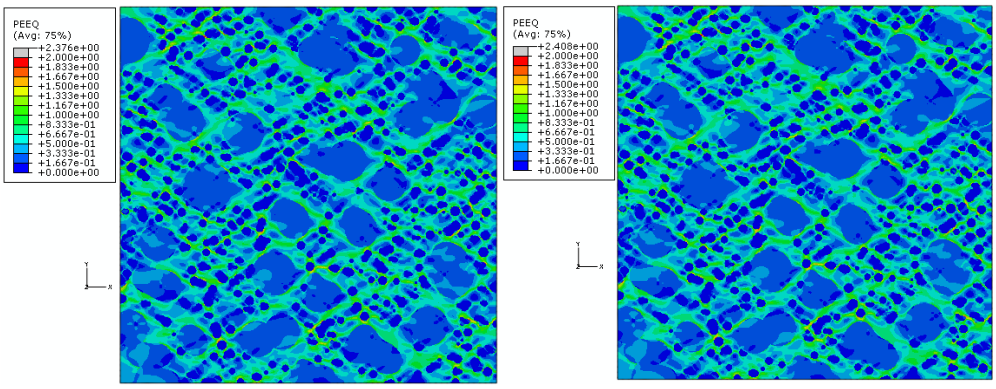

Group 2: Silicon Carbide **Group 3: Cementite**

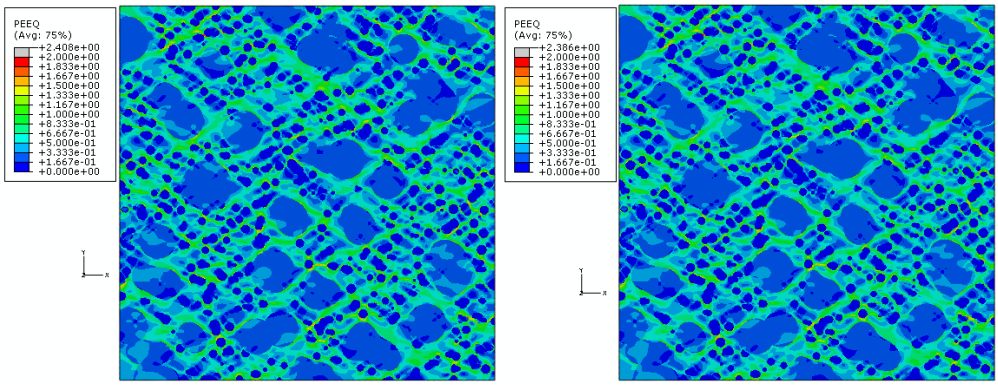

Group 4: Zirconia **Group 5: Aluminum**

Figure 62 PEEQ for Group 1 and Subgroup Ati at 40% Strain

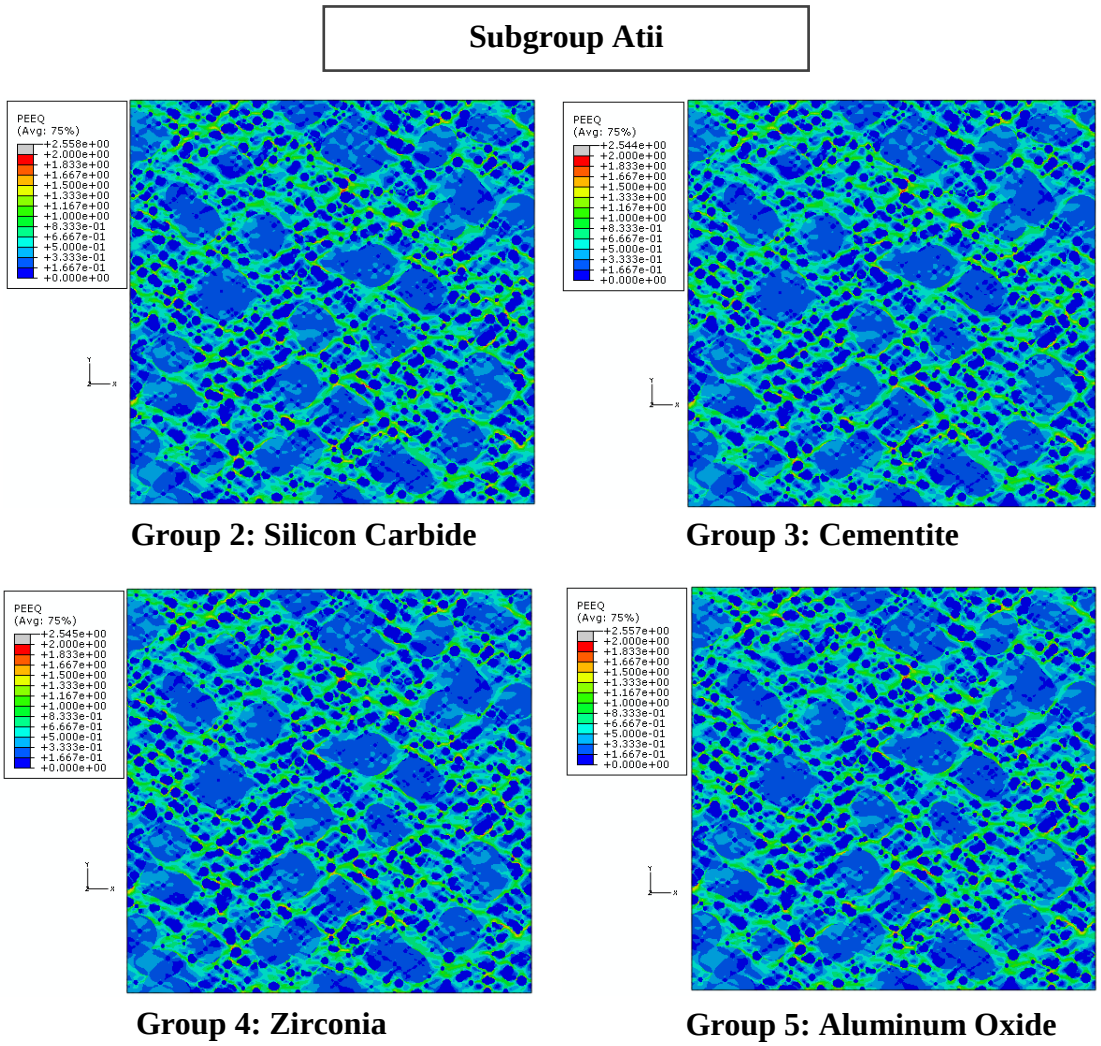

Figure 63 PEEQ for Subgroup Atii at 40% strain

Subgroup Atiii

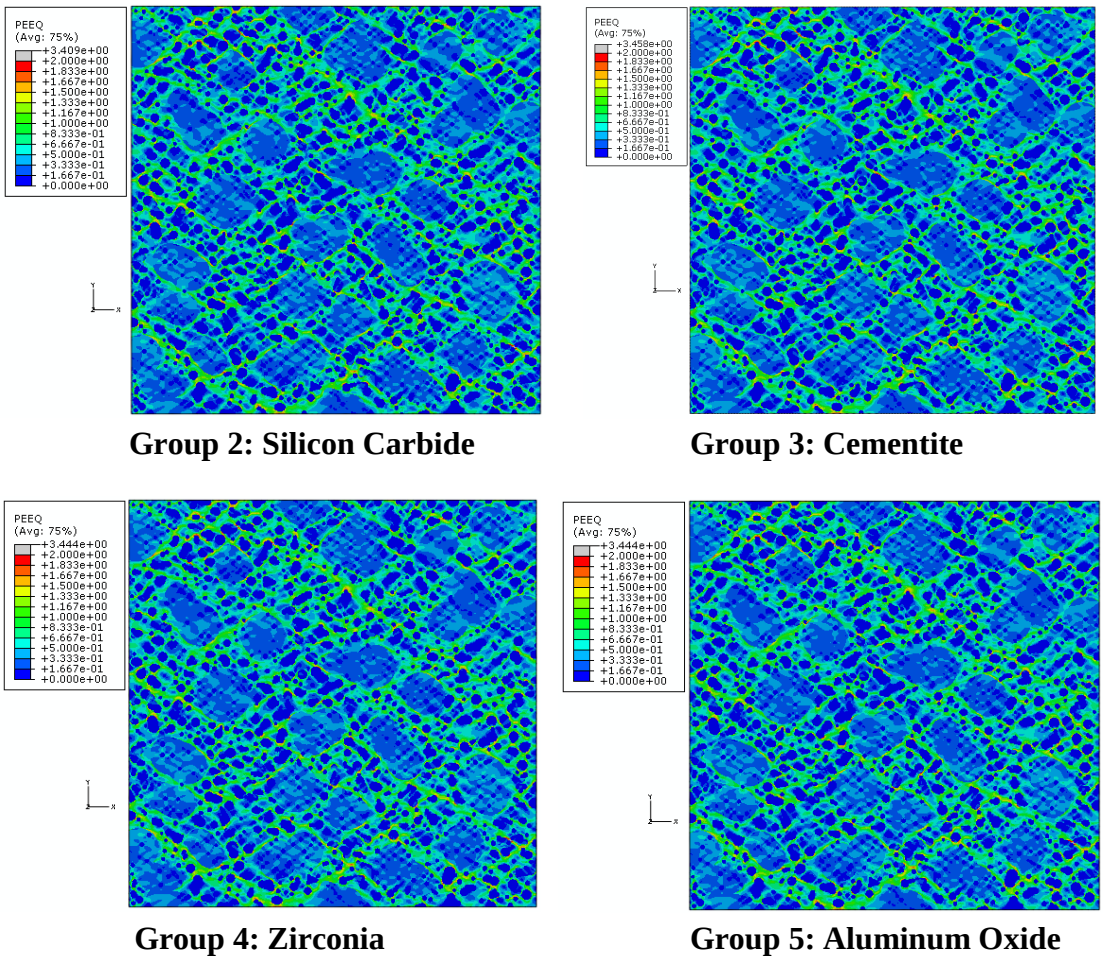

Group 2: Silicon Carbide **Group 3: Cementite**

Group 4: Zirconia **Group 5: Aluminum Oxide**

Figure 64 PEEQ for Subgroup Atiii at 40% strain

Revisiting the PEEQ analysis described for structure At in Group 1, areas of high concentrations can already be depicted between the martensitic phases as opposed to all the austenitic microstructures analyzed. This is due to the fact that martensite is a much harder and more brittle phase than austenite and also bainite, thus the concentrations begin at a much earlier strain between the interfaces of these phases and the remaining constituents. Unlike the austenitic structures, minimal to no concentrations engender at the bainite interfaces. The ferrite matrix for microstructure At in Group 1 has PEEQ ranging from 0.1667 to 1.167 while the bainite illustrates less PEEQ ranging from 0.1167 to 0.5. At 40% strain, the martensite phases, depicted by the darkest blue areas, illustrate 0 PEEQ. The maximum PEEQ presented in structure At is 2.297.

Subgroup Ati, in which 1% ceramic inclusions are introduced into the microstructure, illustrates very similar behavior to that of Group 1 structure At, with a slightly higher maximum PEEQ for each group. Here it seems like the added ceramics are behaving similar to martensite. The PEEQ concentrations still occur in the same areas in Subgroup Ati as in Group 1. Thus, the addition of ceramics seem negligible to the visual PEEQ behavior of the particle reinforced TRIP steel composites. The small addition of ceramics seems to simply add to the maximum PEEQ value presented in the structure at 40%. It is safe to assume that at 40% strain, for this subgroup, martensite governs over the ceramic particles in contributing to the PEEQ response of the microstructure. There is a small difference between the maximum values of PEEQ amongst the groups in this subgroup. The highest occurs in Group 3- Cementite and Group 4- Zirconia, both with a maximum PEEQ of 2.408. Group 5- Aluminum Oxide

follows with a maximum PEEQ of 2.386 and then Group 2- Silicon Carbide with a maximum PEEQ of 2.376. This difference seems very small, thus higher strain frames will provide more useful information on how 1% addition of ceramic inclusions affects the microstructure as a whole.

Subgroup Atii, with a total volume fraction of 5% ceramic inclusions illustrate a slightly larger effect on the microstructure. The dramatic difference in the strain bands proliferating through the ferrite visible in the austenitic structures are not presented in their transformed microstructures at 40%. Again, this is most likely due to the fact that the martensite presents a hard phase competitive with the ceramic phases since the martensite can almost be considered as elastic Also, instead of occurring around the bainite phases, large PEEQ concentrations begin to form around the martensite and ceramics. Although the range of PEEQ for the ferrite and bainite have not changed much, more frequent areas of higher strain concentrations do exist compared to Subgroup Ati. This is due to the fact that more ceramics are present, thus more areas of strain localization are introduced into the microstructure. As in Subgroup Ati, the different material groups within Subgroup Atii do not have a significant difference to say that material has any effect on the overall PEEQ response of the material. All groups here have a maximum PEEQ value of about 2.55. The small variations in plastic strain within the ferrite and bainite constituents occur due to the addition of ceramic inclusions into or near the phase. This can be seen with lighter colors beginning around ceramics within the bainite islands, for example, verses previous subgroups in which no ceramic

inclusion is trapped within the constituent. This will become more evident at later strain values.

Subgroup Atiii at 40% begins to illustrate more clearly thinner and more prevalent branches of PEEQ within the ferrite spreading through the microstructure. There is still not big difference in the groups within the microstructure with all ranging close to a maximum PEEQ value of 3.4, yet this value is higher than the previous analyzed martensitic structures to this point. All the microstructures in Subgroup Atiii illustrate more areas of high PEEQ strain localizations occurring around the martensite phases and ceramics. The bainite islands illustrate no areas of high PEEQ concentrations. Also, as previously described in Subgroup Atii, since there are more ceramic particles distributed throughout Subgroup Atiii, lighter colored regions are presented in the bainite islands and ferrite matrix especially surrounding areas where a ceramic inclusion is present. This indicates that PEEQ values increase in areas surrounding the ceramic particles. At this point, also, no plastic strain is observed in the martensite or the ceramic inclusions. These hard constituents simply serve as vulnerable interfaces where cracks or voids may begin if debonding were a consideration.

The next frames and important indicators of ductility are observed at the strain in which the ultimate tensile stress occurs. The following PEEQ responses and their corresponding strains were recorded in Figures 65 - 67.

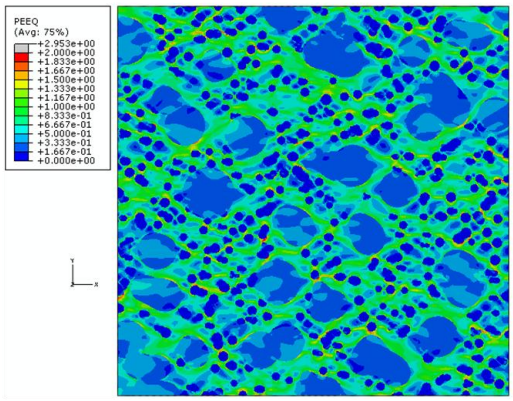

Group 1: At - 52% Strain

Subgroup Ati

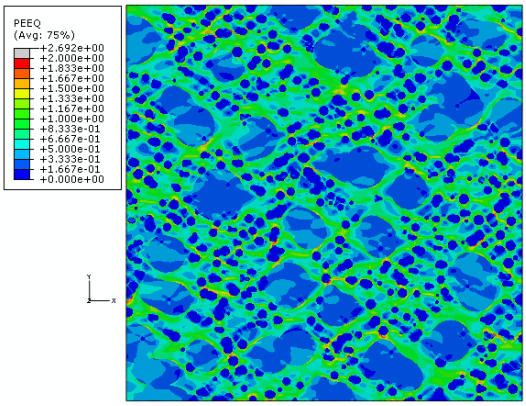

Group 2: Silicon Carbide-52.2%

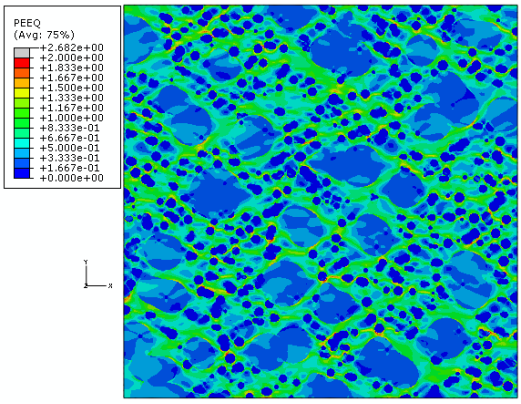

Group 3: Cementite-

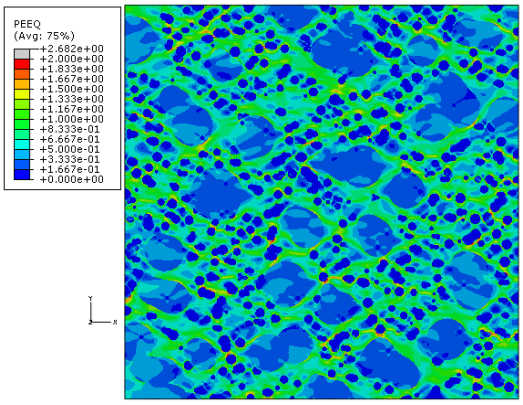

Group 4: Zirconia-51.6%

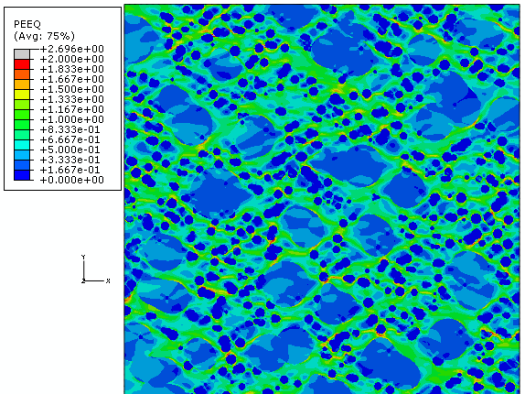

Group 5: Aluminum Oxide-52.5%

Figure 65 PEEQ for Subgroup Ati - ultimate tensile strength

Subgroup Atii

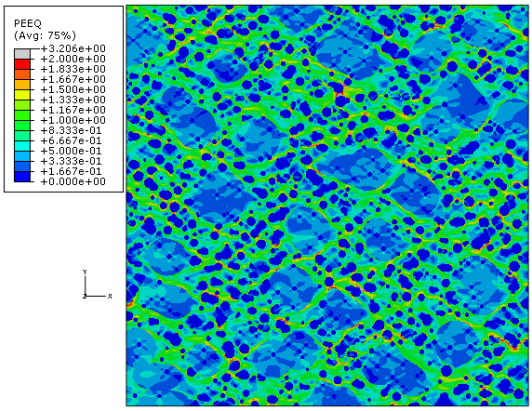

Group 2: Silicon Carbide-54.5%

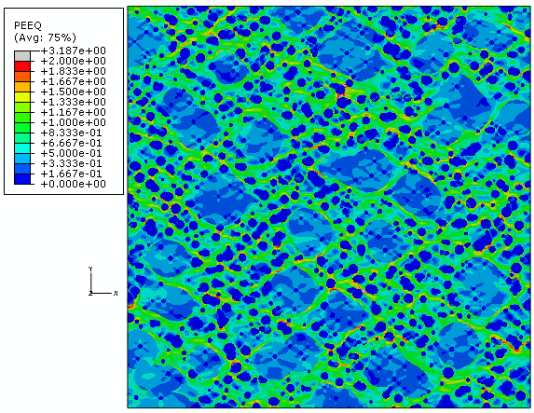

Group 3: Cementite-54.2%

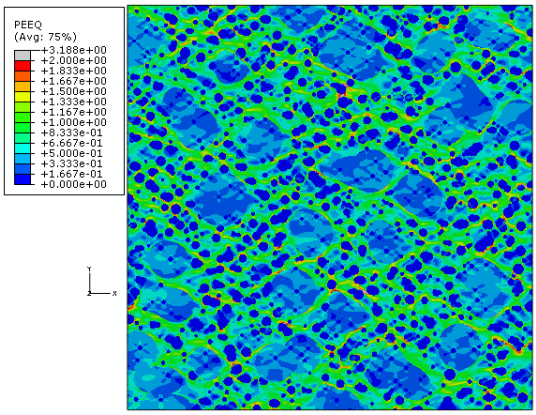

Group 4: Zirconia-54.2%

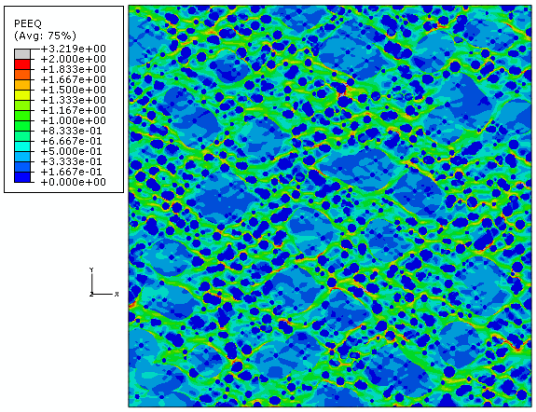

Group 5: Aluminum Oxide-

Figure 66 PEEQ for Subgroup Atii - ultimate tensile strength

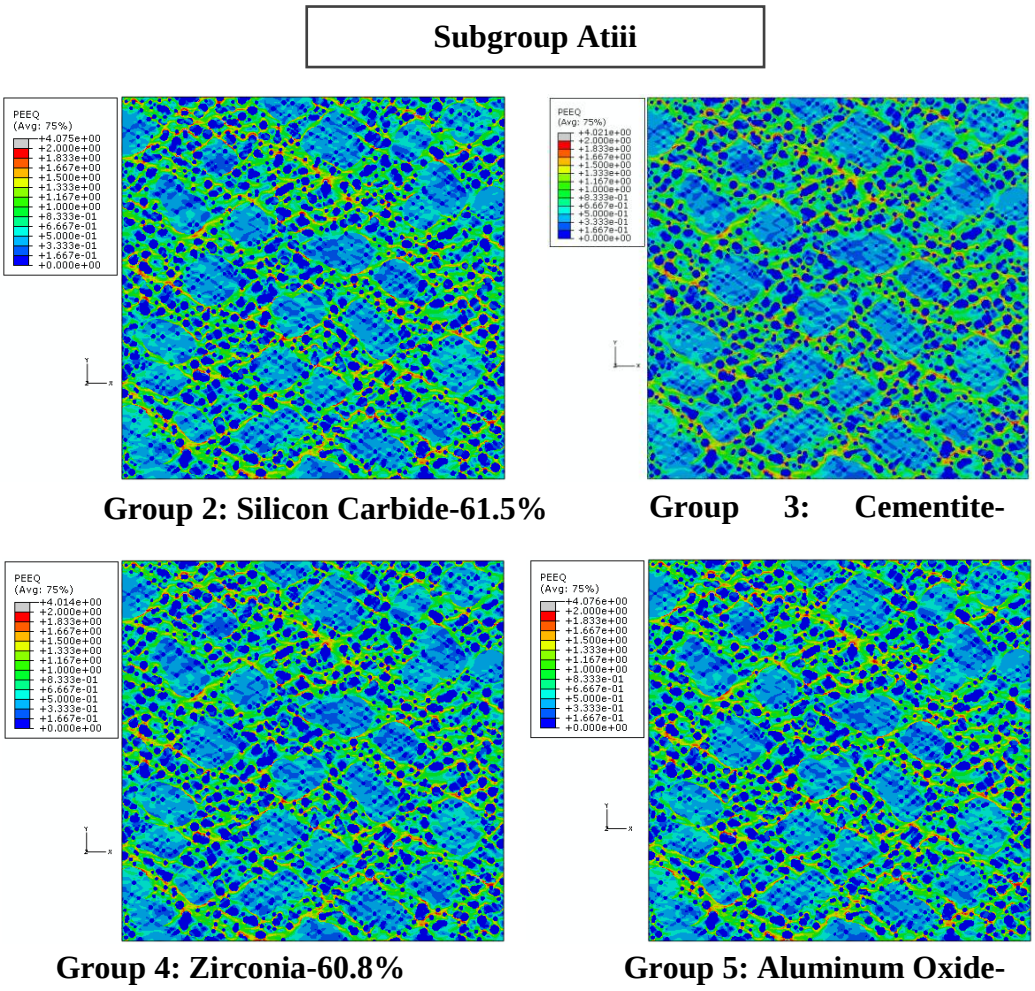

Figure 67 PEEQ for Subgroup Atiii - ultimate tensile strength

At ultimate strength, the main factor to look at is the strain value at which this occurs in order to see how much ductility has enhanced or decreased. For Group 1, At, the ultimate tensile strength occurs at 52% strain. As before, high PEEQ concentrations can be seen surrounding the martensite and showing small paths or branches to other neighboring areas of high PEEQ values throughout the ferrite matrix. The PEEQ

throughout the ferrite matrix ranges from 0.333 to 1.167 with thin yellow branches of PEEQ values ranging from 1.333 to 1.667 connecting high PEEQ concentrations of 1.667 to 2.953. The bainite phases illustrate PEEQ values ranging from 0.1667 to 0.667. No plastic strain can be observed within the martensite or ceramic particles.

Subgroup Ati proves to be extremely similar to microstructure At in almost all aspects except that the maximum PEEQ for this subgroup is smaller, about 2.69 for all microstructures. Also, despite the materials utilized in each group, the PEEQ responses are once again congruent among the microstructures and also all very close to 52%. Thus 1% increase in ceramic inclusions does not cause too much difference from the original martensitic structure in Group 1. As before, this is due to the ceramics acting as a small addition to the martensitic effects, although martensite seems to govern in this subgroup. The ferrite PEEQ now ranges from 0.333 to 1.333 with slightly longer yellow branches compared to At with PEEQ values ranging from 1.333 to 1.667. The high PEEQ concentration areas are still present in the same areas as that of structure At, except now the PEEQ values have slightly lowered to 1.667 to 2.69. Since there are more areas for these concentrations to "spread out", less PEEQ is concentrated solely in interfaces of the martensite and ceramics. Thus, the ceramics are somewhat alleviating some of the strain from the martensite interfaces causing a smaller maximum PEEQ value in Subgroup Ati. The bainite regions still illustrate PEEQ values ranging from 0.1667 to 0.667. Very small areas of lighter colors can be depicted within the bainite islands where ceramic particles are present.

Subgroup Atii, with an addition of a total of 5% ceramic inclusions, illustrates even more areas of branching strain localization throughout the ferrite. As before, more branches are prevalent through the ferrite indicating more ceramic particles and higher areas of PEEQ. The ferrite PEEQ ranges from 0.5 to 1.333 where the branches are again 1.333 to 1.667 connecting areas of high PEEQ ranging from 1.667 to about 3.2. As in Subgroup Ati, the maximum strains amongst the different groups in the subgroup are extremely similar and all very close to 3.2. Here, all the microstructures, once again are very close to 54% strain at which ultimate strength occurs. This once again explains that at this stage for these microstructures, the ceramic material properties have negligible effects on the microstructure. Although the values are extremely close, it is worth noting that Group 5- Aluminum Oxide illustrates the most ductile of the group by less than 1% with a strain value of 54.9% followed by Group 2-Silicon Carbide at 54.5%. Group 3-Cementite and Group 4-Zirconia illustrate the same strain at ultimate of 54.2%. Also, as predicted the bainite islands still range from 0.1667 to 0.667 in PEEQ, except there are more lighter regions throughout the bainite phases.

A more notable difference in strain increase can be seen in Subgroup Atiii amongst the different material groups. Group 5- Aluminum Oxide illustrates the most ductile microstructure with a strain value of 61.8% followed very closely by Group 2-Silicon Carbide with a strain value of 61.5%. Group 4-Zirconia is the next highest in ductility with 60.8% strain and finally Group 3-Cementite illustrates the least ductile microstructure with 60.1% strain. The harder ceramic materials with the higher modulus of elasticity enhance the ductility of the particle reinforced TRIP steel. Yet, if the

material is too hard, as in the case of the silicon carbide, ductility begins to slightly decrease, but not to a significant amount to impede this observation. This may be explained in the sense that since these phases are ideally perfectly bonded, the harder ceramics illustrate a constituent that is much harder than the other constituents and can absorb more of the stress occurring throughout the microstructure. Thus, by absorbing the majority of the stress, this alleviates the remaining constituents from experiencing a larger amount of stress, and stretch even further. Also, since there are more ceramics throughout the microstructures in Subgroup Atiii, more stress may be absorbed by these ceramics, thus allowing the particle reinforced TRIP steel composite to elongate even further. Again, this is crucial to the idea that these phases are perfectly bonded and no damage is presented. Despite this, more areas of potential cracks are presented throughout the ferrite in the microstructure yet the PEEQ values are similar to the other microstructures. Yet, the maximum PEEQ regions have increased to about 4.0 for Subgroup Atiii. The PEEQ in the bainite has also increased to range from 0.333 to 0.833. Also, this subgroup illustrates PEEQ engendering within the martensitic phases in a few areas ranging from no PEEQ to faint areas of 0.667.

At 80% strain the microstructures continue to follow the same predicted trend in Figures 68 - 70.

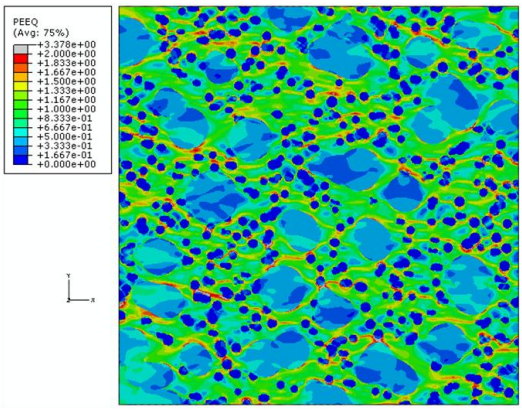

Group 1: At

Subgroup Ati

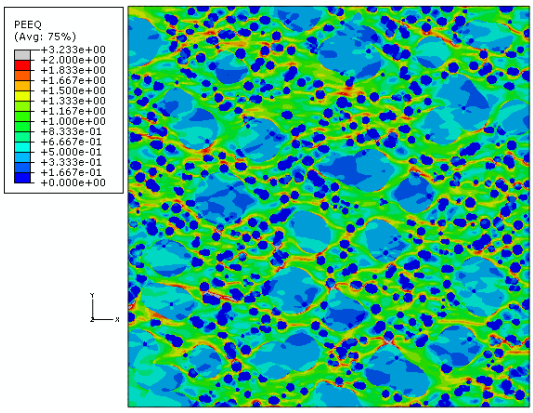

Group 2: Silicon Carbide

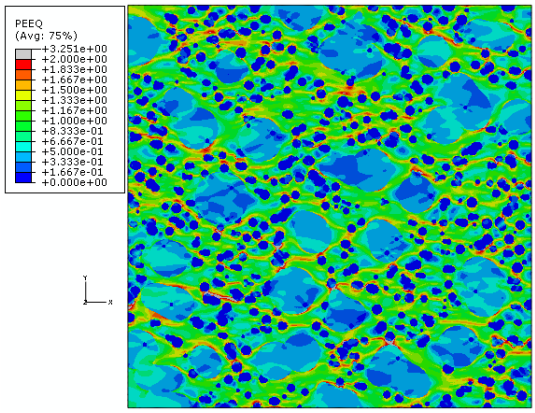

Group 3: Cementite

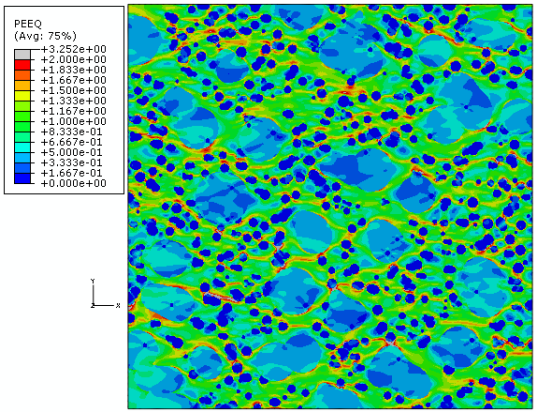

Group 4: Zirconia

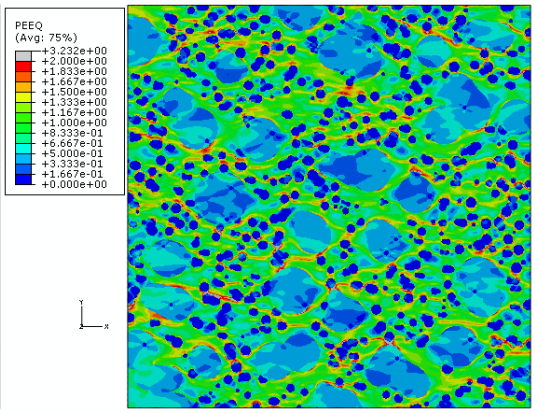

Group 5: Aluminum Oxide

Figure 68 PEEQ for Group 1 and Subgroup Ati at 80% strain

Subgroup Atii

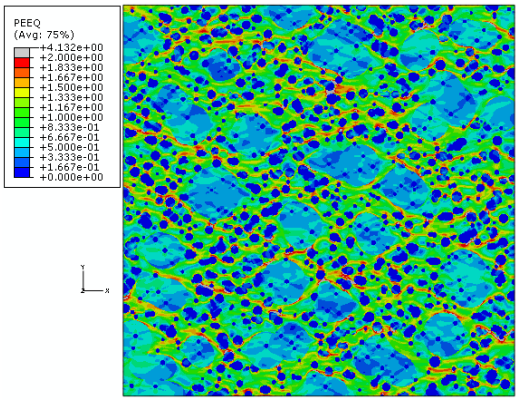

Group 2: Silicon Carbide

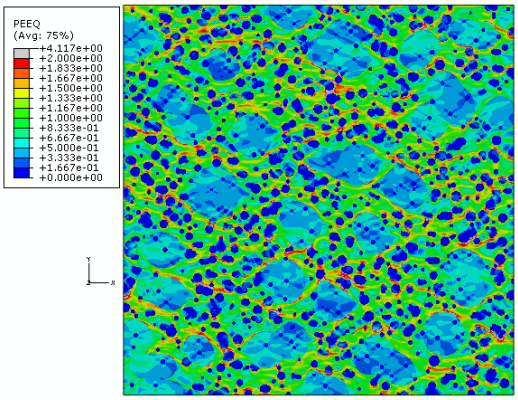

Group 3: Cementite

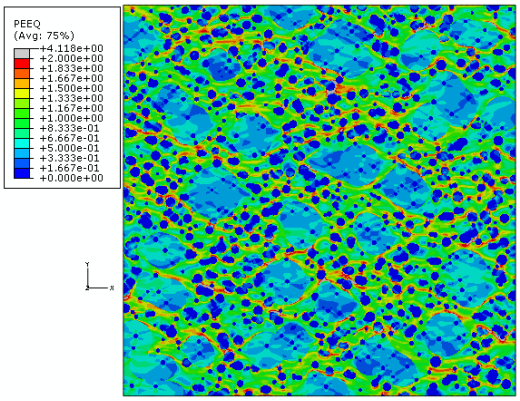

Group 4: Zirconia

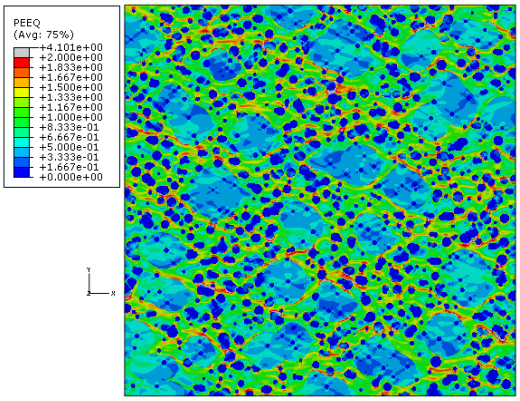

Group 5: Aluminum

Figure 69 PEEQ for Subgroup Atii at 80% strain

Subgroup Atiii

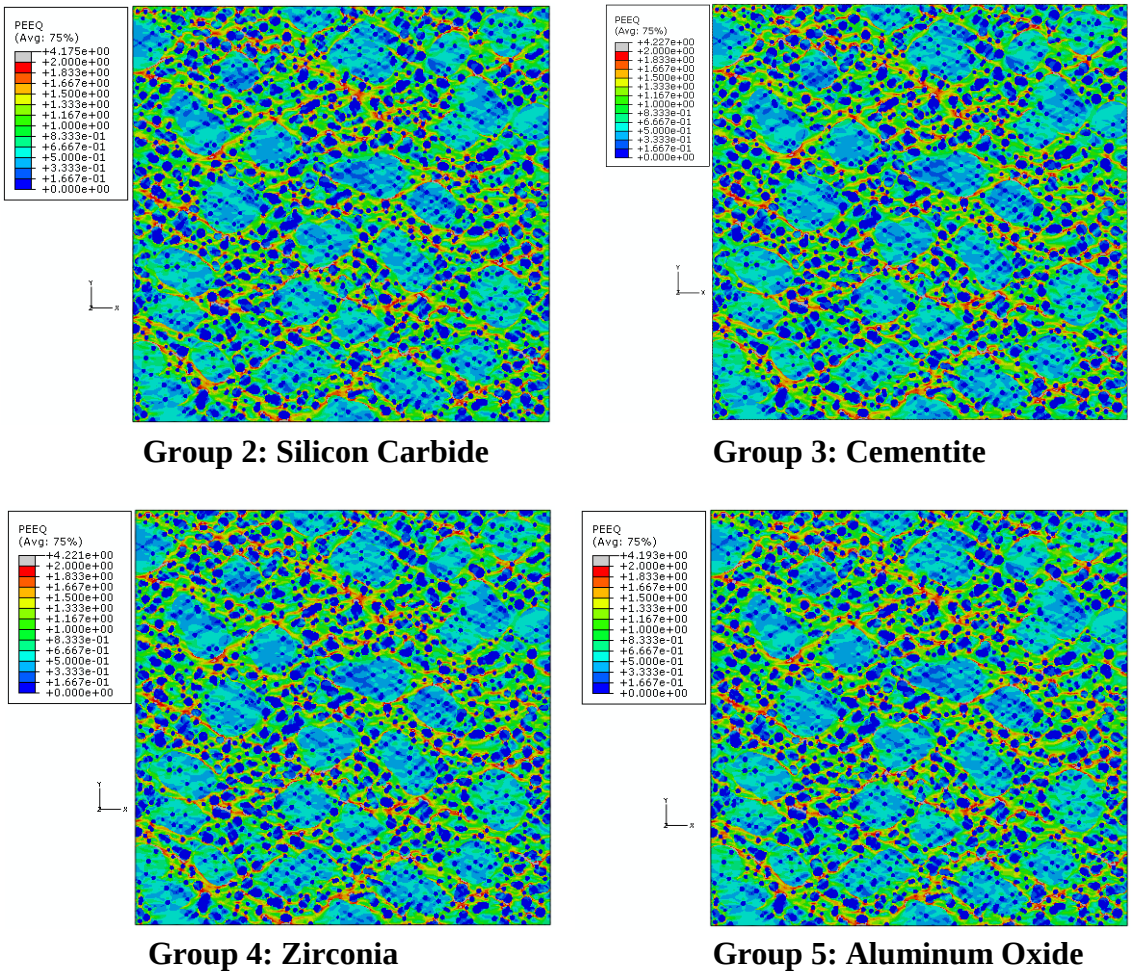

Figure 70 PEEQ for Subgroup Atiii at 80% strain

At 80% strain structure At from Group 1 illustrates the behavior previously described. To be brief, the strain around the martensite and bainite structure has spread throughout the microstructure. The maximum PEEQ presented in this microstructure is 3.378.

Similar to the other subgroups, Subgroup Ati at 80% strain illustrates a slightly smaller maximum PEEQ for the microstructures of about 3.2. The material utilized for the ceramics in each group again seems negligible for the overall response of the composite. This is because, once again, the maximum strains are so similar through each group within each subgroup and the visible PEEQ responses are identical as well. This holds true for the remaining subgroups for the martensitic structures to avoid repetition. For this subgroup, the PEEQ values for each microstructure are identical to that of the corresponding structure in Group 1. The ferrite still ranges in PEEQ from 0.667 to about 1.333 with branches of 1.333 to 2.0. The maximum values can be slightly depicted in the areas around the interfaces of the martensite and ceramic particles. The bainite PEEQ response is also similar to that of the microstructure in Group 1 with values ranging from 0.1667 to 0.667. The martensite is actually also starting to show very faint signs of PEEQ responses ranging from 0 to 0.667. This response should increase with the addition of inclusions and more likely at the next observed strain frame.

Subgroup Atii, illustrates many more light regions within the bainite, revealing more plasticity occurring. This is due to the increase in ceramics as described earlier in more detail. The highest plasticity is again throughout the ferrite, which has become much lighter, exhibiting higher PEEQ values still with the same range as Subgroup Ati,

but indicating more regions closer to 1.333 and more strain concentration branches. The maximum PEEQ for this subgroup has also increased to a value of about 4.1 for all the RVE groups.

Subgroup Atiii at 80% shows a slight increase in maximum PEEQ from the previous subgroup of about 4.2. Although the maximum PEEQ did not increase by much, this may be explained by the large increase in PEEQ distribution amongst the rest of the regions in the microstructures. Although the ceramic particles show no PEEQ response, the martensite shows more evidence of PEEQ still ranging from 0 to 0.667, yet now there are more light regions visible. Also, the bainite seems to have increased its range of plasticity to 0.333 to 1.0. As predicted the ferrite also illustrates more branches of very high PEEQ concentrations. In visual terms, these branches now include much more red than previous observed strain levels.

To improve on the analysis done at 80% strain, the next most critical frame is observed at 100% strain for each microstructure in Figures 71 - 73.

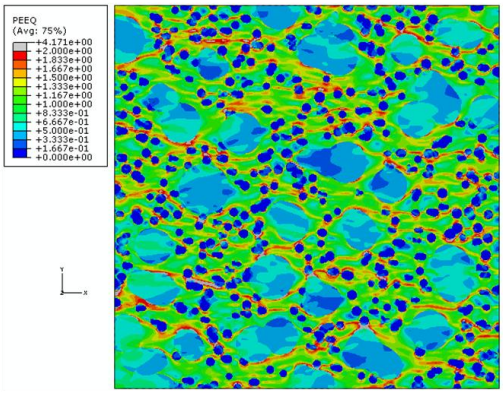

Group 1: At

Subgroup Ati

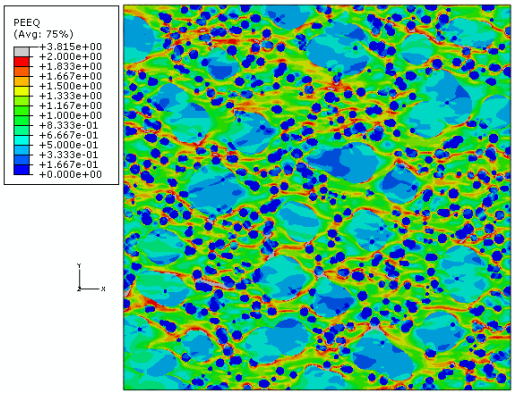

Group 2: Silicon Carbide

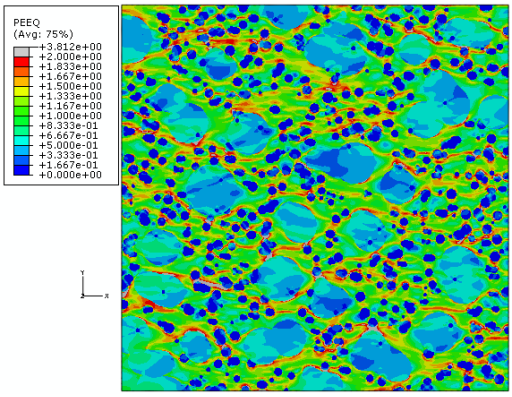

Group 3: Cementite

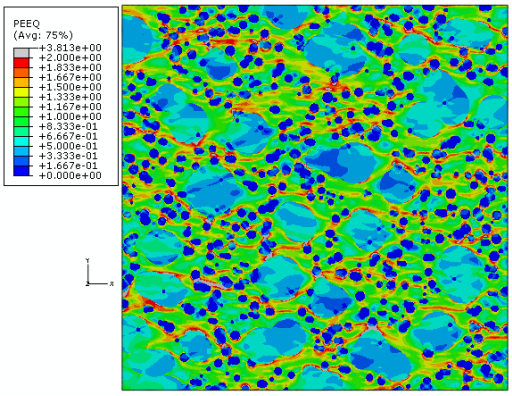

Group 4: Zirconia

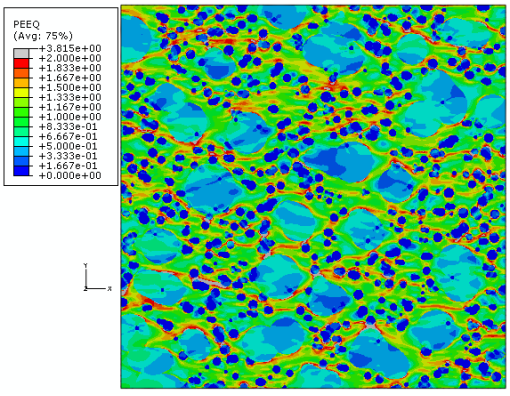

Group 5: Aluminum

Figure 71 PEEQ for Group 1 and Subgroup Ati at 100% strain

Subgroup Atii

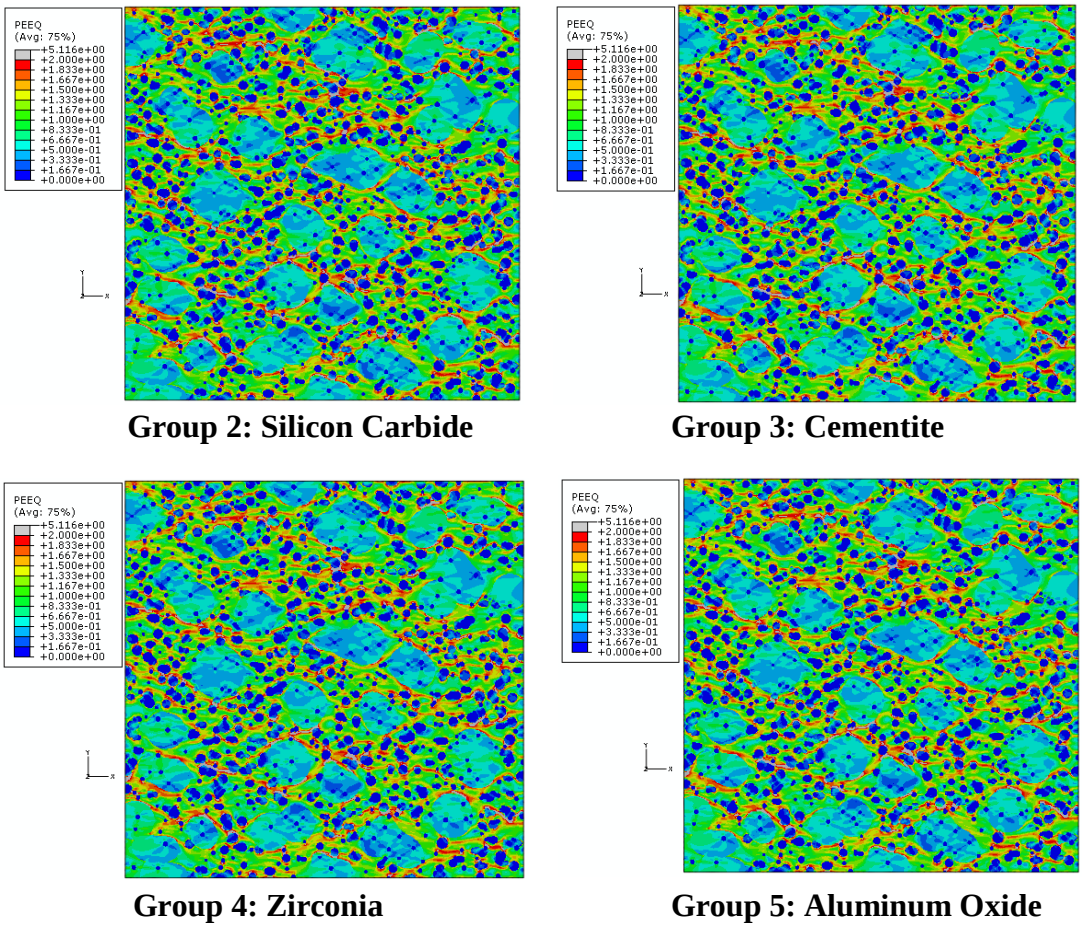

Figure 72 PEEQ for Subgroup Atii at 100% strain

Subgroup Atiii

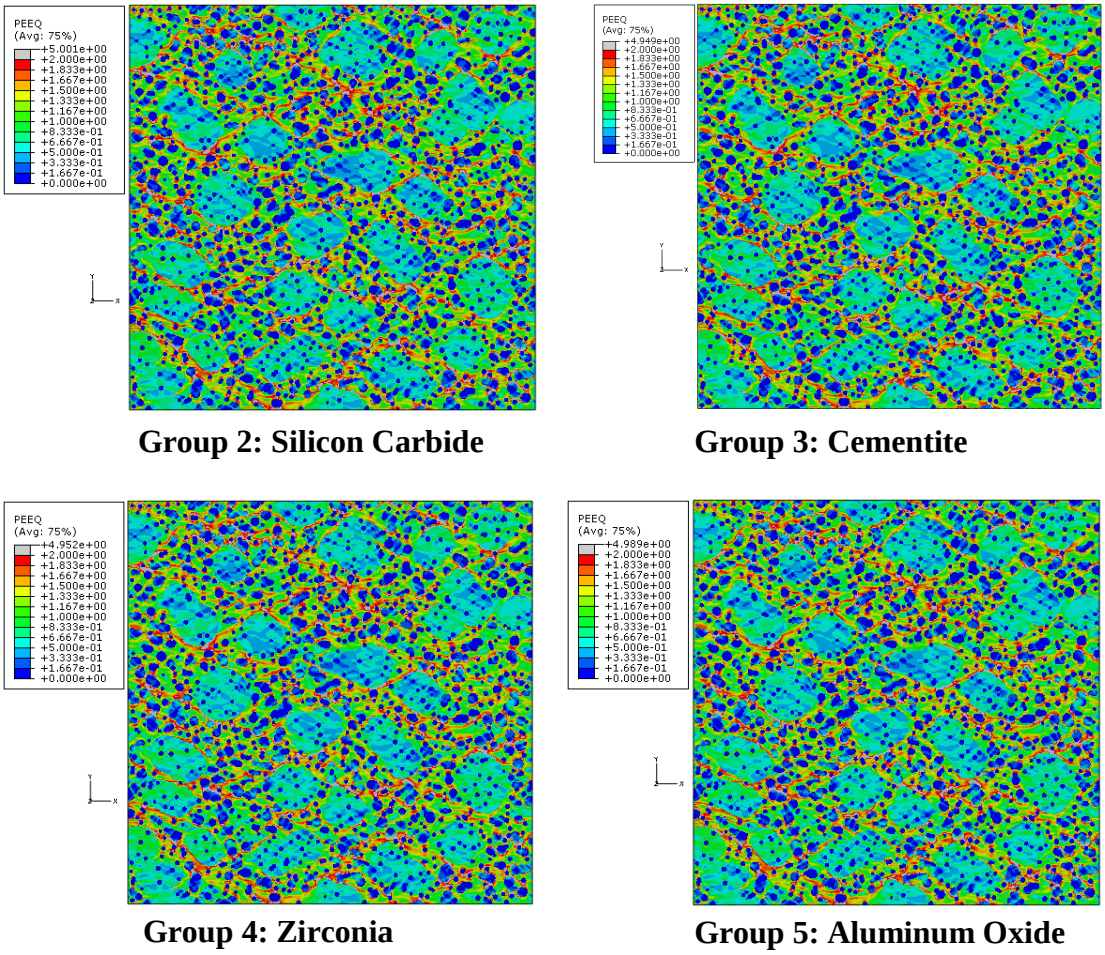

Group 2: Silicon Carbide **Group 3: Cementite**

Group 4: Zirconia **Group 5: Aluminum Oxide**

Figure 73 PEEQ for Subgroup Atiii at 100% strain

To reiterate, at 100% strain, structure At in Group 1 illustrates more severe PEEQ levels throughout the branches spreading through the microstructure. These areas now illustrate areas of red and orange, even some areas of gray illustrating regions of maximum PEEQ values of 4.171. These branches never pass through a bainite or martensite constituent, they merely move around the interface of the constituents. This

illustrates that in the control, cleavage fracture inside a bainite or martensite island will not be the leading cause of failure. The main PEEQ vulnerable areas engender among the martensitic interfaces and later the bainite islands. They connect and spread through the ferrite, suggesting the possibility of fracture caused through strain in the ferrite. The bainite islands do show a higher PEEQ ranging from 0.1667 to 1.167. The bainite phases are illustrating the same lower PEEQ values in some regions as the ferrite. The martensite phases at this stage also illustrate areas of PEEQ ranging from 0 to 0.667.

Subgroup Ati, as before illustrates a lower maximum PEEQ throughout the microstructures compared to Group 1 of about 3.8. As predicted, Groups 2-5 are similar enough to again assume ceramic material utilized is negligible. As predicted the overall material behavior of the microstructures in Subgroup Ati are similar to At in overall PEEQ range values, except some regions have become lighter within the bainite due to the introduction of ceramics in the microstructure. Even the plasticity in the martensite and ferrite seem to increase very slightly, yet the overall PEEQ behavior is very similar to At. This is much more prevalent in the next few subgroups as ceramics are added.

Subgroup Atii on the other hand, illustrates a maximum PEEQ of about 5.116 for all group microstructures. Compared to Subgroup Atiii, with a maximum PEEQ of about 5.0 for all the microstructures within the subgroup, Atii illustrates a higher maximum PEEQ since the martensite, bainite and ferrite continuants seem to be absorbing much of the localized strain. The microstructures presented in Subgroup Atiii do no illustrate the highest maximum PEEQ values, but the phases throughout show evidence of higher PEEQ values than the other subgroups. The PEEQ ranges described for the previous

subgroups are the same for each constituent, except now in this subgroup, the PEEQ values are much closer to the higher end of the identified spectrums. Also, more frequent lighter areas are evident throughout the martensitic and bainite structures. The ferrite matrix is now mainly covered in red and orange branches with significant areas of gray, illustrating extremely high PEEQ values that simulate the areas in which cracks will undoubtedly penetrate through the microstructure. As described before, the martensitic properties govern over the ceramic material properties presented in each group. None the less, the slight difference in Subgroup Atiii still follows the same sequence as Subgroup Aiii in which the harder ceramic material illustrates a higher maximum PEEQ value throughout the microstructure. Group 2-Silicon Carbide illustrates a maximum PEEQ of 5.00 followed by Group 5-Aluminum Oxide with 4.989, Group 4- Zirconia with 4.952 and finally Group 3-Cementite with 4.949. This difference in maximum PEEQ throughout the groups, though, is so small that for the martensitic structures, ceramic material properties are overtaken by the properties presented by martensite. The deformed microstructures at 100% strain are illustrated below in Figures 74 - 76 to further depict how the cracks will proliferate through the structures upon loading.

Subgroup Ati

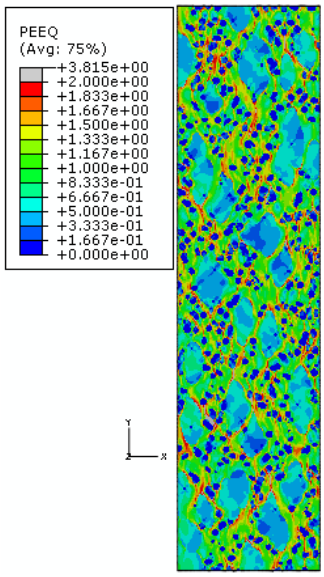

Group 2: Silicon Carbide

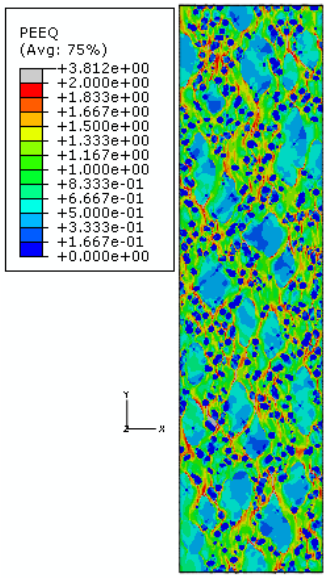

Group 3: Cementite

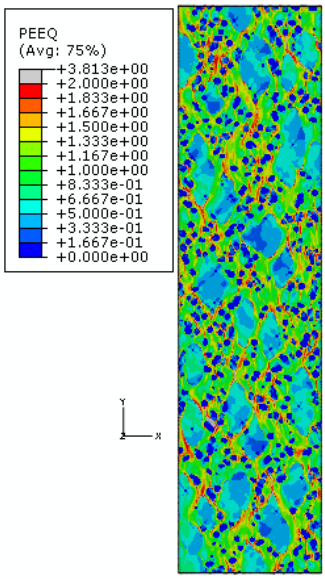

Group 4: Zirconia

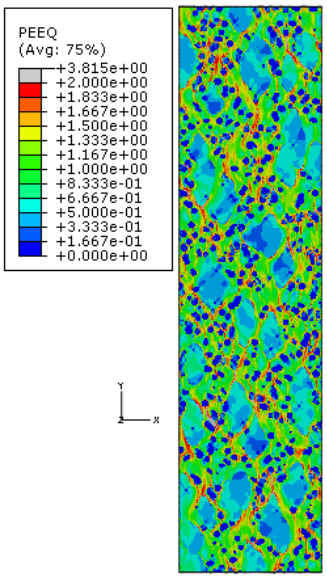

Group 5: Aluminum Oxide

Figure 74 PEEQ for Subgroup Ati at 100% strain-deformed microstructure

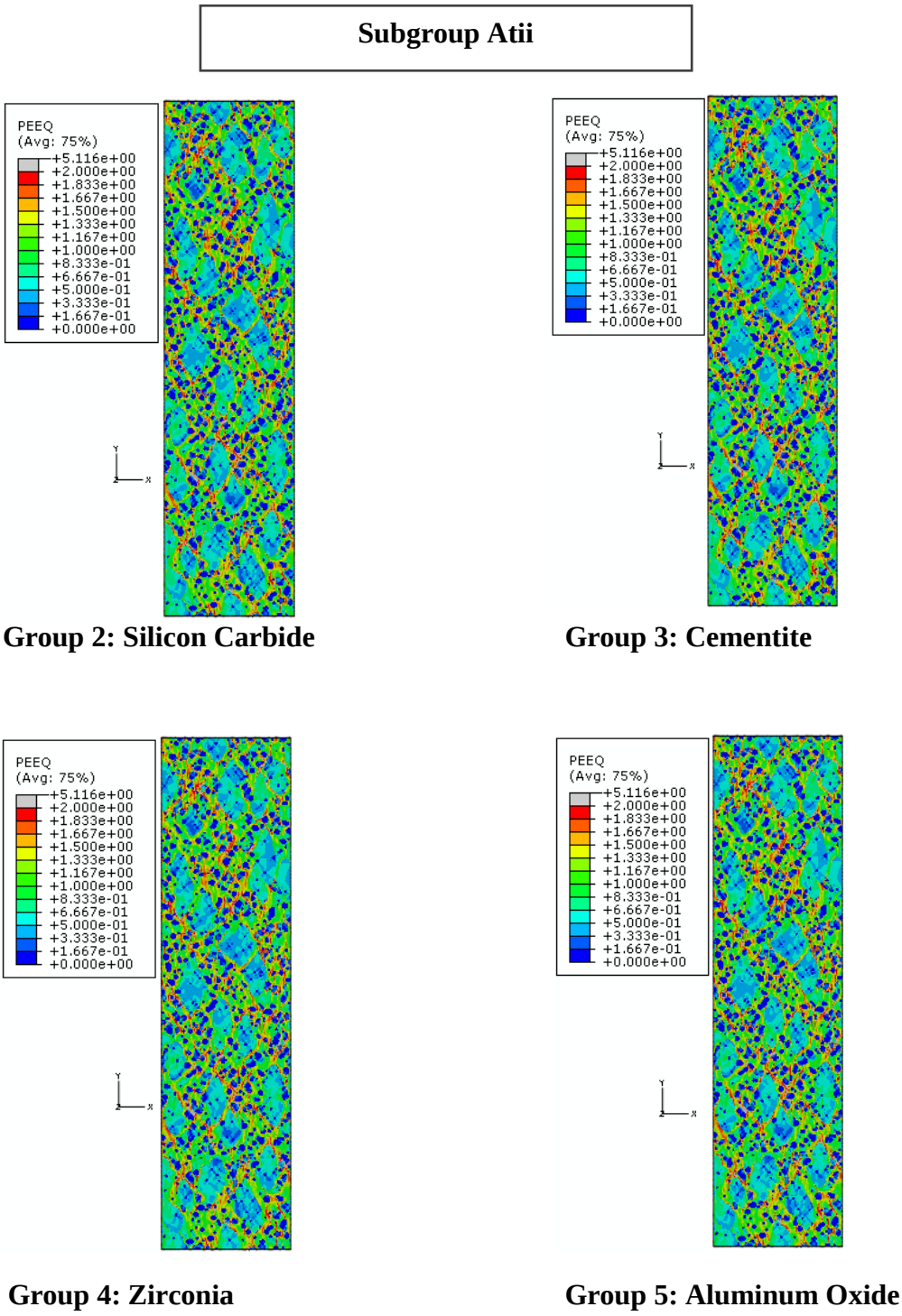

Figure 75 PEEQ for Subgroup Atii at 100% strain-deformed microstructure

Subgroup Atiii

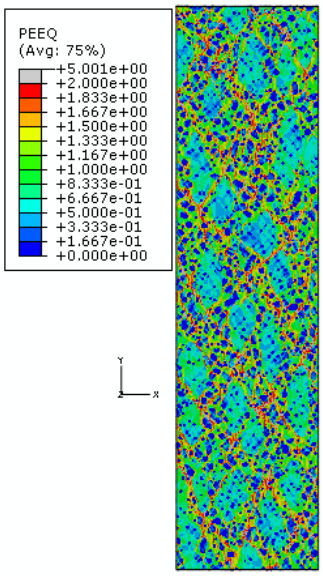

Group 2: Silicon Carbide

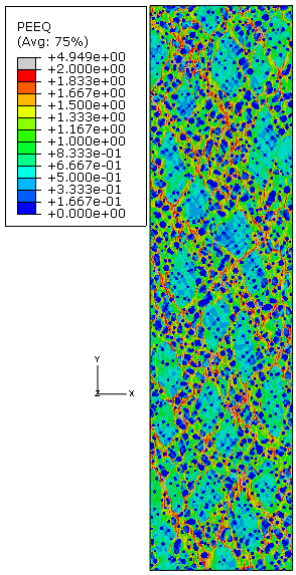

Group 3: Cementite

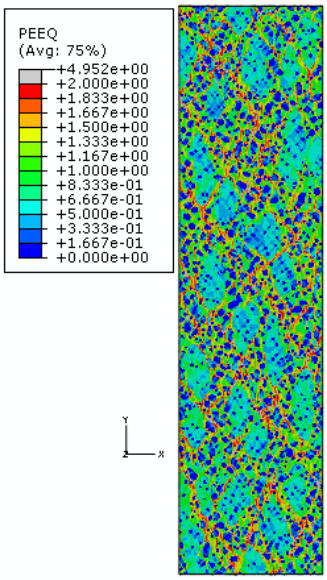

Group 4: Zirconia

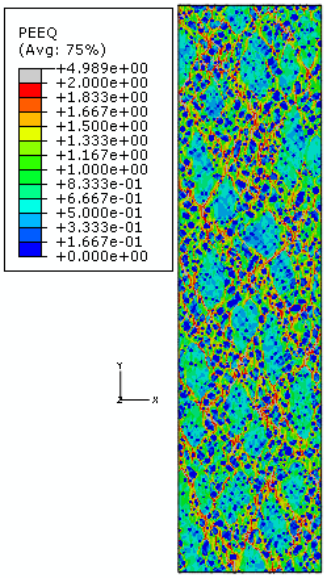

Group 5: Aluminum Oxide

Figure 76 PEEQ for Subgroup Atiii at 100% strain-deformed microstructure

The behavior of the all the microstructures in Groups 2, 3, 4, and 5 are congruent to the main behavior illustrated in Group 1 in which the martensitic structures illustrate more and larger values of strain localizations than the austenitic structures. From the frames in the ceramic inclusion groups, it is also evident that more strain localization and larger values of strain localizations occur the majority of the time in the structures with higher percentage volumes of ceramics. As demonstrated in Group 1 with the martensite, this is due to the paramount difference in modulus between the extremely hard ceramic and soft ferrite matrix, as well as the other constituents in the microstructure. These localizations occur at a faster rate as the ceramic content in the microstructure increases. Also, these strain localizations occur much sooner in the transformed phases and also with the microstructures with larger percentages of ceramic inclusions since the martensite controls most of the PEEQ behavior. Due to this, the highest strain localization and strain values occur in Subgroup Atiii, which consists of the transformed structure with 10% ceramic inclusions. Also congruous to Group 1, the PEEQ distribution and behavior suggests that failure in the austenitic structures occur as a result of strain localization throughout the ferrite. The strain bands in the ferrite actually serve as hindering agents that keep the “voids” along the constituent and particle interfaces from growing. Yet, as more ceramic inclusions are added to the microstructure, and more areas of large strain localization occur in the interfaces of the inclusions, the composite becomes more vulnerable to failure due to voiding and crack propagation. The martensitic structures on the other hand all propose more likeliness of

failure due to voids initiating at the interfaces and coalescing to create a crack, ultimately ending in fracture.

4.3 Stress vs. Strain Behavior Group 2- TRIP Steel With Silicon Carbide Inclusions

The next paramount factor that must be analyzed in order to view the behavior of the material is the stress versus strain response of each RVE. Each ceramic material group will be analyzed separately in order to observe the direct effects of changing the ceramic volume fraction in each microstructure. After this, the groups will then be compared with each other to conclude which material illustrates the most optimal results and how varying the ceramic material presented in each microstructure truly effects the total behavior of the composite.

First, Group 2 which entails silicon carbide inclusions is analyzed, recorded, and compared. Thus, the response of each volume subgroup is recorded, plotted, and compared to the other microstructures within Group 2. These mentioned microstructures in Group 2 yielded the stress vs. strain responses in Figure 77 with composite properties calculated in Table 11.

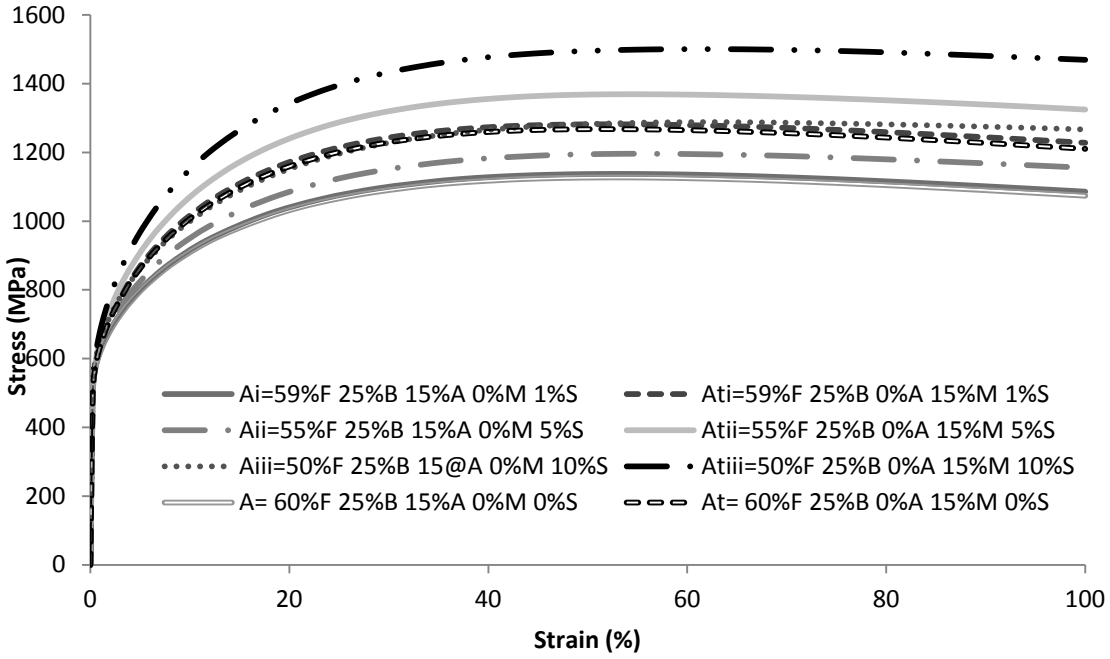

Figure 77 Group 1 and Group 2 stress vs. strain response

Table 11 Resulting properties for Group 2 particle reinforced TRIP steel composite microstructures

Subgroup	E (MPa)	σ_y (MPa)	σ_u (MPa)	$\%\varepsilon_u$ (μm/μm)
Ai	238627.5	477.255	1137.72	52.8196
Ati	238616.8	477.2336	1282.194	52.1822
Aii	207083.2	414.1664	1196.018	54.4526
Atii	207092.8	414.1856	1368.996	54.4896
Aiii	210848.8	421.6976	1288.356	61.6192
Atiii	210901.6	421.8032	1500.334	61.5356

As in Group 1, the transformed microstructures in Group 2 illustrate a stronger behavior than that of the TRIP steel microstructures with retained austenite. This can be further supported in Table 11, where the ultimate tensile strength for the transformed microstructures is much higher than their preliminary stage counterparts. Also, more importantly, the stress vs. strain behavior indicates that as the volume content of silicon carbide particles increase within the microstructure, so does the overall capacity of the composite. The stress vs. strain responses illustrate a higher strength as the presence of silicon carbide particles increase for both the initial and transformed phases. The more dramatic the increase of silicon carbide particles, the higher the capacity of the composite becomes on the stress vs. strain diagram. For example, if we focus on Subgroup Ai and Ati in comparison to Group 1's microstructures A and At respectively, the difference in capacity by just adding 1% inclusions into the microstructure is slight, but noticeable. On the other hand, by adding in 5% ceramic inclusions illustrate an even greater increase in capacity. This increase is even more dramatic when the silicon carbide volume content is increased to 10%. Table 11 illustrates the values of the ultimate tensile strength to further support this increase in strength with the addition of ceramic inclusions. This comparison will be illustrated in more detail momentarily. The ductility for each microstructure also seems to increase proportionally to the increasing volume of silicon carbide particles as described in the PEEQ analysis. The microstructures containing the highest silicon carbide content in Subgroup Aiii and Atiii exhibit the highest strain at ultimate strength in Group 2 with strain values of 61.62% and 61.54%. Of these two, Subgroup Aiii, the austenitic structure illustrates the superior

ductility, although it is not much of an increase from its transformed structure. Naturally, due to the inevitable transformation into a harder phase, microstructure Atiii will lose a small fraction of ductility. Again, this difference is so small that the overall performance of the microstructure is not considered compromised. The modulus of elasticity and yield strength on the other hand, had a very small and almost negligible increase to the composite's transformed stage, yet marked odd differences between subgroups with different volume fractions of silicon carbide particles. In order to simply summarize the increase or decrease in properties from the corresponding control TRIP steel microstructure, Table 12 entails this information in a concise manner.

Table 12 Percent difference from Group 1

	% Increase From Group I			
Subgroup	**E (MPa)**	**σ_y (MPa)**	**σ_u (MPa)**	**$\%\varepsilon_u$ (μm/μm)**
Ai	17.23495	17.23495	0.917708	-0.5462
Ati	17.22921	17.22921	1.106962	0.4538
Aii	1.737589	1.737589	6.08884	1.0868
Atii	1.741906	1.741906	7.951703	2.7612
Aiii	3.587585	3.587585	14.27938	8.2534
Atiii	3.613118	3.613118	18.30832	9.8072

Overall, as predicted, compared to Group 1, the particle reinforced TRIP steel composites in Group 2 achieve a higher tensile strength due to the hard elastic ceramic inclusions, especially as more inclusions were introduced into the microstructure.

Strength increased in Subgroup Ai , Aii, and Aiii by 0.92%, 6.09% and 14.28% respectively compared to the initial TRIP steel microstructure in Group 1 with no inclusions. Subgroup Ati, Atii and Atiii experienced a much higher increase of strength that their austenitic counterparts of 1.11%, 8.00%, and 18.31% respectively from the original transformed microstructure, At. As in Group 1, the higher strength in the transformed stage is due to the presence of martensite instead of austenite. Besides the small outlier illustrated by Subgroup Ai, the elongation or percent strain also gradually increases proportionally with the volume content of silicon carbide inclusions. Although the austenitic structure with 1% increase in ceramic inclusions illustrates a 0.55% decrease in ductility in comparison to Group 1, the other two austenitic structures with higher contents of ceramic particles show a 1.09% and 8.25% increase in strain for 5% and 10% silicon carbide inclusions respectively. The largest increase in ceramic inclusions illustrates the highest increase in ductility from the original austenitic unreinforced structure. This also holds true for the transformed structures which increase by 0.45%, 2.76%, and 9.81% in strain from microstructure At with increasing volumes of silicon carbide inclusions. The modulus of elasticity and initial yield strength for the reinforced TRIP steel composites illustrate diverse increases from the original structure of 17.23%, 1.74%, 3.59% for Subgroup Ai, Aii, and Aiii and similarly, for the transformed versions in Subgroups Ati, Atii and Atiii, increases of 17.23%, 1.74%, and 3.61% respectively. Now, in order to compare the difference amongst the subgroups, Table 13 summarizes the percent differences in properties within Group 2.

Table 13 Percent difference between subgroups in Group 2

Subgroup	E (MPa)	σ_y (MPa)	σ_u (MPa)	$\%\varepsilon_u$ (μm/μm)
Ai->Aii	-13.2191	-13.2191	5.124108	1.633
Ati-> Atii	-13.2111	-13.2111	6.769802	2.3074
Ai->Aiii	-11.641	-11.641	13.24016	8.7996
Ati-> Atiii	-11.6149	-11.6149	17.01303	9.3534
Aii->Aiii	1.8184	1.8184	7.720452	7.1666
Atii->Atiii	1.839175	1.839175	9.593746	7.046

From these results, it is evident that the addition of silicon carbide particles into TRIP steel does in fact increase the overall strength and ductility of the microstructure. For example, the ultimate strength increased by a total of 17.01% and strain at ultimate increased by a total of 9.35% just from comparing microstructure Ati to microstructure Atii, or a total increase of 9% more volume content of silicon carbide inclusions. From Table 13, it can be inferred that adding inclusions does in fact enhance the performance in strength and ductility of TRIP steel. Yet, this enhancement does not compliment the modulus of elasticity and initial yield strength of the material, except in the cases in Table 13 when subgroup Atii is compared to Atiii. Compared to the high 13.2% and 11.6% decrease in Young's modulus and yield strength for Ai/Ati vs. Aii/Atii and Ai/Ati vs. Aiii/Atiii , the slight 1.8% increase from Subgroup Aii/Atii to Aiii/Atiii proves to be ineffective. The addition of ceramic inclusions is highly responsible for this large

decrease in modulus of elasticity and yield strength. Adding in more of a harder ceramic material will cause the material itself to become harder, thus decreasing the modulus of elasticity and also causing it to yield at an earlier strength. Therefore from this study, in Group 2, microstructures Aiii and Atiii which indicate the beginning and final stages of transformation of a particle reinforced TRIP steel composite with a 10% volume content of silicon carbide particles, indicates the highest enhancement of strength and ductility.

4.3 Stress vs. Strain Behavior Group 3- TRIP Steel With Cementite Inclusions

Group 3 entails the same explained microstructures with cementite as the ceramic material utilized for the inclusions. To be more clear, the exact same microstructures presented in Group 2 are analyzed in Group 3, yet the only difference is that instead of utilizing silicon carbide for the material in the ceramics, cementite is used. The following Figure 78 and Table 14 illustrate the behavior recorded for this particular group.

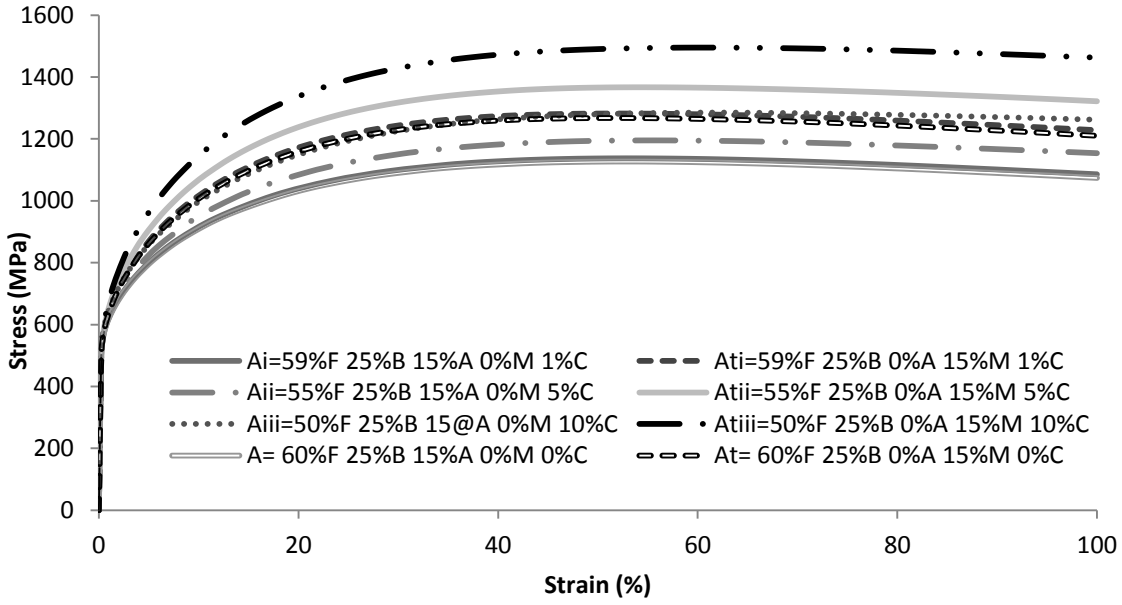

Figure 78 Group 1 and Group 3 stress vs. strain response

Group 3 illustrates the same overall behavior as in Group 2 in which the martensitic structures exhibit higher strengths compared to their austenitic counterparts. Also, the overall enhancement in behavior due to the inclusion and increase in cementite particles in the TRIP steel microstructure is also synonymous in Group 3 as it was in Group 2. The enhancement in the overall capacity of the cementite reinforced TRIP steel composite as in Group 2 also depends in Group 3 on the total increase in volume fraction of the cementite particles introduced into the microstructure. Table 14 illustrates these enhanced values more closely.

Table 14 Resulting properties for Group 3 particle reinforced TRIP steel composite microstructures

Subgroup	E (MPa)	σ_y (MPa)	σ_u (MPa)	$\%\varepsilon_u$ (μm/μm)
Ai	238153.8	476.3076	1137.59	52.8196
Ati	238046.6	476.0933	1281.966	51.5606
Aii	204276.8	408.5536	1195.108	55.8736
Atii	204276.8	408.5536	1367.352	54.1682
Aiii	205110.4	410.2208	1285.658	61.338
Atiii	205110.4	410.2208	1495.816	60.0738

As in the previous group, Group 3 also proves that the highest ductility and ultimate tensile stress occurs in the TRIP steel microstructure containing the 10% volume fraction of ceramic particles. Subgroup Aiii and Atiii show that the strain at ultimate strength is 61.34% and 60.07%. The transformed structure, again, is slightly less ductile than that of its original austenitic structure, yet this follows the same explanation in which the martensitic phase introduces a harder material. This difference is so small, that the difference is almost negligible, especially since the Atiii still illustrates a higher strain at ultimate value than the remaining subgroup microstructures in Group 3. The ultimate strength is also the highest in Subgroup Atiii with a value of 1495.816MPa. Also synonymous to Group 2, the modulus of elasticity and yield strength illustrate the same odd behavior between subgroups. Despite the similarities between the overall behavior of Group 2 and Group 3, these increases in performance are not as large in magnitude as in Group 2. For example, Group 2 illustrated an ultimate tensile strength of 1500.33MPa for Atiii versus the same microstructure in Group 3 with 1495.82MPa. Also, the strain at

ultimate for Aiii/Atiii for Group 3, 61.34% / 60.07%, are less than Group 2, 61.62% / 61.54%. Although this difference is small in both cases, it is important to note that Group 3 does not illustrate as high of an improvement in performance as Group 2. This can also be seen in Table 15 which shows the comparisons in Group 3 from the original control group.

Table 15 Percent difference from Group 1

	% Increase From Group I			
Subgroup	**E (MPa)**	**σ_y (MPa)**	**σ_u (MPa)**	**$\%\varepsilon_u$ (μm/μm)**
Ai	17.00222	17.00222	0.906177	-0.5462
Ati	16.94911	16.94911	1.088983	-0.1678
Aii	0.358837	0.358837	6.008122	2.5078
Atii	0.358443	0.358443	7.822066	2.4398
Aiii	0.768375	0.768375	14.04006	7.9722
Atiii	0.767979	0.767979	17.95205	8.3454

As discussed, Group 3 illustrates higher tensile strengths compared to Group 1. Strength increased in Subgroup Ai, Aii, and Aiii by 0.91%, 6.01% and 14.04% respectively compared to the initial TRIP steel microstructure. Subgroup Ati, Atii and Atiii yield an increase of strength of 1.09%, 7.82%, and 17.95% respectively from the original transformed microstructure, At. These enhancements are very close in value to those recorded with silicon carbide inclusions. It is important to note also, that silicon carbide

and cementite are the two extremes in this experiment, thus they should illustrate the two extreme performances of this study. For example, silicon carbide has the highest value of modulus of elasticity in this study while cementite offers the lowest. Therefore, their responses should indicate the highest and lowest behavior for the particle reinforced TRIP steel composites. Ironically, although a slight difference is shown, the enhancement due to the ceramic material does not seem very drastic. To further support this, similar to Group 2, compared to the control group, Subgroup Ai and Ati illustrate a very small compromise in ductility. By adding in 1% cementite inclusions into the microstructure, there is a 0.55% decrease of strain in the austenite structure and 0.17% decrease in strain in the martensite structure. The remaining microstructures Aii/Atii and Aiii/Atiii illustrate an increase in strain due to addition of inclusions of 2.51% / 2.44% and 7.97% / 8.35%. Subgroup Aii in Group 3 is the only structure that illustrates a higher enhancement in ultimate strain than Group 2 which only shows a total enhancement of 1.09%. More clearly, Group 3 Subgroup Aii illustrates that strain at ultimate stress is 55.87% while Group 2 Subgroup Aii shows the strain to be 54.45%. Unfortunately, this only holds true for this structure, which is not the optimal solution for this study. Also, the overall behavior of Group 3 is similar to Group 2 for the change in modulus of elasticity and yield strength. An increase is shown from the original structures for all microstructures, although the increase ranges among subgroups. The values of these parameters compared amongst the subgroups in Group 3 are noted below in Table 16 for a closer comparison.

Table 16 Percent difference between subgroups in Group 3

Subgroup	E (MPa)	σ_y (MPa)	σ_u (MPa)	$\%\varepsilon_u$ (μm/μm)
Ai->Aii	-14.2248	-14.2248	5.056127	3.054
Ati-> Atii	-15.1495	-15.1495	6.660551	2.6076
Ai->Aiii	-13.8748	-13.8748	13.01594	8.5184
Ati-> Atiii	-14.8032	-14.8032	16.68141	8.5132
Aii->Aiii	0.408074	0.408074	7.576721	5.4644
Atii->Atiii	0.408074	0.408074	9.395094	5.9056

From Table 16, the same conclusion is made as before in that the addition of cementite inclusions increases the ductility and strength of a TRIP steel microstructure. Although the modulus of elasticity and yield strength illustrate an overall increase from Group 1 when inclusions are presented, the amount of cementite particles play a large role in how the microstructure will respond. Group 2 also exhibited the same pattern in which 1% ceramic inclusions illustrated the higher increase in modulus of elasticity and yield strength, followed by 10% and then 5% volume addition. This indicates that the addition of 1% volume of ceramics into a TRIP microstructure will allow the composite to achieve a much higher modulus of elasticity and also allow it to yield at a much higher stress, thus causing the material to initially become much harder than the initial phase. Unfortunately, when 5% volume of ceramics are added, although more hard inclusions are introduced into the microstructure, the composite actually behaves as a softer

material. This may be tied into the previous observations in the PEEQ analysis in which more inclusions allow for more areas in the ferrite to become vulnerable about the interfaces. Thus the soft ferrite matrix surrounding the inclusions absorb more of the stress imposed upon the microstructure, causing the composite as a whole to yield at an earlier stress, and not show as high of a modulus of elasticity. Yet, when a 10% volume fraction of ceramic inclusions are included in a TRIP steel microstructure, these parameters begin to increase again, describing a harder, tougher material. The way to explain this factor is that at 5% ceramic volume fraction, the ferrite and softer phases in the TRIP steel gain control of the composites overall elastic properties, while if a 10% ceramic volume fraction is introduced, the amount of ceramic inclusions deter the other constituents to control the elastic region, thus yielding these results. At 1% ceramic volume fraction, the presence of the small amount of ceramics into the microstructure are not enough to focus the stress on the softer phases in the microstructure, thus these ceramic inclusions act as stress concentrations to help the microstructure achieve such a higher yield stress and elastic modulus.

4.4 Stress vs. Strain Behavior Group 4- TRIP Steel With Zirconia Inclusions

Group 4 now entails the addition of zirconia inclusion into the microstructure. Since the elastic properties of zirconia are so close and similar to those of cementite, the results for Group 4 are predicted to be very similar to those of Group 3. Therefore, in order to avoid too much repetition or reiteration, Group 4 will not be described as in

large detail as the previous two groups. With this in mind, Figure 79 illustrates the stress vs. strain response for Group 4 and Table 17 tabulates the proper calculated properties.

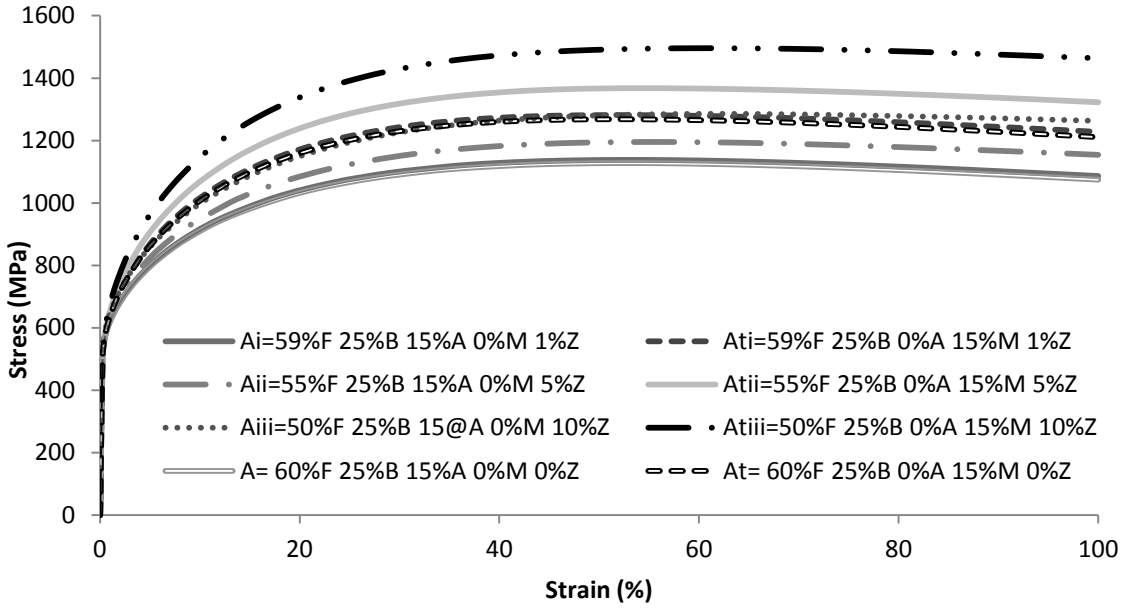

Figure 79 Group 1 and Group 4 stress vs. strain response

Table 17 Resulting properties for Group 4 particle reinforced TRIP steel composite microstructures

Subgroup	E (MPa)	σ_y (MPa)	σ_u (MPa)	$\%\varepsilon_u$ (μm/μm)
Ai	238297.8	476.5956	1137.606	52.8196
Ati	238297.8	476.5956	1281.994	51.5606
Aii	204606.4	409.2128	1195.188	56.3892
Atii	204606.4	409.2128	1367.536	54.1682
Aiii	205808.8	411.6176	1285.77	61.0488
Atiii	205808.8	411.6176	1496.332	60.7872

As predicted, the values for the parameters calculated and the graphed behavior for Group 4 proves to be extremely similar to that of Group 3, yet slightly higher. The performance in ultimate strength and strain at this point is still increasing with the addition of inclusions. Subgroup Atiii reveals the highest ultimate stress of 1496.33MPa at 60.79% strain. It's austenitic structure, Aiii, before transformation illustrates a strain at ultimate of 61.05%, which proves to be the highest strain at ultimate in Group 4. Therefore, for this study, the most optimal case to enhance strength and ductility in the particle reinforced TRIP steel composite entails Subgroups Aiii and Atiii with 10% volume fraction of ceramic inclusions. Also, the modulus of elasticity and yield strength are also very close in value, yet slightly larger than Group 3. Since zirconia is a slightly harder phase, this explains the slight increase in properties resulting from the cementite particles. The variation from Group 1 can be investigated in Table 18 while Table 19 provides insight on the differences between the subgroups.

Table 18 Percent difference from Group 1

	% Increase From Group I			
Subgroup	**E (MPa)**	**σ_y (MPa)**	**σ_u (MPa)**	**$\%\varepsilon_u$ (μm/μm)**
Ai	17.07296	17.07296	0.907596	-0.5462
Ati	17.0725	17.0725	1.091191	-0.1678
Aii	0.520766	0.520766	6.015218	3.0234
Atii	0.520371	0.520371	7.836575	2.4398
Aiii	1.111491	1.111491	14.05	7.683
Atiii	1.111094	1.111094	17.99274	9.0588

Table 19 Percent difference between subgroups in Group 4

Subgroup	E (MPa)	σ_y (MPa)	σ_u (MPa)	$\%\varepsilon_u$ (μm/μm)
Ai->Aii	-14.1384	-14.1384	5.061682	3.5696
Ati-> Atii	-14.1384	-14.1384	6.672574	2.6076
Ai->Aiii	-13.6338	-13.6338	13.02419	8.2292
Ati-> Atiii	-13.6338	-13.6338	16.71911	9.2266
Aii->Aiii	0.587665	0.587665	7.578891	4.6596
Atii->Atiii	0.587665	0.587665	9.418107	6.619

Congruent to the previous groups, an overall increase can be seen from Table 18 in all properties, excluding the two outliers illustrated in the small ductility decrease in Subgroup Ai and Ati by 0.55% and 0.17% strain respectively from the corresponding structures in Group 1. As mentioned previously, these two factors are so small, that the overall conclusion of ductility enhancement due to addition of ceramic inclusions is not compromised. Also, with the more inclusions provided into the microstructure, the larger the strain increase at ultimate stress, thus eliminating any doubts insisted by the mentioned outliers. For example, an increase of 3.02% / 2.44% and 7.68% / 9.06% in strain for Subgroups Aii/Atii and Aiii/Atiii are enough proof to disregard the negligible decrease in ductility suggested by Subgroup Ai/Ati. To further illustrate the enhancement in strength due to addition and the increase in ceramic particle volume fraction, the addition of zirconia into each microstructure compared to Group 1 increased the ultimate tensile strength by 0.91%, 6.02%, and 14.05% in Subgroups Ai, Aii, and Aiii, and by 1.09%, 7.84%, and 18.0% in Subgroups Ati, Atii, and Atiii. The predicted

trend in which a higher volume fraction of ceramic inclusions enhanced the strength is still supported with the zirconia particles. Table 19 also illustrates this fact by illustrating that as the content of zirconia particles increase, so does the percentage increase in ultimate strength and even ductility. For example, from Ati to Atiii, the overall strength is increased by 16.72% and the strain at this point also increases by 9.23%. The modulus of elasticity and yield strength also follows the same behavior as described in Group 3. Overall increases from the original structure in Group 1 are seen for all microstructures, in the same previously described pattern. Yet, as before, between subgroups, decreases of 14.14% and 13.63% are witnessed between Subgroups Ai/Ati and Aii/Atii, and Ai/Ati and Aiii/Atiii, while a very small increase of 0.59% is seen between Aii/Atii and Aiii/Atiii.

4.5 Stress vs. Strain Behavior Group 5- TRIP Steel With Aluminum Oxide

Finally, the last group, Group 5 entails the addition of inclusions consisting of aluminum oxide. This material serves as a median between Group 2 and Groups 3 and 4 since this material is harder than cementite and zirconia, but not as hard as silicon carbide. Therefore, parameters and behavior of this group is responsible for reporting the median response as opposed to the extremes described primarily by Groups 2 and 3. Therefore, Figure 80 illustrates the material response for each microstructure in Group 5 with the calculated parameters in Table 20.

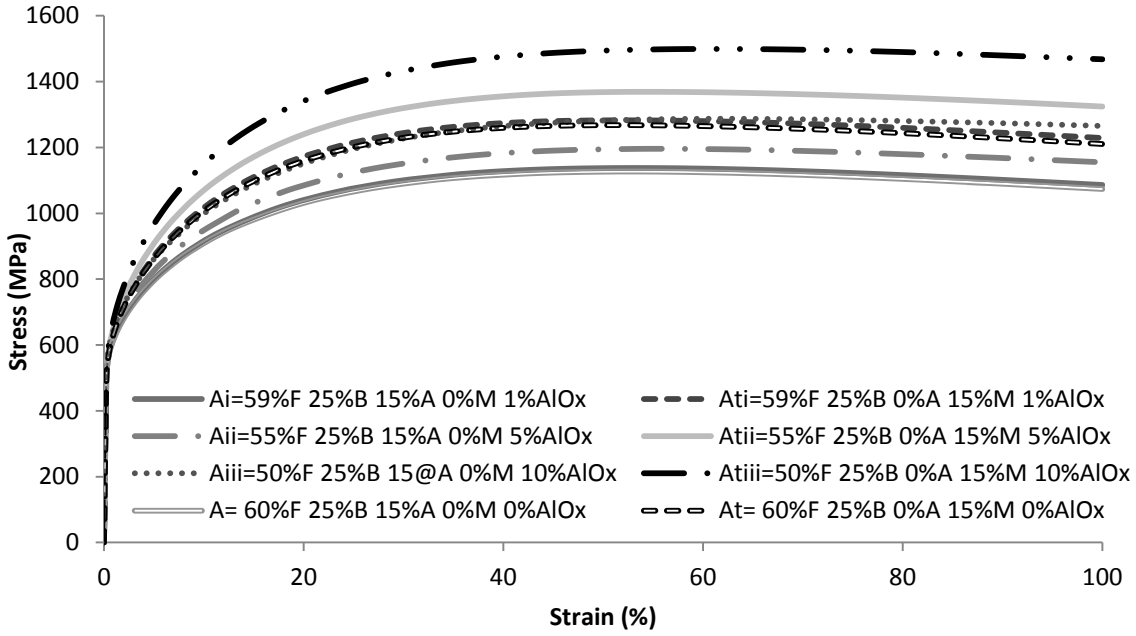

Figure 80 Group 1 and Group 5 stress vs. strain response

Table 20 Resulting properties for Group 5 particle reinforced TRIP steel composite microstructures

Subgroup	E (MPa)	σ_y (MPa)	σ_u (MPa)	$\%\varepsilon_u$ (μm/μm)
Ai	238499.4	476.9988	1137.698	52.8196
Ati	238606.8	477.2136	1282.14	52.4708
Aii	206620.8	413.2416	1195.946	55.5254
Atii	206624.8	413.2496	1368.656	54.8554
Aiii	209947.2	419.8944	1287.836	62.6938
Atiii	209971.2	419.9424	1499.45	61.8124

The most paramount parameter calculated in Group 5, which was also revealed in the PEEQ analysis is the strain at ultimate strength for Subgroup Aiii, 62.69%, which illustrates the highest strain at ultimate out of all the groups and subgroups. Its transformed configuration, Atiii, shows the second highest strain value at ultimate of 61.81%. The highest ultimate tensile strength, 1499.45MPa, is also revealed in Subgroup Atiii for Group 5. This value is only slightly less than silicon carbide which illustrates the highest value of ultimate strength of 1500.33MPa. Ductility on the other hand, is higher for Group 5 in Subgroup Aiii by a little more than 1% compared to silicon carbide. Group 2 illustrates strain values at ultimate in Subgroups Aiii/Atiii of 61.62% / 61.54%. Therefore, aluminum oxide illustrates an even greater enhancement than silicon carbide in ductility, and is very competitive in ultimate strength. Despite this, the modulus of elasticity and yield strength for each microstructure in Group 5 is still less than those in Group 2, yet larger than Group 3 and Group 4. Table 21 and Table 22 also show the variation from Group 1 and the subgroups within Group 5.

Table 21 Percent difference from Group 1

	% Increase From Group I			
Subgroup	**E (MPa)**	**σ_y (MPa)**	**σ_u (MPa)**	**$\%\varepsilon_u$ (μm/μm)**
Ai	17.17201	17.17201	0.915756	-0.5462
Ati	17.2243	17.2243	1.102703	0.7424
Aii	1.510417	1.510417	6.082454	2.1596
Atii	1.511983	1.511983	7.924893	3.127
Aiii	3.144639	3.144639	14.23325	9.328
Atiii	3.156025	3.156025	18.23861	10.084

Table 22 Percent difference between subgroups in Group 5

Subgroup	E (MPa)	σ_y (MPa)	σ_u (MPa)	$\%\varepsilon_u$ (μm/μm)
Ai->Aii	-13.3663	-13.3663	5.119812	2.7058
Ati-> Atii	-13.4036	-13.4036	6.747781	2.3846
Ai->Aiii	-11.9716	-11.9716	13.19665	9.8742
Ati-> Atiii	-12.0012	-12.0012	16.94901	9.3416
Aii->Aiii	1.609906	1.609906	7.683457	7.1684
Atii->Atiii	1.619554	1.619554	9.556382	6.957

The same behavior is supported in Group 5. The microstructures with the highest volume fraction of ceramic inclusions reveal the highest ultimate strength and ductility values. Table 21 illustrates the addition of aluminum oxide particles into a TRIP steel matrix increases the value of the modulus of elasticity, yield strength, but more importantly, strength and ductility of the material as a whole, disregarding the outlier presented by Subgroup Ai. For Atiii, the ultimate strength increased 18.24% from the original structure in Group 1 and also increased in ductility by 10.08% strain. Within the subgroups, it is also evident in Group 5 that the larger volume fraction of ceramic inclusions increases the values of ultimate tensile strength in all the microstructures, and also the strain at this value, indicating an enhancement in ductility. The modulus of elasticity and yield strength in this group still follows the pattern described in the previous groups.

5. CONCLUSION

The advantages of TRIP steel in industry today already provide the highest ductility to strength ratio in industry. According to this research, these parameters may be increased even more simultaneously by the addition of ceramic inclusions. All the simulations illustrated that as the volume fraction of ceramic particles in the microstructure increased, the strength and ductility of the composite increased as well. For all material groups, Groups 2-5, Subgroup Aiii/Atiii, which indicate the RVE's with 50% ferrite, 25% bainite, 15% austenite or martensite, and 10% ceramic inclusions, illustrated the largest simultaneous enhancement in strength and ductility among all the analyzed combinations. The transformed ceramic particle reinforced TRIP steel composite, Atiii, illustrated about an 18% increase in strength all the ceramic material groups from the original TRIP steel microstructure with no reinforcement, At. More accurately, the highest ultimate strength recorded from the ceramic groups from microstructure Atiii was from Group 2 which entailed silicon carbide particles. Group 2 reflected an ultimate tensile strength of 1500.33MPa compared to the unreinforced TRIP steel microstructure in Group 1 with an ultimate tensile strength of 1268.16MPa. Also, very close by, Group 5, with aluminum oxide particles illustrated a competitive ultimate tensile strength of 1499.45MPa. In regards to ductility all groups also showed a proportional increase in strain value at ultimate to the volume fraction of ceramic inclusions. Subgroup Aiii/Atiii illustrated the highest increase in ductility with about an 8-10% increase in strain at the ultimate tensile strength for all ceramic material groups.

Group 5, with aluminum oxide particles, revealed the highest enhancement in ductility of 62.69% for Aiii and 61.81% for Atiii. Group 1 reached ultimate strength for microstructure A at 53.37% and At at 51.73%. Group 5 illustrates a 9.33% and 10.08% increase in strain at ultimate from the control TRIP steel microstructures in Group 1. Group 2, with silicon carbide illustrates a very close, yet smaller value for strain at ultimate for Aiii, 61.62%, and Atiii, 61.54%. Yet, these two structures still illustrate a significant 8.25% and 9.81% strain increase from the original TRIP steel microstructure in Group 1. Ultimately, although all the material groups showed proof of simultaneous enhancement of strength and ductility by addition of ceramic inclusions, the highest strength and second highest ductility was achieved by the addition of 10% volume fraction of silicon carbide inclusions into the TRIP steel matrix. The second highest strength and highest ductility resulted from the addition of 10% volume fraction of aluminum oxide particles into the TRIP steel matrix. Due to the similarity in ultimate tensile strengths between the silicon carbide and aluminum oxide microstructures, it may be best to conclude that aluminum oxide illustrates the most optimum results for this study.

The possibility of a new, innovative material is proposed in this study. A third generation advanced high strength steel that encompasses the idea of particle reinforced composites has been suggested and studied. This new material demonstrates superior strength and ductility performance under strain controlled tensile loading compared to unreinforced TRIP steel. By investigating the deformation behavior of ceramic particle reinforced TRIP steel with varying ceramic material parameters, it is concluded that a

large volume fraction of ceramic particles are one key parameter responsible for the simultaneous enhancement of strength and ductility in reinforced TRIP steel. Also, another key parameter that was found through this study indicates that utilizing 99.9% aluminum oxide for the ceramic inclusions will provide the most optimal improvement in mechanical behavior for TRIP steel.

6. SUMMARY OF COMPLICATIONS AND RECOMMENDATIONS

6.1 Complications

During the course of this study, one of the largest problems was the compatibility of ABAQUS with the generated RVE's. The residual would diverge and become exceedingly large, which translates to the fact that the elements generated in the mesh for the microstructure would become far too distorted for analysis, thus leading to unreliable results and the whole job to abort. After much trial and error, mesh adaptivity was one proposed solution for this problem. This involves a built in feature in ABAQUS in which Figure 81 illustrates a close up of the microstructure in Group 1 where this feature is applied. For comparison, Figure 82 shows the same microstructure without mesh adapativity, which unfortuantely yielded the same results.

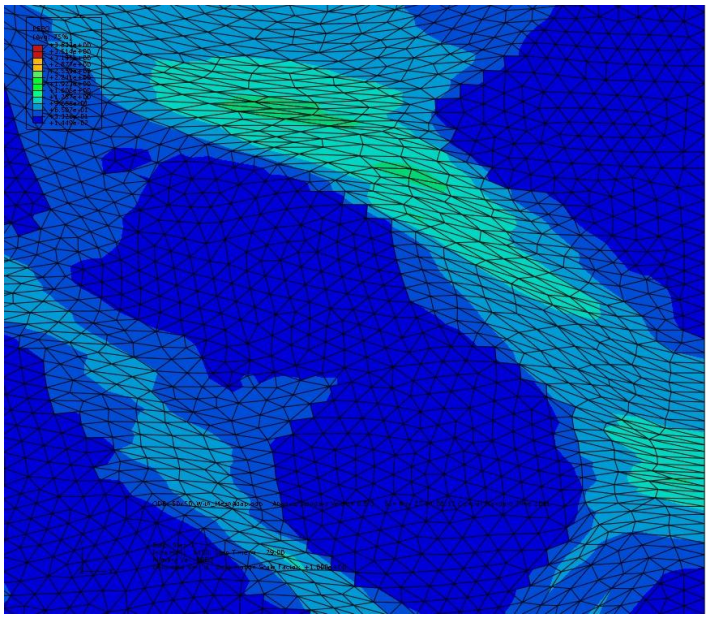

Figure 81 Close-up of bottom right side of Group 1 TRIP steel microstructure with mesh adaptivity

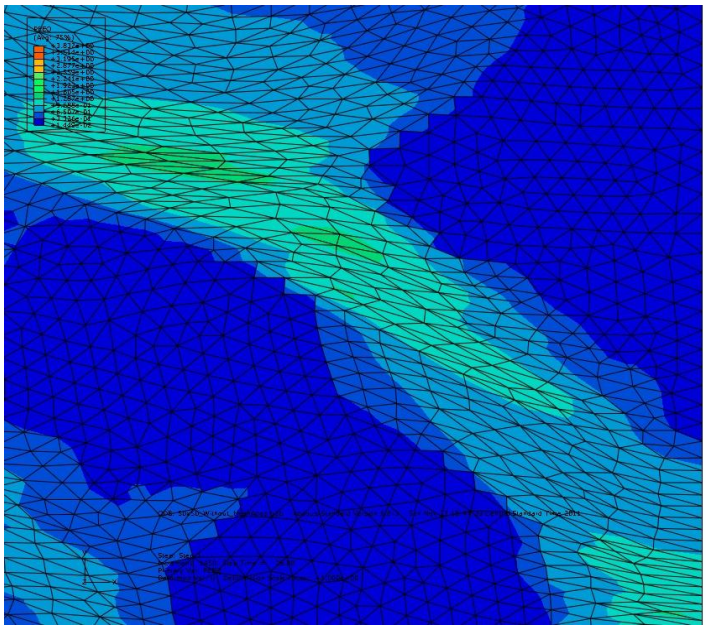

Figure 82 Close-up of bottom right side of Group 1 TRIP steel microstructure without mesh adaptivity

Unfortunately, due to large deformations of the microstructure in both cases, the elements still could not remain stable through the analysis. Figure 83 illustrates the resulting stress and strain diagram from this trial.

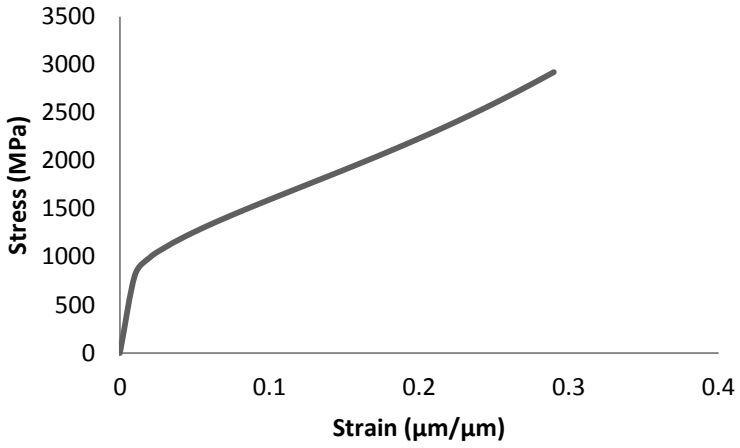

Figure 83 Stress vs. strain diagram for Group 1 microstructure with mesh adaptivity and without mesh adaptivity

This simulation was 100 increments at 0.02 steps and aborted at 30% strain, which is not adequate or sufficient for this research. Consequently, another approach was necessary. The next proposed solution for this problem is utilizing explicit elements, which allows for more strain deformation in the material. This allows for a larger breadth of the stress behavior under a larger strain. In explicit technique, ABAQUS removes elements that exceed a certain residual or become highly distorted. Due to this, we are also able to physically map where the largest problems arise in the microstructure and may physically see at what elements a crack begins and propagates.

Another challenge existed in ABAQUS meshing the generated RVE. The first microstructure created included polygon phases that were generated with specified resolutions. The corners of these polygons created a problem in the analysis due to the presented sharp edges. These sharp edges served as stress concentrations and would not portray accurate results. Due to this, the next attempt was creating the boundaries for the phases with p-lines. Unfortunately, this idea was quickly unacknowledged when ABAQUS illustrated complications with meshing the microstructure due to very fine sharp edges presented by the p-line intersections. Splines were the next proposed solution which seemed much more advantageous since this would allow the edges of the phases to be smooth curves. Also, this would embody a more realistic microstructure for the TRIP steel composite models. Problems arose when the microstructure was being created. In order to assign material properties to each phase after the microstructure was created, it was necessary to subtract out the phase geometries from the rectangular matrix, then assign the material properties to its proper phase, and then merge them all back together. With splines, ABAQUS executed a precise recalculation of all the phase geometries when subtracting them from the microstructure. Thus, when the phases were to be merged back together, the boundaries did not match. From this, it was decided that fit curved lines for each phase through their corresponding coordinates would solve this problem. After attempting this proposition, it was decided the nodes were far too close together in some instances and would resemble the same problems caused by p-lines. Thus, finally, it was decided the solution would be to revisit splines except not subtract the phases from the microstructure. Instead, after the phases are initially merged, the

properties could then be assigned by distinctly assigning properties to the faces of each phase through the coordinates of their respective geometries. With this, ABAQUS was then able to recognize each phase, and mesh the microstructure.

Another factor that is important to note is that quadratic shaped elements were utilized to mesh these microstructures. The models utilized required a far larger number of triangular elements than quadratic elements to execute analysis. A large number of elements results in longer time span necessary to complete an analysis. Due to the time constraints of this project, it was decided that quadratic elements should be utilized.

6.2 Recommendations

This study serves the purpose of beginning an innovative idea towards the possibility of a third generation high strength steel composite. These results were recorded and calculated from simulations with a variety of stated assumptions. It would be beneficial to perform this analysis under different loading and environmental conditions to view how the microstructures react. Also, varying volume fractions of each TRIP steel constituent along with particles may give more enhanced results. Overall, expanding on the varied parameters in this study is also recommended. One example is, but not limited to, investigating the effects of varying the sizes of the particles and constituents in the microstructures. This may even lead into an investigation of size effect on particle reinforced TRIP steels. One of the most important factors that should be considered in future studies when considering TRIP steels is applying the phase transformation mechanism and kinetics. With this, it is also important to investigate the

effects of gradient theory and phase boundaries as well as not assuming perfect bonding between particles and the TRIP steel matrix. This may give an even closer estimation to what would occur in experimental circumstances which should also be done to investigate the accuracy of produced simulations. This study serves as the stepping stone to unlimited possibilities. These recommendations illustrate a fraction of how this research may be expanded to ultimately create a new innovative particle reinforced TRIP steel composite.

REFERENCES

1999-2011. Key to Metals AG The World's Most Comprehensive METALS Database: High Strength Steels: TRIP Steels.

Abu Al-Rub, R.K., 2009. Modeling the Particle Size and Interfacial Hardening Effects in Metal Matrix Composites with Dispersed Particles at Decreasing Microstructural Length Scales. International Journal for Multiscale Computational Engineering 7.

Bao, G., 1992. Damage due to fracture of brittle reinforcements in a ductile matrix. Acta Metallurgica et Materialia 40, 2547-2555.

Bleck, W., Kranz, S., Ohlert, J., Papamantellos, K., 1999. 41st MWSP Conference Proceedings, ISS, pp. 295–305.

Callister, W.D., 2007. Materials Science and Engineering: An Introduction, 7th ed. John Wiley & Sons, Inc.

Choi, K.S., 2009. in: Laboratory, C.S.a.M.D.P.N.N. (Ed.).

Choi, K.S., Lui, W.N., Sun, X., Khaleel, M.A., 2009. Microstructure-based constitutive modeling of TRIP steel: Prediction of ductility and failure modes under different loading conditions. Acta Materialla 57, 2592-2604.

Choi, K.S., Soulami, A., Lui, W.N., Sun, X., Khaleel, M.A., 2010. Influence of various material design parameters on deformation behaviors of TRIP steels. Computational Materials Science 50, 720-730.

Christman, T., Needleman, A., Suresh, S., 1989. An experimental and numerical study of deformation in metal-ceramic composites. Acta Metallurgica 37, 3029-3050

Corbin, S.F., Wilkinson, D.S., 1994. Low strain plasticity in a particulate metal matrix composite. Acta Metallurgica et Materialia 42, 1319-1327.

Delannay, L., Jacques, P.J., Pardoen, T., 2008. Modelling of the plastic flow of trip-aided multiphase steel based on an incremental mean-field approach. International Journal of Solids and Structures 45, 1825-1843.

Evans, A.G., Zok, F.W., Davis, J., 1991. The role of interfaces in fiber-reinforced brittle matrix composites. Composites Science and Technology 42, 3-24.

Gurson, A.L., 1977. Continuum Theory of Ductile Rupture by Void Nucleation and Growth: Part 1- Yield Criteria and Flow Rules for Porous Ductile Media. J. Eng. Mater. Technol 99, 2-15.

Hom, C.L., McMeeking, R.M., 1991. Plastic flow in ductile materials containing a cubic array of rigid spheres. International Journal of Plasticity 7, 255-274.

Hu, M.S., 1991. Some effects of particle size on the flow behavior of AlSiCp composites. Scripta Metallurgica et Materialia 25, 695-700.

Iwamoto, T., Tomita, Y., 1995. Consitutive modelling of TRIP steel and its applictions to the improvement of mechanical properties. International Journal of Mechanical Sciences 37, 1295-1305.

Iwamoto, T., Tomita, Y., 2001. Computational prediction of deformation behavior of TRIP steels under cyclic loading. International Journal of Mechanical Sciences 43, 2017-2034.

Iwamoto, T., Tsuta, T., 2000. Computational simulations of the dependence of austenitic grain size on the deformation behavior of TRIP steels. International Journal of Plasticity 16, 791-804.

Iwamoto, T., Tsuta, T., 2002. Computational simulation on deformation behavior of Ct specimens of TRIP steel under mode I loading for evaluation of fracture toughness. International Journal of Plasticity 18, 1583-1606.

Iwamoto, T., Tsuta, T., 2004. Finite element simulation of martensitic tranformation in single-crystal TRIP steel based on crystal plasticity theory with cellular automata approch. Key Engineering Materials 274-276, 679-684.

Iwamoto, T., Tsuta, T., Tomita, Y., 1998. Investigation on deformation mode dependence of strain-induced martensitic transformation in TRIP steels nad modeling of transformation kinetics. International Journal of Mechanical Sciences 40, 173-182.

Jacques, P.J., Furnemont, Q., Pardoen, T., Delannay, F., 2001. On the role of martensite transformation on damage and cracking resistance in TRIP-assisted multiphase steels. Acta Materialla 49, 139-152.

Jain, M., MacEwen, S.R., Wu, L., 1994. Finite element modelling of residual stresses and strength differential effect in discontinuously reinforced metal matrix composites. Materials Science and Engineering: A 183, 111-120.

Kelly, P., 2008. Solid Mechanics Part II. Kelly, P., University of Auckland.

Kim, C., 1988. Modeling Tensile Deformation of Dual-Phase Steel. Metallurgical And Materials Transactions A 19, 1263-1268.

Kiser, M.T., Zok, F.W., Wilkinson, D.S., 1996. Plastic Flow and Fracture of a Particulate Metal Matrix Composite. Acta Materialla 44, 3465-3476.

Lani, F., Furnemont, Q., Van Rompaey, T., Delannay, F., Jacques, P.J., Pardoen, T., 2007. Mutliscale mechanics of TRIP-assisted multiphase steels: II. Micromechanical modelling. Acta Materialla 55, 3695-3705.

Lemaitre, J., 1992. A Course On Damage Mechanics. Springer Verlag., Berlin.

Llorca, J., Poza, P., 1994. Influence of matrix strength on reinforcement fracture and ductility in Al・Al2O3 composites. Materials Science and Engineering: A 185, 25-37.

Lloyd, D.J., 1990. Aspects of Fracture in Particulate Reinforced Metal Matrix Composites. Acta metall. mater 39, 59-71.

Lloyd, D.J., 1991. Aspects of Fracture in Particulate Reinforced Metal Matrix Composites. Acta metall. mater 39, 59-71.

Lloyd, D.J., 1994. Particle reinforcement aluminum and magenesium matrix composites. Institute Materials Review 39, 1-23.

Mazen, A.A., Emara, M.M., 2004. Effect of Particle Cracking on the Strength and Ductility of Al-SiCp Poweder Metallury Metal Matrix Composites. Journal of Materials Engineering and Performance 13, 39-46.

McDaniels, D.L., 1985. Analysis of Stress-Strain, Fracture, and Ductility Behavior of Aluminum Matrix Composites Containing Discontinuous SiC Reinforcement. Metallurgical Transactions A 16A, 1105.

Mummery, P.M., Derby, B., Scruby, C.B., 1993. Acoustic emission from particulate-reinforced metal matrix composites. Acta Metallurgica et Materialia 41, 1431-1445.

Muransky, O., Hornak, P., Lukas, P., Zrnik, J., Sittner, P., 2006. Investigation of retained austenite stability in Mn-Si TRIP steel in tensile deformation condition. Journal of Achievements in Materials and Manufacturing Engineering 14, 26-30.

Nan, C.W., Clarke, D.R., 1995. The influence of particle size and particle fracture on the elastic/plastic deformation of metal matrix composites. Acta metall. mater 44, 3801-3811.

Olson, G.B., Cohen, M., 1975. Kinetics of Strain-Induced Martensitic Nucleation. Metallurgical Transactions A 6A, 791-795.

Papaefthymiou, S., 2005. Failure mechanisms of multiphase steels. Aachen University, Aachen, Germany.

Papaefthymiou, S., Prahl, U., Bleck, W., Van der Zwaag, S., Siestsma, J., 2006. Experimental observations on th correlation between microstructure and fracture of multiphase steels. International Journal of Material Research 97, 1723-1731.

Papatriantafillou, I., Agoras, M., Aravas, N., Haidemenopuolos, G., 2006. Constitutive modeling and finite element methods for TRIP steels. Computational Methods in Applied Mechanics and Engineering 195, 5094-5114.

Sakaki, T., Ohnuma, K., Sugimoto, K., Ohtakara, Y., 1990. Plastic Anisotropy of Dual-Phase Steels. International Journal of Plasticity 6, 591-613.

Shen, Y.L., Finot, M., Needleman, A., Suresh, S., 1994. Effective elastic response of two-phase composites. Acta Metallurgica et Materialia 42, 77-97.

Sierra, R., Nemes, J.A., 2008. Investigation of the mechanical behavior of multi-phase TRIP steels using finite element methods. International Journal of Mechanical Sciences 50, 649-665.

Simo, J.C., Hughes, T.J.R., 1998. Computational Inelasticity. Springer, New York.

Stringfellow, R.G., Parks, D.M., Olson, G.B., 1991. A constitutive model for a transformation plasticity accompanying strain-induced martensitic transformations in metastable austenitic steels. Acta metall. mater 40, 1703-1716.

Taggart, D.G., Bassani, J.L., 1991. Elastic-plastic behavior of particle reinforced composites influence of residual stresses. Mechanics of Materials 12, 63-80.

Umemoto, M., Todaka, Y., Takahashi, T., Li, P., Tokumiya, R., Tsuchiya, K., 2003. Characterization of Bulk Cementite Prodiced By Mechanical Alloying and Spark Plasma Sintering. Journal of Metastable and Nanocrystalline Materials 15-16, 607-614.

Uthaisangsuk, V., Prahl, U., Bleck, W., 2008. Micromechanical modelling of damage behavior of multiphase steels. Computational Materials Science 43, 27-35.

Uthaisangsuk, V., Prahl, U., Bleck, W., 2011. Modelling of damage and failure in multiphase high strength DP and TRIP steels. Engineering Fracture Mechanics 78, 469-486.

Vasudevan, A.K., Richmond, O., Zok, F., Embury, J.D., 1989. The influence of hydrostatic pressure on the ductility of Al-SiC composites. Materials Science and Engineering: A 107, 63-69.

Voyiadjis, G.Z., Abu Al-Rub, R.K., Palazotto, A.N., 2006. On the Small and Finite Deformation Thermo-elasto-viscoplasticity Theory for Strain Localization Problems:

Algorithmic and Computational Aspects. European Journal of Computational Mechanics 15.

Wagoner, R.H., Smith, G.R., 2006. Advanced High-Strength Steels (AHSS) Workshop, Arlington, Virginia, USA.

Wenzel, C., Aneziris, C.G., 2010. Ceramic matrix composites based on Mg-PSZ with Cr-Ni-steel-additions with improved thermo-mechanical properties. Materials Science and Engineering B 176, 32-40.

Xu, X., Needleman, A., 1994. Numerical simulations of fast crack growth in brittle solids Journal of the Mechanics and Physics of Solids 42, 1397-1434.

Yang, J., Cady, C., Hu, M.S., Zok, F., Mehrabian, R., Evans, A.G., 1990. Effects of damage on the flow strength and ductility of a ductile Al alloy reinforced with SiC particulates. Acta Metallurgica et Materialia 38, 2613-2619.

Zahl, D.B., McMeeking, R.M., 1991. The influence of residual stress on the yielding of metal matrix composites. Acta Metallurgica et Materialia 39, 1117-1122.

Zhang, K., Zhang, M., Guo, Z., Chen, N., Rong, Y., 2011. A new effect of retained austenite on ductility enhancement in high-strength quenching -partitioning-tempering martensitic steel. Materials Science and Engineering: A.

Zhu, H.T., Zbib, H.M., Khraisheh, M.K., 1994. Flow Strength and Size Effects of an Al-Si-Mg Composite Model System Under Multiaxial Loadings. Scripts Metallurgics et Materialia 32, 1895-1902.

Zrnik, J., Mamuzic, I., Dobatkin, S.V., 2006. Recent Progress in High Strength Low Carbon Steels. Metalurgia 45, 323-331.

VITA

Name: Sara Cristina Diaz

Address: Room CE 16D
Zachary Department of Civil Engineering
3136 TAMU
Texas A&M University
College Station, TX 77843

Email Address: scd7892@gmail.com

Education: B.S., Civil Engineering, Texas A&M University, 2010
M.S., Civil Engineering, Texas A&M University, 2012